Design, Modeling, And Experimental Validation Of A Stirling Engine With A Controlled Displacer Piston

By

Anna Winkelmann

Thesis

Submitted to the Faculty of the

Graduate School of Vanderbilt University

in partial fulfillment of the requirements

for the degree of

MASTER OF SCIENCE

in

Mechanical Engineering

May, 2015

Nashville, Tennessee

Approved:

Dr. Eric J. Barth

Dr. Michael Goldfarb

Dr. Alvin Strauss

ACKNOWLEDGEMENTS

First and foremost I would like to express my gratitude and appreciation to my advisor, Dr. Eric J. Barth, for giving me the opportunity to work and do research in the Laboratory for the Design and Control of Energetic Systems. I would like to thank him for his guidance throughout this work. My gratitude also extends to the rest of my colleagues, Bryn Pitt, David Comber, and Alex Pedchenko, each of whom I learned from. I would also express my appreciation to the members of my thesis committee: Dr. Michael Goldfarb and Dr. Alvin Strauss.

I would like to thank Red River machine for machining all my parts, for being very responsive and very helpful. I appreciate all the work they have done for me.

I thank my parents and my brother for their constant support and encouragement during my studies despite being so far away from home. Without them I would have not made it so far. At this point I would like to especially thank my dad for all the technical advice, mental support, and for being there whenever I was in need to talk to someone.

Finally, I would like to thank the Center for Compact and Efficient Fluid Power (CCEFP) grant EEC-0540834 for funding this work.

TABLE OF CONTENTS

	Page
Acknowledgements	ii
List of Figures	iv
List of Tables	vii
Chapter	
I. Overview	1
Introduction and Motivation	1
Literature Survey	3
Organization of the Document	4
References	5
II. Manuscript 1: System Dynamic Model and Design of a Stirling Pump	7
Abstract	7
Introduction	7
Design of Stirling Pump	9
Multi-Stage to Single-Stage Design Change	10
Working Fluid and Pumping Fluid	11
Other Design Changes	13
Dynamic Model	14
Results	17
Conclusion	19
Acknowledgement	20
References	20
III. Manuscript 2: Design, model, and experimental testing of a stirling Pressurizer	21
Abstract	21
Introduction	21
Design	23
Dynamic Model	25
A. Pressure Dynamics	26
B. Mass Flow	27
C. Heat transfer	28
D. Regenerative Channel	30
Experimental Validation of the Model	31
A. Experimental Setup	31
B. Engine Parameters	35
C. Tuned Model Parameters	36
D. Sinusoidal Displacer Motion	37
E. Non-sinusoidal Displacer Motion	39
Conclusion	41
Acknowledgment	41
References	41
IV. Future Directions and Discussion	43
Appendix	45
A. Simulink Diagrams	45
B. Matlab Code	53
C. Technical drawings for prototype	58

LIST OF FIGURES

Page

Figure 1-1: Comparison of the energy transduction of a typical electric system with a Stirling pressurizer combined with a hydraulic pump 2
Figure 1-2: Energy density vs. actuation power density of different devices. 2

Figure 2-1: Generation-1 multistage thermocompressor device concept 9
Figure 2-2: Design for a single stage of the generation-1 thermocompressor device. A reciprocating lead screw driven by a DC motor moves a loose-fit displacer piston between the hot side and the cold side. In response to this, the pressure in the device changes as the working fluid moves between the hot side (high pressure) and the cold side (low pressure). As the pressure fluctuates, the thermocompressor outputs high pressure fluid to a reservoir and intakes low pressure fluid from the environment (or from a previous stage). 10
Figure 2-3: Design of the generation 2 device 11
Figure 2-4: Pumping Section 12
Figure 2-5: Linear DC Servomotor 13
Figure 2-6: Driving (blue) and average (green) pressure vs. time 18
Figure 2-7: Displacement of the pumping piston with respect to time 18
Figure 2-8: Pressure dynamics in the pumping chamber compared to the supply pressure (7 MPa) and atmospheric pressure (101kPa) 19

Figure 3-1: Design of the Stirling pressurizer 24
Figure 3-2: A System overview of all the dynamics taking place within the pressurizer. This diagram illustrates dynamic interactions within the system 27
Figure 3-3: Diagram explaining the shuttle heat transfer 30
Figure 3-4: Experimental setup 33
Figure 3- 5: Thermographic image of the engine section 34
Figure 3-6: Orifice area was adjusted such that modeled and measured pressure inside the return chamber would be the same. 36
Figure 3-7: Measured and modeled pressure Pk inside the engine section at low heater head temperature (250°C), low pressure (10 bar), and at a frequency of 1 Hz. The modeled pressure ratio is about 7% lower than measured pressure ratio. 37
Figure 3-8: Measured and modeled pressure Pk inside the engine section at 450°C heater head temperature, high pressure (20 bar), and at a frequency of 2 Hz. The modeled pressure ratio is about 3% higher than measured pressure ratio. 38

Figure 3-9: Measured and modeled pressure Pk inside the engine section at high heater head temperature (500°C), high pressure (20 bar), and at a frequency of 2 Hz. The modeled pressure ratio is about 4.6% higher than measured pressure ratio. 38
Figure 3-10: Filtered square wave motion profile of the displacer piston at 450°C, 20bar and 2Hz 40
Figure 3-11: Measured and modeled pressure Pk inside the engine section at 450°C heater head temperature, high pressure (20 bar), and at a frequency of 2 Hz. The modeled pressure ratio is 8% higher than measured pressure ratio. 40

Figure 4-1: Stirling device using additive manufacturing capabilities 44

Figure A-1: Overall system 45
Figure A-2: Volumes 45
Figure A-3: Engine dynamics 46
Figure A-4: Pressure dynamics on hot side 47
Figure A-5: Heat transfer losses 48
Figure A-6: Regenerative system 48
Figure A-7: Mass flow rate in engine section 49
Figure A-8: Mass flow rate in engine section times T_{flow} 49
Figure A-9: Pressure dynamics on cold side 50
Figure A-10: Direction switch 51
Figure A-11: Mass flow rate between cold side and return chamber 51
Figure A-12: Mass flow rate between cold side and return chamber 52

Figure C-1: Engine weld assembly 58
Figure C-2: Heater head 59
Figure C-3: Inconel cylinder 60
Figure C-4: Cooling fins 61
Figure C-5: Cooler head 62
Figure C-7: Top part of Hugger1 64
Figure C-8: Shaft part of hugger1 65
Figure C-9: Return part of hugger1 66
Figure C-10: Hugger2 of return chamber 67
Figure C-11: Top part of hugger2 68
Figure C-13: Displacer weld assembly 70
Figure C-14: Top part of displacer piston 71
Figure C-15: Displacer cylinder 72
Figure C-16: Bottom of displacer 73

Figure C-17: Extension rod 74
Figure C-18: Clamp assembly 75
Figure C-21: Connection between coupling and linear motor 78

LIST OF TABLES

Page

Table 2-1: Values of significant parameters 15
Table 2-2: Values of significant parameters 16
Table 2-3: Conditions for P_u and P_d 16
Table 2-4: Parameters used in simulation 17

Table 3-1: Engine Parameters 35
Table 3-2: Pressure ratio of experimental and 39
Table 3-3: Pressure ratio of experimental and modeled data at 2 Hz 39

CHAPTER I
OVERVIEW

Introduction and Motivation

An un-tethered, portable, and effective power supply for human-scale robots has progressively become more important in robotics research. This is because today's mobile robots must be energetically autonomous to be truly effective. Typical electric power supply and actuation systems using batteries and motor drives are not capable of powering human-scale robots like the Honda P3 robot or Honda ASIMO for more than 25 min. More recent progress includes systems like Big Dog which use hydrocarbon fueled IC engines and hydraulic actuators. Although superior in energy and power density to electric systems, IC engine based systems are very noisy.

The motivation of this research is to develop a more adequate power supply and actuation system that provides an order of magnitude greater power and energy density than the state-of-the-art batteries and motor drives while also avoiding the drawbacks of IC-based systems. It should also be noted that this challenge is very scale-dependent. Miniaturizing IC engines results in very poor efficiencies whereas the downscaling of Stirling devices actually enhances their power density [1]. The key to a more effective, portable power supply and actuation system is a combined measure of 1) a high energy density fuel source, 2) an efficient energy conversion to mechanical work, 3) a low converter mass, and 4) high power density actuators. The reason why an electric power supply and actuation system cannot power human-scale robots for more than 25 min is simply because of the low energy density of batteries and the low power density of electric motors compared to the high overall converter mass of the system. This work proposes a Stirling pressurizer combined with a power unit to be used as the power supply. The power unit could be anything that can be driven by a pressure swing such as a hydraulic pump, a linear electric generator, a reciprocating piston compressor, or a high pressure water filtration system, among others.

Figure 1-1 compares the energy transduction of a typical electric power supply and actuation system with the energy transduction of a Stirling pressurizer combined with a hydraulic pump. The power supply and actuation proposed here yields an increased energetic merit on the overall system level. This is because the pressurizer uses a much more energy dense fuel source than electric systems. The Stirling pressurizer can operate using a variety of heat sources such as high energy density hydrocarbon fuels (propane, butane, etc.), natural gas, solar concentrators, geothermal or radioisotope sources or others.
The energy density of hydrocarbon fuels for example is more than 65 times higher than the energy density of Li-ion batteries (46,000 kJ/kg vs 700 kJ/kg). This implies that a fairly poor energy conversion from the heat absorption to the pressurizer's power output (about 10% efficient) will result in a higher mechanical work output per unit mass of the overall system compared to electric systems. The Stirling pressurizer combined with a hydraulic pump will output about 3500 kJ per unit mass of energy source, while a typical battery and DC Motor drive outputs about 350-630kJ per unit mass of energy source. As a

result the proposed device has a 5-10 times higher energy figure of merit. Figure 1-2 illustrates graphically the energy density vs actuation power density of multiple devices. While batteries and motor drives are located in the lower left hand corner of the graph with low energy and power densities, the Stirling pressurizer combined with a power unit is located in the upper right hand corner with superior energy and power densities.

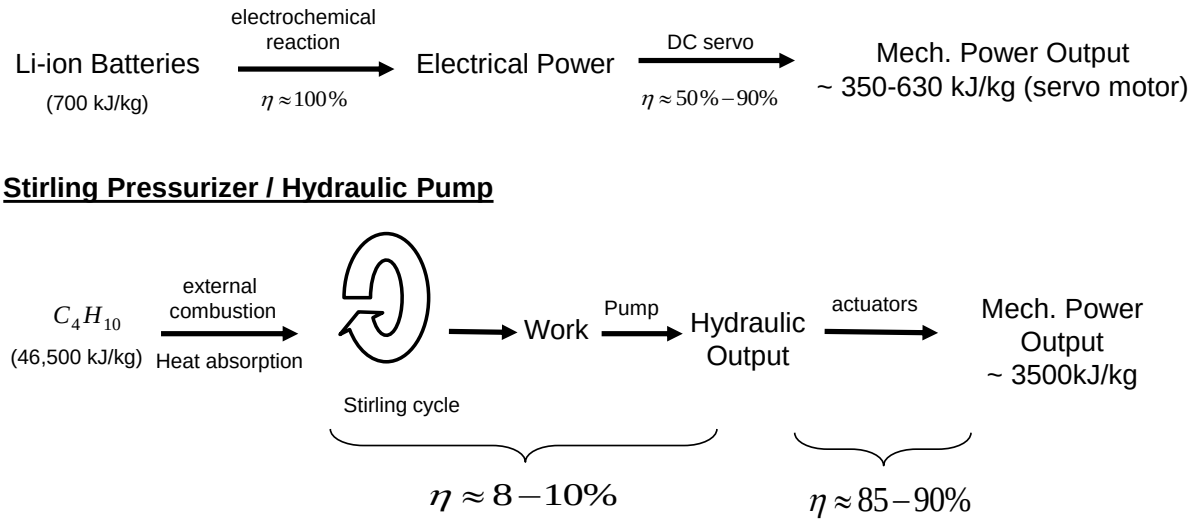

Figure 1-1: Comparison of the energy transduction of a typical electric system with a Stirling pressurizer combined with a hydraulic pump

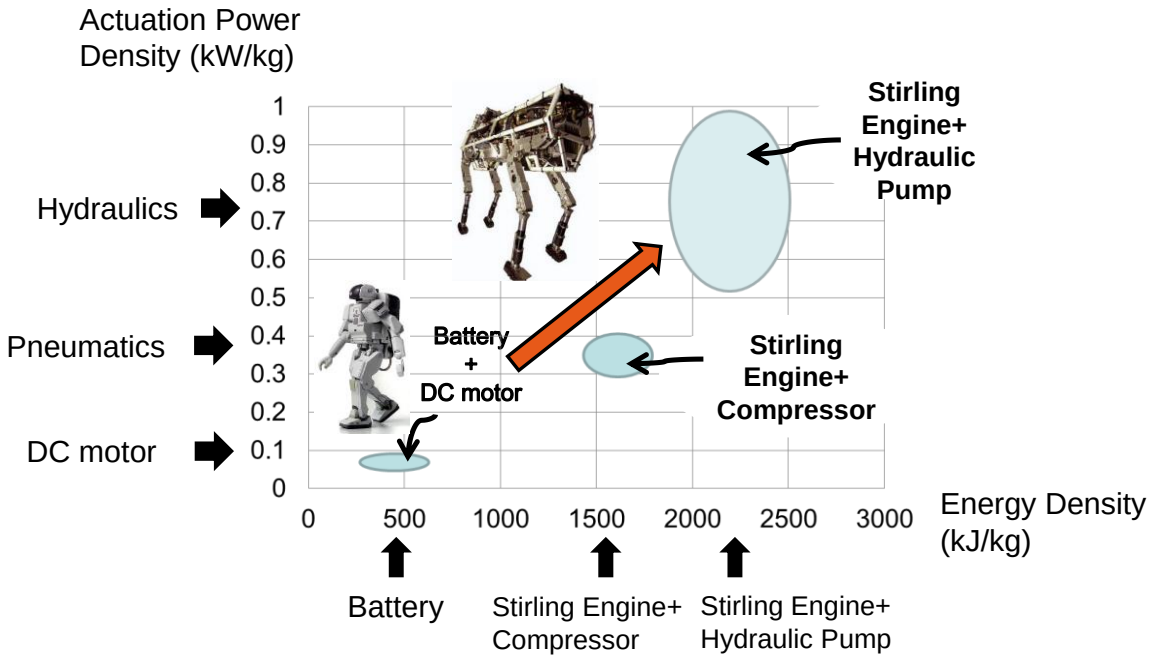

Figure 1-2: Energy density vs. actuation power density of different devices.

Literature Survey

The following literature review focuses on the evolution of the Stirling engine from a kinematic arrangement to a more power dense, purely dynamic arrangement; the free-piston Stirling engine. This is followed by a more recent research focus, namely the concept of a controlled displacer piston.

A Stirling engine is a heat engine that can operate using a variety of heat sources such as high energy density hydrocarbon fuels (propane, butane, natural gas, etc.), solar concentrators, geothermal, radioisotope sources, or others. Stirling engines cyclically heat and cool the working fluid which in turn induces a pressure change. This pressure change can then be used to drive a power unit. The Stirling engine was invented in 1816 by Robert Stirling and has long held the promise of being a clean, reliable, safe and quiet source of power. The first Stirling engine built was a purely kinematic arrangement where the motion of the displacer piston and the motion of the power piston were kinematically constrained such that displacer and power piston were always 90° out of phase. These engines were heavy and produced only a small amount of usable power. Stirling engines were outperformed by electric motors and internal combustion engines. In the twentieth century, advances in Stirling engines served to replace their kinematic arrangements with lightweight, small, purely dynamic elements. Such engines were called “free-piston Stirling engines.” The primary advantage of free-piston engines over its kinematic cousin include compactness, the ability to completely seal the engine, the elimination of side forces on the piston, and the ability to pressurize the engine to obtain higher power densities [4,5]. Nevertheless, this purely dynamic arrangement presented new challenges. The dynamic arrangements had to keep the engine self-oscillating, achieve the correct phase between the displacer and power piston dynamically, and robustly maintain self-oscillation in the face of load variations and disturbances. This is very difficult to achieve since free-piston Stirling engines utilize their own pressure change to drive the displacer piston. Self-oscillation is very sensitive to parametric properties of the engine and the load itself. Despite this, some free-piston Stirling devices have been built and shown to work. Beale built the first free-piston Stirling arrangements in the 1960’s [6,7]. Other noteworthy examples include the Harwell Thermomechanical Generator [7,8,9] and the liquid piston Fluidyne Stirling engine built by West [10,11]. Generally, the sensitivity to engine parameters is not well understood and results in a trial-and-error selection of engine specifications to arrive at acceptable parameters.

More recent research [12,13] overcomes the difficulty of getting the correct phase dynamically by controlling the displacer piston directly. By independently driving the displacer, the motion of the displacer is decoupled from the pressure dynamics within the engine. Ordinarily, the pressure and load influence the power piston which in turn drives the displacer piston through passive dynamics. By decoupling the displacer motion and then controlling it independently, the load does not affect the engine’s ability to self-oscillate. This allows an independent design of the displacer piston motion that can be controlled to shape the thermodynamic cycle in the face of arbitrary loads. Avoiding the complex coupling between the displacer and power pistons in favor of a fully controlled device transforms a free-piston Stirling engine into a mechatronic Stirling engine.

The work presented in this document builds on the work of [12,13] by using the position of the displacer piston as a control input to a first-principles model of a Stirling engine. An accurate, first-principles model that is amenable to deriving control laws for the displacer motion is critical for the line of work regarding controlled Stirling engines to continue. Furthermore, such a model needs to be rigorously validated experimentally. Although other papers [14, 15, 16] present control models of Stirling devices, many are not experimentally validated and none present a validated model that will accept an arbitrary displacer motion. The contribution of this paper is a first-principles model, amenable to the direct control of the displacer piston, that is validated experimentally for a wide range operating conditions.

Described herein is a Stirling device that uses the position of a displacer piston as a control input to a first-principles model. The design, first-principles model, and experimental setup of such a Stirling device are described. The first-principles model is experimentally validated for two different motion profiles of the displacer piston, a variety of heater head temperatures, and a variety of different average engine pressures. Additionally, a system dynamic model of a Stirling pressurizer combined with a hydraulic pump is presented.

Organization of the Document

The thesis is organized in four chapters. Chapter I presents the introduction, motivation, and the literature survey of the work. Chapter II and III are comprised of the manuscripts that encompass the body of the work completed during the author's two years at Vanderbilt University. Chapter II contains a Conference paper on the system dynamic model and design of a Stirling pressurizer combined with a hydraulic pump. Chapter III builds on the work of Chapter II by experimentally validating the model of a Stirling pressurizer. Chapter IV concludes with a discussion and future directions of the work.

Manuscript 1: System Dynamic Model and Design of a Stirling Pump

This paper presents the system dynamic model and design of a Stirling engine combined with a hydraulic pump. The Stirling pump is intended to fill the technological gap of a compact high energy density power supply for untethered fluid power applications in the 50W to 500W range. The Stirling device uses pre-pressurized helium as its working fluid for maximum power and efficiency. A directly controlled, loose-fit displacer piston moves the pre-pressurized working fluid between the hot and cold side of the sealed engine section; therefore inducing a pressure swing. The hydraulic pump uses this pressure swing to pump hydraulic fluid to a desired output pressure of 70bar. Manuscript 1 is based on the following conference paper:

A. Winkelmann, and E. J. Barth, "System Dynamic Model and Design of a Stirling Pump," *2014 Proceeding of the 27th Symposium on Fluid Power and Motion Control, ASME/Bath, FPMC2014-7839, September 10-12, 2014, Bath, England*

Manuscript 2: Design, Modeling and Experimental Validation of a Stirling Pressurizer with a Controlled Displacer Piston

This paper presents the design, first-principles model, and experimental setup of a Stirling Pressurizer. The first-principles model is validated with experimental results. This paper builds on the work of manuscript 1. More complexity has been added to the first-principle model by incorporating regenerative effects and heat transfer losses (shuttle losses and conduction losses) within the engine section. Experimental data for two directly controlled motion profiles of the displacer piston, a variety of heater head temperatures, and a variety of different average engine pressures validate the first-principle model. Experimental results show that the first-principles model can not only be used for the optimization of the pressurizer's efficiency and/or power output through an optimized displacer piston motion profile but the model also informs about the design and sizing of Stirling devices in general. Manuscript 2 is based on the following paper:

A. Winkelmann, and E. J. Barth,"Design, Modeling and Experimental Validation of a Stirling Pressurizer with a Controlled Displacer Piston," Submitted to*: IEEE/ASME Transactions on Mechatronics,* 2015.

References

[1] F. Formosa, L.G. Frechette, "Scaling laws for free piston Stirling engine design: Benefits and chellenges of miniaturization" Energy, vol 57, pp. 796-808, 2013. doi:10.1016/j.energy.2013.05.009

[2] C.Ronneau, "Energie, pollution de l'air et developpement durable", Presses universitaires de Louvain, 2004. Print

[3] M. Raibert et al., "BigDog, the Rough-Terrain Quadruped Robot", Proceedings of the 17th IFAC World Congress, 2008:17-1:10822-10825.

[4] G. Walker, "Large Free-Piston Stirling Engines," Lecture Notes in Engineering, Springer-Verlag, pp.216-221, 1985.

[5] A. J. Organ, "The Regenerator and the Stirling Engine," Mechanical Engineering Publications Limited, London, 1997.

[6] G. Walker, Stirling Engines, Oxford University Press, 1980.

[7] G. Walker and J. R. Senft, Lecture Notes in Engineering: Free Piston Stirling Engines, Springer-Verlag, New York, 1985.

[8] E. H. Cooke-Yarborough, E. Franklin, T. Gesow, R. Howlett, C. D. West, "Thermomechanical generator: an efficient means of converting heat to electricity at low power levels," Proceedings IEE, no. 121, p. 749-751, 1974.

[9] C. D. West, Principles and Applications of Stirling Engines, Van Nostrand Reinhold Company, New York, 1986.

[10] C. D. West, Liquid Piston Stirling Engines, Van Nostrand Reinhold Company, New York, 1983.

[11] F. T. Reader and M. A. Clarke, “Liquid Piston Stirling Air Engines,” 2nd International Conference of on Stirling Engines, 14 p, 1984

[12] Gopal, V. K., Duke, R., and Clucas, D., 2009. “Active Stirling Engine”. In TENCON 2009-2009 IEEE Region 10 Conference, IEEE, pp. 1–6.

[13] M. Craun, B. Bamieh, “Optimal Periodic Control of an Ideal Stirling Engine Model,” ASME Journal of Dynamic Systems, Measurement and Control, Jan 2nd 2015. doi:10.1115/1.4029682

[14] Chin-Hsiang Cheng, and Ying-Ju Yu, “Numerical model for predicting thermodynamic cycle and thermal efficiency of a beta-type Stirling engine with rhombic-drive mechanism”, Renewable Energy, vol. 35, pp. 2590-2601, 2010. doi:10.1016/j.renene.2010.04.002

[15] F. Formosa and G. Despesse, “Analytical model for Stirling cycle machine design”, Energy Conversion and Management, vol. 51, pp. 1855-1863, 2010. doi:10.1016/j.enconman.2010.02.010

[16] H. Karabulut, “Dynamic analysis of a free piston Stirling engine working with closed and open thermodynamic cycles”, Renewable Energy, vol. 36, pp. 1704-1709, 2011. doi:10.1016/j.renene.2010.12.006

CHAPTER II.
MANUSCRIPT 1: SYSTEM DYNAMIC MODEL AND DESIGN OF A STIRLING PUMP

Anna Winkelmann and Eric J. Barth

Vanderbilt University
Nashville, TN

Accepted as a Conference Paper at the
Proceedings of the 27th Symposium on Fluid Power & Motion Control
ASME/Bath 2014

Abstract

This paper presents the design and dynamic modeling of a second generation prototype combined Stirling engine pump. The Stirling pump is intended to fill the technological gap of a compact high energy density power supply for untethered fluid power applications in the 50W to 500W range. Specifically, this prototype is intended as a compact and quiet, untethered, hydraulic power supply for an ankle foot orthosis testbed associated with the Center for Compact and Efficient Fluid Power. The energy source for the unit is flexible and can include propane, butane, methane, natural gas, or other high energy density hydrocarbon source of heat. The target output pressure of 7 MPa (1000 psig) is obtained from a pumping stage that is driven by a sealed engine stage that utilizes high pressure helium as the working fluid. The separate pumping stage utilizes the differential pressure swing inside the engine section to pump hydraulic fluid to the desired output pressure. This paper presents the system dynamic model of the Stirling pump, and includes (1) heat transfer from the heat source to the working fluid in the hot space of the engine, (2) heat transfer from the working fluid in the cold space of the engine to the heat sink, (3) energetically derived pressure dynamics in the hot and cold spaces, (4) mass flow around the displacer piston in between the hot and cold sides, (5) work output to the pump driving section, (6) pumping piston inertial dynamics, (7) flow losses through the pump's check valves, and (8) hydraulic power output. This dynamic model allows components of the Stirling pump to be sized. The paper includes results from the dynamic model.

Introduction

More than 6 million individuals in the US are affected by an impaired ankle function. Commercially available passive Ankle Foot Orthoses (AFO) are compact and durable but lack functionality since they

cannot provide active motion control or generate net power. Active AFOs lack utility because they require tethered power supplies. One of the goals of the Center for Compact and Efficient Fluid Power (CCEFP) is to develop a fluid powered untethered device that operates in the 10 to 100 W power range to address the shortcomings of both passive and active AFOs. The Stirling pump is intended to serve as a silent, low vibration, compact, efficient, untethered, and high energy-density hydraulic power supply for an AFO, or similar application.

Stirling engines have been a research curiosity for more than a century. They have the appeal of offering power from any heat source including fuels, solar concentration, biomass, geothermal, or radioisotope decay. They also have the theoretical appeal of offering high thermodynamic efficiency due to the Stirling cycle. In the limited number of applications they have found, Stirling engines have been shown to be reliable and requiring little to zero maintenance. Despite their appealing properties, it is also fair to say that Stirling engines have fallen far short of their expectations primarily due to their low power density.

The historical progression of Stirling machines has offered some improvement in power density as their configurations have progressed from purely kinematic to free-piston varieties. Purely kinematic configurations rely on bulky linkages to enforce the correct phasing between the power piston and the displacer piston. Free-piston Stirling engines rely upon dynamic forces developed in the engine and the dynamic responses of the displacer and power pistons to enforce the necessary relationship between the two. If the engine is designed with these dynamics in mind, it can be shown that kinematic linkages are not necessary [1]. The first purely dynamic (non-kinematic) Stirling engine was Beale's free-piston Stirling engine [1]. The free-piston arrangement was not only lighter, but was able to be hermetically sealed and eliminated side forces on the pistons due to a connecting rod. Moreover, the ability to pressurize a sealed engine allows for higher power densities [2,3].

The challenge with free-piston configurations is to get the phase of the displacer and power piston correct in order to approximate the Stirling cycle. Designing the dynamics to do this correctly and robustly in the face of varying loads and heat input remains a technological barrier. Some success in the design of working free-piston Stirling engines is represented by many of Beale's arrangements [4, 5], the Harwell Thermomechanical Generator [6, 5, 7], and the liquid piston Fluidyne Stirling engine by West [8, 9]. The analysis of even these *working* Stirling machines demonstrates a knowledge gap with respect to designing their parameters for robust operation [5].

The Stirling pump presented in this paper overcomes this knowledge gap by decoupling the sensitive interacting dynamics of the displacer and power pistons. This is done by directly controlling the motion of the displacer piston. This allows more design degrees of freedom and ensures that the device is insensitive to load or internal dynamics variations. This paper describes the design and dynamic model of the combined Stirling engine pump. The Stirling pump is pre-pressurized and has a separate pump section that uses the pressure swing of the engine to pump hydraulic fluid.

Design of Stirling Pump

The rationale for the design of the proposed device result in large part from results and observations from a previous Stirling Thermocompressor device that was designed, fabricated, and experimentally tested by our research group [10]. The previous (generation 1) device was a multi-stage, true thermocompressor (Fig.2-1). A true thermocompressor uses the working fluid as the output fluid (air in this case). As discussed below, results from this previous device motivated: 1) a change in architecture from a multistage device to a single stage device, and 2) a change in functionality and architecture from a thermocompressor to a hydraulic pump. A single stage of this previous multistage device is shown in Fig. 2-2.

The generation 1 device used a brushless DC motor to drive a continuous linear reciprocating lead screw onto which the displacer piston was attached. The displacer piston was chosen to be made from Macor machinable ceramic due to its low thermal conductivity (1.46 W/m/K at 25°C) and its high service temperature. A quartz glass cylinder was chosen to seal the working fluid in between the heater head and the heat sink due to the same characteristics - low thermal conductivity and high service temperature.

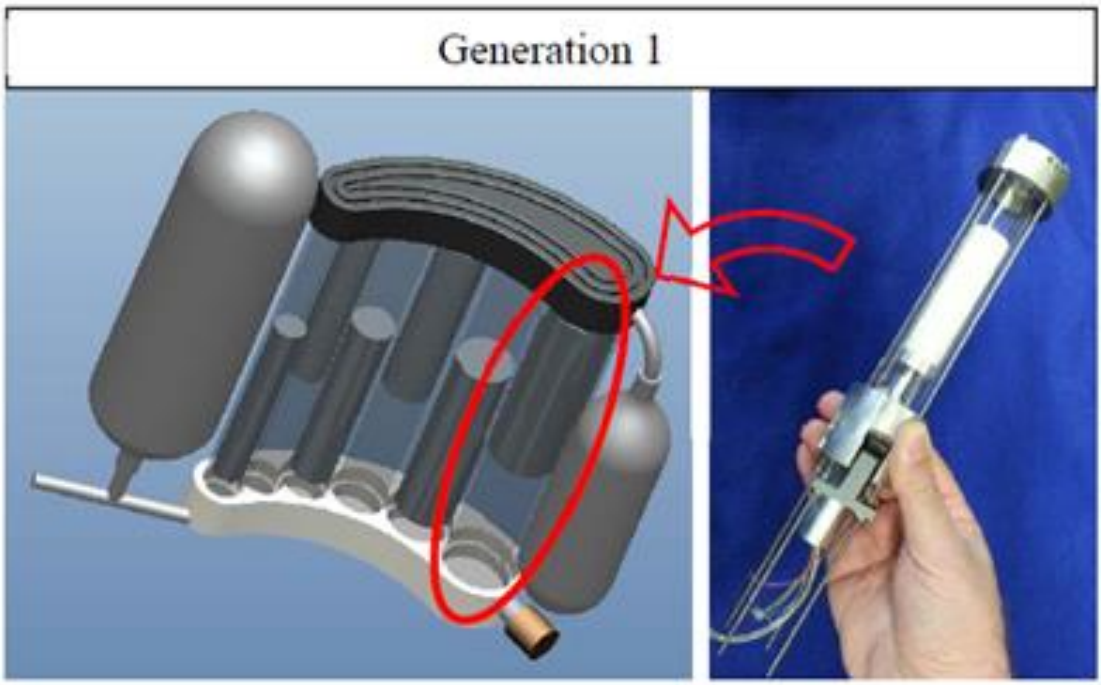

Figure 2-1: Generation-1 multistage thermocompressor device concept

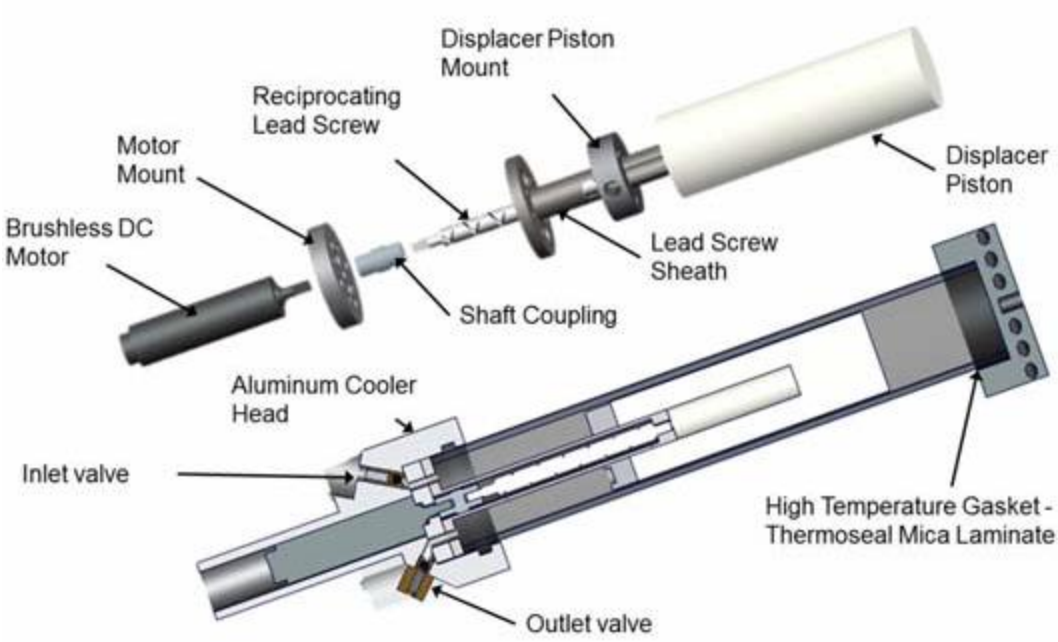

Figure 2-2: Design for a single stage of the generation-1 thermocompressor device. A reciprocating lead screw driven by a DC motor moves a loose-fit displacer piston between the hot side and the cold side. In response to this, the pressure in the device changes as the working fluid moves between the hot side (high pressure) and the cold side (low pressure). As the pressure fluctuates, the thermocompressor outputs high pressure fluid to a reservoir and intakes low pressure fluid from the environment (or from a previous stage).

Multi-Stage to Single-Stage Design Change

A dynamic simulation of the multi-stage thermocompressor [10] showed that more than four compression stages would be needed to reach the target output pressure. With respect to the multi-stage architecture, the prospect of having at least four compression stages to reach a target output pressure of 80 psig (for pneumatics reservoir) becomes untenable in the face of the mechanical complexity encountered in our single stage prototype. A multi-stage device requires that each stage become smaller with increasing pressure and the realities of dead-volume in such stages would make them far less than ideal as they become smaller. It was clear that a different approach was needed for the next generation of the device.

The generation 2 device will be of single-stage architecture with a sealed pre-pressurized engine section and separate pumping stage that pumps hydraulic fluid. Although the prospect of a true thermocompressor is appealing, the fundamental work density per stroke [J/(m^3stroke)] increases by more than two orders of magnitude by increasing the pre-pressurization (pressure when cold) to 500 psig. This agrees with the observation that almost every Stirling device (actual experimental platform) in the literature operates at a high pressure and agrees with the observations of authors such as G. Walker, G. T. Reader, O.R. Fauvel, I. Urieli, N. Isshiki, D. Gedeon, M. B. Ibrahim, M. Carlini, L. Bauwens, and others.

Pursuing this pre-pressurized architecture, as opposed to a true thermocompressor, requires a separate pump section that utilizes the differential pressure swing inside the engine section. Based on the experimentally measured heat transfer and pressure ratio of the generation-1 device, an output pressure of greater than 1000 psig (7000 kPa) can be obtained by utilizing a separate pumping stage and a single pre-pressurized sealed engine section with a similar size as the generation-1 device.

Working Fluid and Pumping Fluid

As discussed above, better compactness and power density can be achieved by using a single-stage, pre-pressurized engine section. This design change allows a consideration of a different working fluid than air. For maximum efficiency and power, helium was selected as the working fluid in the sealed engine section. The advantage of helium over air is that helium has a higher heat transfer coefficient than air. For our conditions, the use of helium over air would result in a 20 times higher heat transfer coefficient (14800 W/m^2/K for helium vs. 715 W/m^2/K for air).

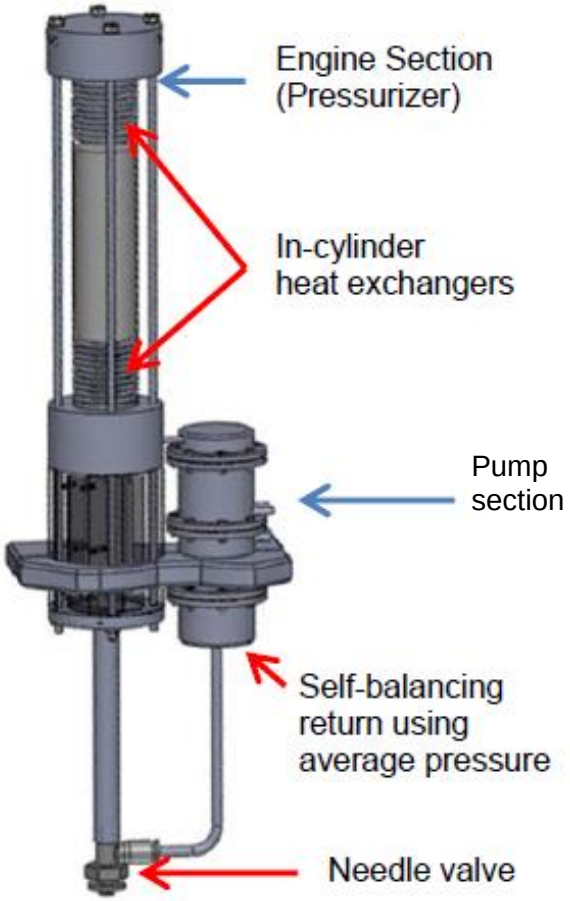

Figure 2-3: Design of the generation 2 device

The design change to a sealed single-stage also allows for a consideration of the fluid being pumped to be something other than air. Hydraulic pumping is inherently more efficient than compressing and

pumping air. This is due to the fact that when air is compressed, appreciable energy is stored as pressure potential energy that can be lost in the form of heat once pumped to its destination. Driving an air compressor also presents the possibility of pressurizing the gas to an inadequate level to pump, and then losing the work that was needed for that pressurization. This occurs even in the case where some of the air is pumped and may leave a remainder that is not pumped due to dead volume in the compressor section. This remainder is then susceptible to heat loss. Due to hydraulic oil's much higher stiffness as compared to a gas, much less energy is stored in the compression of the fluid thereby reducing thermal effects during the pumping phase. Finally, since hydraulic fluid is nearly incompressible, it eliminates the dead volume in the pumping section.

The design of the separate pump stage can be seen in Fig. 2-4. The pump section utilizes the differential pressure swing inside the engine section to pump hydraulic fluid at a desired output pressure. The pump section is composed of three types of chambers; the driving chamber, the pumping chamber, and the return chamber. The driving chamber will be connected to the cold side of the engine section such both are always at the same pressure. The bottom chamber represents a self-balancing return chamber. This is achieved by staying near an average pressure via a flow restriction implemented with a simple needle valve (see Fig. 2-3). The pressure difference in the driving and return chamber will cause the piston in the pumping chamber to move. When the pressure in the driver chamber is higher than in the return chamber, the piston moves down and pumps the hydraulic fluid in the lower pumping chamber through a check valve when the pressure is greater than the supply pressure. Simultaneously, the fluid in the upper pumping chamber decompresses and ultimately draws in more fluid through a check valve from the low pressure side of the hydraulic system. Conversely, when the piston moves up, fluid is pumped out of the upper pumping chamber and drawn in to the lower pumping chamber.

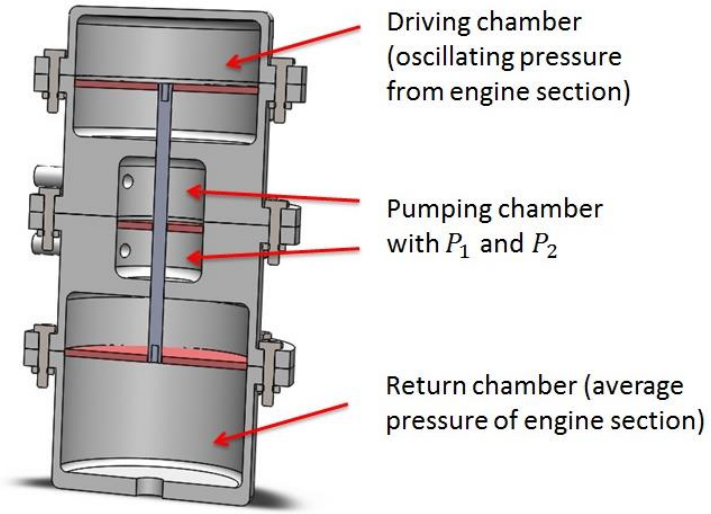

Figure 2-4: Pumping Section

Other Design Changes

Other design changes that need to be made to the generation-1 device include a different driver mechanism for the displacer piston and a different sealing mechanism at the hot end. For the generation 1 device, the position and velocity of the displacer was controlled by driving a reciprocating lead screw with a brushless DC motor. The reciprocating lead screw had “criss-crossed’ left-handed and right-handed threads which enabled the motor to be driven in one direction while achieving a reciprocating motion of the displacer piston. This was intended to reduce the power consumption of the motor since it does not need to accelerate and decelerate the motor shaft. Nevertheless, the power consumption was still found to be much higher than expected due to excessive friction in the lead screw mechanism. As a result, the displacer of the generation 1 device could only be driven at a frequency of 2.8 Hz. Dead volume around the lead screw mechanism was also a downside of the mechanism and limited the pressure swing in the engine. At 800°C and 2.8 Hz, the generation-1 device showed a pressure ratio of 1.6. While favorably comparable to devices in the literature, it was lower than expected.

The dead-volume and the higher than expected motor power necessitated a better solution for the linear drive mechanism of the displacer piston. The generation 2 device replaces the DC motor and the reciprocating lead-screw with a compact COTS linear actuator (Faulhaber) (see Fig. 2-5). The linear DC-Servomotor is light weight and has linear Hall sensors for position sensing. The positioning of the rod can be controlled very accurately such that dead volume at the cylinder ends can be held to a minimum. The smooth shaft of the linear motor also reduces the dead volume seen in the reciprocating lead screw design. A linear spring located in between the displacer piston and the linear motor will act as a conservative restoring force to minimize actuation energy, and effectively replaces the energetically motivated unidirectional operation of the reciprocating lead screw.

Figure 2-5: Linear DC Servomotor

Finally, experimental results of the generation-1 device revealed a slow leak resulting from the high temperature seal between the fused quartz glass and the heater head. To avoid a leak, the generation 2

device will have an engine cylinder made of Inconel 625 as opposed to fused quartz. This will be tougher and able to be welded, thus solving the sealing problem at the hot end.

Dynamic Model

The entire Stirling Pump can be dynamically modeled as having two sections, namely, the engine section and the pump section. The only input to the pump section is the pressure swing on the cold side of the engine section. The displacer piston in the engine section is driven by a linear DC servomotor with a sinusoidal velocity of

$$V = l_{Stroke} \pi f_{Hz} \sin(2\pi f_{Hz} t) \tag{1}$$

where f_{Hz} is the frequency the displacer motion, and l_{Stroke} is the stroke length of the displacer piston in the engine section of the Stirling pump. The position of the displacer is given accordingly by:

$$x_{displacer} = \frac{l_{stroke}}{2} + \frac{l_{stroke}}{2} \cos(2\pi f t) \tag{2}$$

The engine section of the Stirling pump is modeled as two control volumes of variable size. The control volumes represent the volume of the medium in the hot and the cold side of the engine section. The two control volumes are separated by the displacer piston which represents a flow restriction. The size of the control volume and the rate at which these are changing are governed by the position and velocity of the displacer piston above. The walls in the hot control volume (V_h) transfer thermal energy from heat source to the medium, and the walls in the cold control volume (V_k) transfer thermal energy from the medium out of the engine section of the Stirling pump. The wall temperatures on the hot and cold side of the engine section are set to a constant temperature of T_h and T_k, respectively. The dead volume around the displacer piston is equally divided into the model of V_h and V_k. Since the displacer never hits the ends of the cylinder, additional dead volume is added to both sides.

The pressure dynamics in the cylinder were derived from a fundamental power balance of the stored energy, enthalpy, heat flow and work:

$$\dot{U} = \dot{H} + \dot{Q}_{heat} - \dot{W} \tag{3}$$

Rearranging the terms and solving for the pressure dynamics inside the control volume yields:

$$\dot{P} = \frac{\sum \dot{m} \gamma_{He} R T_{flow} - \gamma_{He} P \dot{V} + h_{He} A_{h,k} (\gamma_{He} - 1)\left(T_{wall,h,k} - T\right)}{V} \tag{4}$$

An estimate of the heat transfer coefficient h_{He} was done by using fully developed pipe flow analysis as similar to [11]. In order to determine whether the flow is laminar or turbulent, the Reynolds number was calculated:

$$\mathrm{Re} = \frac{\dot{x}_m \delta}{\nu} \tag{5}$$

where $\dot{x}_m$ is the mean velocity of helium, δ is the characteristic length, and v is the kinematic viscosity of helium. The hydraulic diameter was used for the characteristic length given by:

$$\delta = \frac{4A_c}{C} \tag{6}$$

where A_c is the area of the gap in between the engine cylinder and the displacer piston and C is the wetted perimeter given by:

$$C = \pi(d_{cylinder} - d_{displacer}) \tag{7}$$

where $d_{cylinder}$ is the inside diameter of the Inconel housing and $d_{displacer}$ is the diameter of the displacer piston.

The heat transfer coefficient is determined by calculating the Nusselt number and solving for the heat transfer coefficient h by using the following equation:

$$Nu = \frac{h\delta}{k} = a \cdot \mathrm{Re}^m \cdot \mathrm{Pr}^n \tag{8}$$

where k is the thermal conductivity, Pr is the Prandtl number and a, m, n are constants that depend on the flow regime. For a frequency of 20 Hz, turbulent flow (Re>2300), and a smooth pipe, the constants used in the implementation of equations 5-8 are shown in the Table 2-1 below. Solving for the heat transfer coefficient yields 14800 W/m^2/K. Since the calculation of this parameter depends on the mean pressure and the mean temperature in determining the kinematic viscosity, conservative values were used such that the h calculated is a lower bound for the conditions in the engine.

Table 2-1: Values of significant parameters

$\dot{x}_m$	125 m/s
δ	0.00099 m
v	5.643e-6 m^2/s
k	0.245 W/m/K
a	0.023
Pr	0.656
m	0.8
n	0.3
h	14800 W/m^2/K

The mass flow restriction between the displacer piston and the Inconel cylinder that separates the two control volumes was modeled using Grinnel's model of compressible fluid flow [12] in a thin passage, which is given by:

$$\dot{m} = \left(\frac{r_{piston} s^3}{12 \mu_{helium} R T_{flow} L_{piston}} \right) \left(P_u^{\,2} - P_d^{\,2} \right) \tag{9}$$

where P_u and P_d are the upstream and downstream pressures found in the control volumes. The constants used in the implementation of Equations 4 and 9 are shown in Table 2-2.

Table 2-2: Values of significant parameters

s = 0.5 mm	R = 2.07x10^9 uJ/kg/K
L_{piston} = 76.2 mm	r_{piston} = 24.5 mm
γ_{helium} =1.664	$T_{wall,\ h}$ = 550ºC
$T_{wall,\ k}$ =50ºC	μ_{helium} =2.8x10^{-8} Ns/m
h_{helium} =14800 W/m^2/K	

The piston position and velocity in the pumping chamber depend on the cross-sectional area of the driving/return chamber (A_d), the pressure swing inside the engine, the cross-sectional area of the pumping chamber (A_p) and the pressure in both pumping chambers. The equation of motion is

$$M\ddot{x} = P_k A_d + P_1 A_p - P_2 A_p - P_{avg} A_d - b\dot{x} \tag{10}$$

where M is the mass of the piston/rod assembly in the pumping section, P_k is the pressure in the driving chamber, P_{avg} is the pressure in the return chamber, P_1 and P_2 are the pressures in the upper and lower pumping chamber respectively, and b is a damping coefficient resulting from the viscous friction of the piston and rod.

The equation for the volumetric flow rate through a small cross-sectional area was used to determine the pressure P_1 and P_2. The volumetric flow rate is given by:

$$Q = A_v \sqrt{\frac{2}{\rho\varepsilon}(P_u - P_d)} \tag{11}$$

where A_v is the cross-sectional area of the valve opening, ρ is the density of the fluid, and ε is the dimensionless loss coefficient. Dependent on the direction the piston is moving, the upstream pressure and the downstream pressure are selected according to Table 2-3.

Table 2-3: Conditions for P_u and P_d

	sign of Q	Pumping chamber	P_u	P_d
$\dot{x} > 0$	-1	lower	P_2 via Eq. 12	P_s
$\dot{x} > 0$	1	upper	P_{atm}	P_1 via Eq. 13
$\dot{x} < 0$	1	lower	P_{atm}	P_2 via Eq. 13
$\dot{x} < 0$	-1	upper	P_1 via Eq. 12	P_s

The negative sign for the volumetric flow rate indicates that fluid is being pumped out of the pumping section while a positive sign indicates that fluid is pumped into the pumping section. By calculating the flow rate Q with the equation $Q = \dot{x}A_p$ and then setting P_u and P_d to the boundary conditions indicated in Table 2-3, the pressures in the upper and lower pumping chambers P_1 and P_2 can be found.

$$P_u = \left(\frac{\dot{x}A_p}{A_v}\right)^2 \frac{\rho\varepsilon}{2} + P_d \tag{12}$$

$$P_d = P_u - \left(\frac{\dot{x}A_p}{A_v}\right)^2 \frac{\rho\varepsilon}{2} \tag{13}$$

These dynamics fully describe the engine and pump section of the Stirling device. To further characterize the device, average output power is calculated by filtering the instantaneous power with a slow, unity-gain first order filter. The instantaneous power output $\mathbf{P}_{\text{instant}}$ is calculated by:

$$\mathbf{P}_{\text{instant}} = Q_{out}P_s \tag{14}$$

where $Q_{out} = A_p|\dot{x}|$ is the volumetric flow rate out of the two pumping chambers and P_s is the desired supply pressure.

Results

Results of the dynamic simulation show that the device can pump 1000 psig (7000 kPa) when the engine runs at 20 Hz (controlled sinusoidal motion of the displacer as given by Eqn. 2), is initially pressurized to 500 psig (3.55 MPa) with cold helium and is then held at a constant temperature T_h of 550°C on the hot side. The parameters for the Stirling pump as designed are given in Table 2-4.

Table 2-4: Parameters used in simulation

l_{cyl}	200 mm	l_{drive}	22 mm
$bore_{cyl}$	50 mm	$bore_{drive/return}$	60 mm
l_{piston}	76 mm	$bore_{pump}$	10 mm
d_{piston}	49 mm	d_{valve}	2.5 mm
		M	0.2 kg
		b	500 Ns/m

The pressure difference in the driving and return chamber (Fig.2-6) caused by the pressure swing inside the engine results in a displacement of the pumping piston as seen Fig. 2-7.

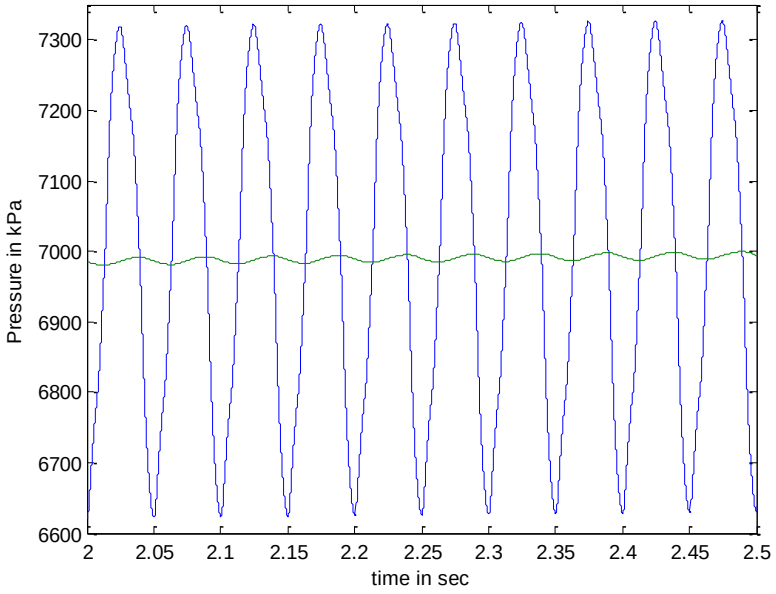

Figure 2-6: Driving (blue) and average (green) pressure vs. time

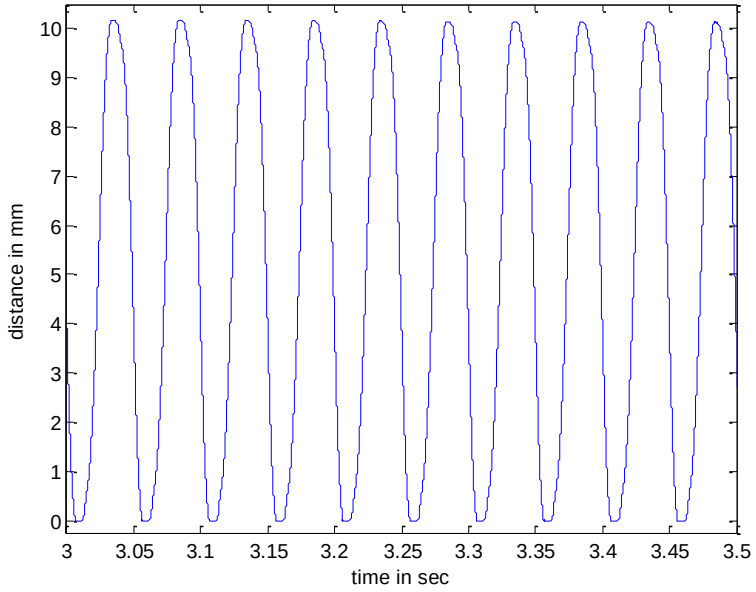

Figure 2-7: Displacement of the pumping piston with respect to time

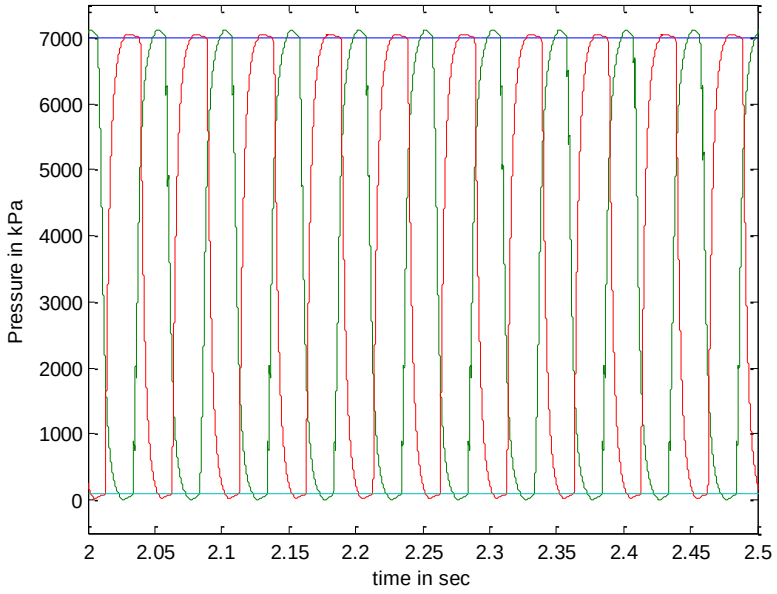

Figure 2-8: Pressure dynamics in the pumping chamber compared to the supply pressure (7 MPa) and atmospheric pressure (101kPa)

The pumping piston moves up and down in response to the engine and load pressures with a maximum displacement of about 10 mm. The pressure inside the pumping section is governed by the piston's velocity according to Equations 12 and 13 and under the conditions shown in Table 2-3. Figure 2-8 shows the pressure dynamics of P_1 and P_2 compared to supply and atmospheric pressure. If the pressure in either pumping chamber is greater than supply pressure, hydraulic fluid is pumping out of the pumping chamber. Conversely, if the pressure is below atmospheric pressure, hydraulic fluid is pumped into the pumping chamber. This is captured compactly as $Q_{out} = A_p|\dot{x}|$. An average power output of about 230 W can be achieved when operated at 20 Hz with a cold helium pre-pressurization of 500 psig.

Conclusion

In this paper the design and dynamic model of a second generation prototype Stirling pump is described. Taking into account observations and results from the generation 1 device, the proposed design changes for generation 2 are presented and justified. The heat transfer coefficient was greatly improved by using helium as the working fluid in the sealed pre-pressurized engine section. Simulation results are used to size the dimensions of the Stirling pump to achieve a high output power. A single-stage unit fulfills the energetic requirements set by the CCEFP for the Stirling pump of a hydraulic output power of 1000 psig and an average supply power ranging between 50W to 500W. The new design can greatly improve output power of the generation 1 device. Future work will formulate a controller for the efficient and precise oscillation of the displacer piston, build and run the engine/pump device, and validate the model with experimental data.

Acknowledgement

This work was supported by the Center for Compact and Efficient Fluid Power, an NSF Engineering Research Center, grant EEC-0540834.

References

[1] G. Walker, G. Reader, O. R. Fauvel, E. R. Bingham, *The Stirling Alternative: Power Systems, Refrigerants and Heat Pumps*, Gordon and Breach Science Publishers, 1994.

[2] G. Walker, “Large Free-Piston Stirling Engines,” Lecture Notes in Engineering, Springer-Verlag, pp.216-221, 1985.

[3] A. J. Organ, The Regenerator and the Stirling Engine, Mechanical Engineering Publications Limited, London, 1997.

[4] G. Walker, Stirling Engines, Oxford University Press, 1980.

[5] G. Walker and J. R. Senft, Lecture Notes in Engineering: Free Piston Stirling Engines, Springer-Verlag, New York, 1985.

[6] E. H. Cooke-Yarborough, E. Franklin, T. Gesow, R. Howlett, C. D. West, “Thermomechanical generator – an Efficient Means of Converting Heat to Electricity at Low Power Levels,” Proceedings of the IEE, no. 121, p. 749-751.

[7] C. D. West, Principles and Applications of Stirling Engines, Van Nostrand Reinhold Company, New York, 1986.

[8] C. D. West, Liquid Piston Stirling Engines, Van Nostrand Reinhold Company, New York, 1983.

[9] G. T. Reader and M. A. Clarke, “Liquid Piston Stirling Air Engines,” 2nd International Conference on Stirling Engines, 14p, 1984.

[10] M. E. Hofacker, N. Kumar, E. J. Barth. “Dynamic Simulation and Experimental Validation of a Single Stage Thermocompressor for a Pneumatic Anke-Foot Orthosis”. 2013 Proceedings of the 25th Symposium on Fluid Power and Motion Control, ASME/Bath, FPMC2013-4483, October 6-9, 2013, Sarasota, FL.

[11] J. Van de Ven, P. Gaffuri, B. Mies, and G. Cole, “Developments Towards a Liquid Piston Stirling Engine,” International Energy Conversion Engineering Conference, Cleveland, Ohio, 2008.

[12] S. K. Grinnell, “Flow of a Compressible Fluid in a Thin Passage”. ASME, 16 pages, 1954.

CHAPTER III.
MANUSCRIPT 2: DESIGN, MODEL, AND EXPERIMENTAL TESTING OF A STIRLING PRESSURIZER WITH A CONTROLLED DISPLACER PISTON

Anna Winkelmann, Eric J. Barth

Vanderbilt University
Nashville, TN

Submitted as a Regular Paper to the
IEEE/ASME Transactions on Mechatronics
(In Review)

Abstract

This paper presents the design, first-principles model, and experimental setup of a Stirling pressurizer. The Stirling pressurizer is a Stirling engine with an independently controlled displacer piston. The directly controlled, loose-fit displacer is actuated with a small linear motor and moves the pre-pressurized working fluid (helium) between the hot and cold side of the sealed engine section; therefore inducing a pressure change. The position of the displacer is the only control input to the first-principles model. The first-principles model is validated with experimental results for different controlled displacer piston motion profiles. Modeled and experimentally measured pressures are compared for average pressures ranging from 10 – 20 bar, and heater head temperatures ranging from 250°C – 500°C. The first-principles model is intended for: 1) the design and sizing of the pressurizer and power piston / power extraction, 2) specification of a displacer piston motion profile to optimize the efficiency and/or power output, and 3) the general design of Stirling devices, beyond the design of the experimental prototype investigated here, through the use of a lumped parameter model with well-defined and measurable parameters.

Introduction

A Stirling engine is a heat engine that can operate using a variety of heat sources such as high energy density hydrocarbon fuels (propane, butane, natural gas, etc.), solar concentrators, geothermal, radioisotope sources, or others. Stirling engines cyclically heat and cool a working fluid, inducing a pressure change which in turn drives a power unit. The Stirling engine was invented in 1816 by Robert Stirling and has long held the promise of being a clean, reliable, safe and quiet source of power. Stirling

engines were outperformed by other power sources such as electric motors and internal combustion engines. This was primarily due to the characteristically low power density of Stirling devices. These heavy engines with bulky kinematic arrangements produced proportionally small amounts of usable power.

In the twentieth century, advances in Stirling engines served to replace their kinematic arrangements with lightweight, small, purely dynamic elements. Such engines were called “free-piston Stirling engines.” This compact, new, and lightweight design held the promise of increasing the power density over its kinematic cousin. Nevertheless, this purely dynamic arrangement presented new challenges. The dynamic arrangements had to keep the engine self-oscillating, achieve the correct phase between the displacer and power piston dynamically, and robustly maintain self-oscillation in the face of load variations and disturbances. This is very difficult to achieve since free-piston Stirling engines utilize their own pressure change to drive the displacer piston. Self-oscillation is very sensitive to parametric properties of the engine and the load itself. Despite this, several free piston Stirling engines have been built and shown to work. Noteworthy examples include Beale’s free piston engines [1,2], the Harwell Thermomechanical Generator [2,3,4] and the liquid piston Fluidyne Stirling engine built by West [5,6]. Generally, the sensitivity to engine parameters is not well understood and results in a trial-and-error selection of engine specifications to arrive at acceptable parameters.

The Stirling pressurizer presented in this paper overcomes the difficulty of achieving the correct phase between the displacer and power pistons by directly controlling the motion profile of the displacer piston. By independently driving the displacer, the motion of the displacer is decoupled from the pressure dynamics within the engine. Ordinarily, the pressure and load influence the power piston which in turn drives the displacer piston through passive dynamics. By decoupling the displacer motion and then controlling it independently, the load does not affect the engine’s ability to self-oscillate. This additional control degree of freedom allows an independent design of the displacer piston motion that can be controlled to shape the thermodynamic cycle in the face of arbitrary loads. Avoiding the complex coupling between the displacer and power pistons in favor of a fully controlled device transforms a free-piston Stirling engine into a mechatronic Stirling engine.

Recent research in Stirling engines with a controlled displacer piston has been conducted in [7] and [8]. Both papers investigate whether a controlled displacer motion profile optimizes the thermodynamic cycle with regard to efficiency and/or power output of the engine. The work presented in this paper builds on the work of [7, 8] by using the position of the displacer piston as a control input to a first-principles model of a Stirling engine. An accurate, first-principles model that is amenable to deriving control laws for the displacer motion is critical for the line of work regarding controlled Stirling engines to continue. Furthermore, such a model needs to be rigorously validated experimentally. Although other papers [9, 10, 11] present control models of Stirling devices, many are not experimentally validated and none present a validated model that will accept an arbitrary displacer motion. The contribution of this paper is a first-

principles model, amenable to the direct control of the displacer piston, that is validated experimentally for a wide range operating conditions.

This paper presents and describes the design, dynamic model, and experimental setup of a Stirling pressurizer with a controlled displacer. The Stirling pressurizer presented in this paper has no power piston attached, which allows isolation and experimental validation of the complex pressure dynamics of the engine. The dynamic model is validated with experimental data for two directly controlled motion profiles of the displacer piston, a variety of heater head temperatures, and a variety of different average engine pressures.

Design

The device has two chambers, namely a sealed engine section that uses pre-pressurized helium as its working fluid for enhanced efficiency and power density, and a return chamber. A cross-section of the engine design is shown in Fig. 3-1. This engine section is referred to as a Stirling pressurizer since it is intended as the portion of a Stirling engine responsible for generating large pressure oscillations that can subsequently be used by a power piston connected at the “power connection ports” to output work. The sealed engine section contains a loose-fit displacer piston (radial clearance of 0.4 mm). The displacer is connected to the linear motor via an extension rod and a shaft coupling which offsets small angular and lateral misalignment. The linear motor moves the displacer piston between the hot side (toward the heater head) and cold side (toward the cooling fins) and in turn shuttles the helium gas. The resulting temperature change of the helium gas produces a pressure change inside the engine section.

The return chamber is kept at an average pressure. This is achieved through a flow restriction induced by a needle valve which connects the cold side of the engine section with the return chamber (needle valve not shown in Fig. 3-1). Two ports, one on the cold side of the engine section and one on the return chamber, are installed to connect a power unit with a power piston to the pressurizer. This power unit could be anything that can be driven by a pressure change such as a hydraulic pump, a linear electric generator, a reciprocating piston compressor, or a high pressure water filtration system, among others.

The selection of the working fluid inside the engine section is of importance in order to achieve good performance and high efficiency. Gases of significant interest for the working fluid inside the engine section are air, helium and hydrogen. Air is of significant interest since it is readily available and easier to seal within the engine than helium or hydrogen. Nevertheless, the heat transfer properties of air don’t allow an air operated engine to compete with internal combustion engines [1]. Therefore, gases with superior heat transfer properties and low viscosities, such as helium or hydrogen, need to be used. Even though hydrogen has better heat transfer properties, it is highly combustible in the presence of air. Therefore, helium was selected due to its good thermophysical characteristics such as its high heat transfer coefficient and its relatively low viscous flow losses. The heat transfer coefficient of helium is about 11 times higher than that of air in the pressure and temperature range the engine is operating.

The heater head of the engine section is made from stainless steel. For this prototype, electric cartridge heaters were chosen such that accurate temperature control of the heater head is provided. Eight tight fit holes for the insertion of cartridge heaters guarantee good conduction between the heaters and the heater head such that the working fluid on the hot side can be heated up to a maximum of 600°C. The hot and cold sides of the engine section are connected via an Inconel cylinder. Inconel was selected due to its high melting point, and its low thermal conductivity. Low thermal conductivity is important since the heat flow from the hot to the cold side along the engine section needs to be as small as possible. Another advantage of Inconel among other materials is that it can be welded to the heater head; therefore providing sealing of helium at high temperatures. To keep helium sealed within the device, static and dynamic O-rings were carefully selected. Two static seals are used on the cold side, one on the bottom cap that bolts to the cooling fins (Parker part no. OR2-228-V9975), and one at the flange on the return chamber (Parker part no. OR2-230-V1475). One dynamic seal is used to seal around the extension rod (Parker part no. O2-006-V9975).

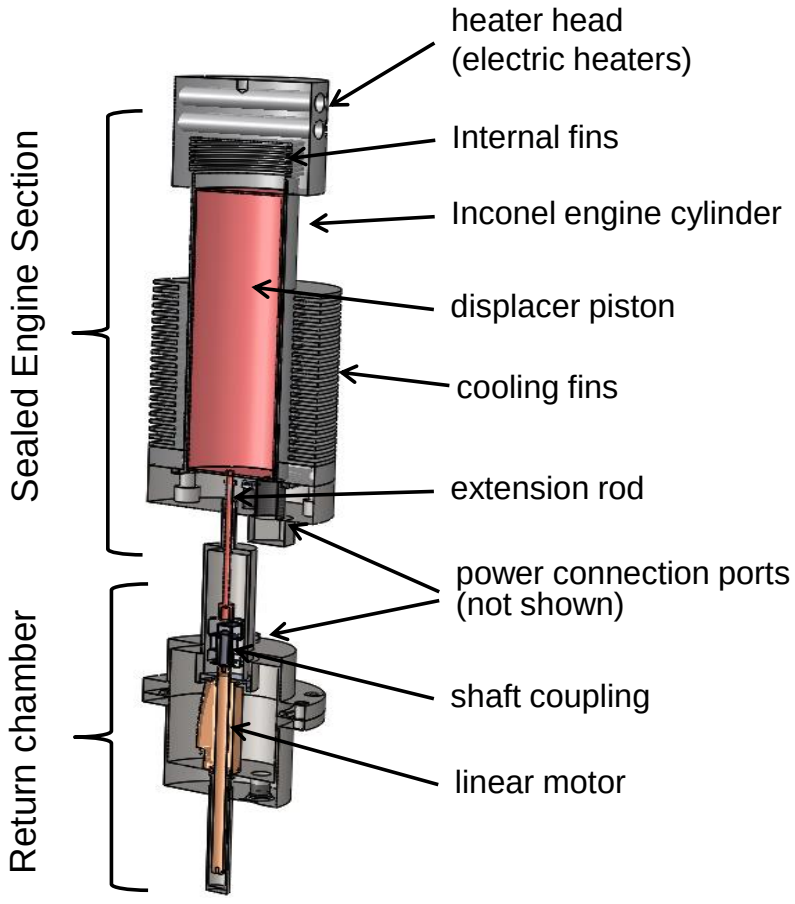

Figure 3-1: Design of the Stirling pressurizer

Internal fins inside the heater head and external fins on the cold side of the engine section increase the area for heat transfer in and out of the system, respectively. Thermal conduction along the displacer piston and the Inconel cylinder are minimized by reducing the wall thicknesses such that it will withstand the exposed pressure without failing or deforming significantly. For the displacer design, not only the wall thickness but also the length of the displacer is important for thermal isolation of the cold and the hot section. A length of three times the diameter was chosen for the displacer piston, since good results on other Stirling devices have been recorded for that aspect ratio [1]. The annular gap between the displacer piston and the Inconel cylinder serves as the flow passage of the working fluid and also forms the regenerator. In most small, low-speed engines it has been found that a formal regenerator as seen in most larger Stirling engines has proven inadequate due to its large dead volume. Instead, small Stirling engines often rely on the annular gap connecting the cold and the hot side such as in Beale's small free-piston engines [1]. Guidelines say that the gap should be between 0.38 and 0.76 mm to minimize thermal conduction losses and to maximize the working fluid's wall contact without increasing the flow restriction too much [1]. For this prototype a gap of 0.4 mm was selected. The reciprocating motion of the displacer piston moves the working fluid back and forth between the hot and cold control volumes. When the working fluid is in the regenerative channel, the fluid liberates or absorbs heat from the displacer and cylinder walls, depending on the direction the fluid is moving. When the fluid is moving downward from the hot to the cold side of the engine section, heat is transferred from the fluid to the walls. Consequently, the fluid leaves the channel at a lower temperature $T_{reg,k}$. Conversely, when the working fluid moves upward, the fluid absorbs heat from the walls and leaves the channel at a higher temperature $T_{reg,h}$.

Dynamic Model

The only exogenous input to the dynamic model is the position of the displacer piston which is determined by the position *f(t)* of the linear motor which is rigidly attached to the displacer. This position function is the result of the linear motor tracking a reference trajectory through any variety of feedback control. The position input to the model is arbitrary; for experimental validation, the response to a sinusoidal and a square wave reference input was chosen. The position of the displacer piston is given by:

$$x_d = \frac{l_{stroke}}{2} + \frac{l_{stroke}}{2} f(t) \tag{1}$$

where l_{Stroke} is the stroke length of the displacer piston in the engine section. The velocity of the displacer is accordingly given by:

$$v_d = \frac{l_{Stroke}}{2} \dot{f}(t) \tag{2}$$

With the position and velocity of the displacer piston known, the engine section can be modeled as two control volumes of variable size, namely the hot control volume (V_h) and the cold control volume (V_k) (Fig.

3-2). In each control volume convection between the walls of the engine housing and the working fluid is present. The walls of the hot control volume (V_h) transfer thermal energy from the heat source to the working fluid while the working fluid in the cold control volume (V_k) transfers thermal energy to the cylinder wall and cooling fins out to the surroundings. The dead volume surrounding the displacer piston is equally added to either control volume V_h and V_k. The dead volume due to the internal fins at the heater head is also incorporated to the control volume of the hot side.

A. Pressure Dynamics

The pressure dynamics in each control volume were derived from a fundamental power balance resulting from the first law of thermodynamics, given by

$$\dot{U} = \dot{H} + \dot{Q} - \dot{W} \tag{3}$$

Expanding and rearranging terms, the pressure dynamics in each control volume as influenced by heat flux, enthalpy, and volume changes can be found. The pressure dynamics of each control volume (*h*: hot side, *k*: cold side, *r*: return chamber) is given by:

$$\dot{P}_h = \frac{\sum(\dot{Q}_{in} + \dot{Q}_{loss,h})(\gamma_{He} - 1) + \dot{m}\gamma_{He}RT_{flow} - \gamma_{He}P\dot{V}_h}{V_h} \tag{4a}$$

$$\dot{P}_k = \frac{\sum(\dot{Q}_{in} + \dot{Q}_{loss,k})(\gamma_{He} - 1) + \dot{m}\gamma_{He}RT_{flow} - \gamma_{He}P\dot{V}_k}{V_k} \tag{4b}$$

$$\dot{P}_r = \frac{\sum\dot{Q}_{out}(\gamma_{He} - 1) + \dot{m}_r\gamma_{He}RT_{flow,r} - \gamma_{He}P_r\dot{V}_r}{V_r} \tag{4c}$$

where T_{flow} is the temperature of the gas that is entering/leaving the control volume, dependent on the pressure difference between the hot and cold sides and the direction the displacer is moving. The mass flow rate into or out of the control volume is denoted by $\dot{m}$, with a positive sign convention for mass flowing into the control volume. The heat transfer rate between the heat source and the working fluid (in), or between the working fluid and the cooling fins (out), is denoted $\dot{Q}_{in/out}$, where the sign convention is always positive for heat entering the control volume. The conduction and shuttle heat transfer losses are denoted $\dot{Q}_{loss}$, with a positive sign convention for heat entering the control volume.

Figure 3-2 is an overview of the system dynamics. These system dynamics are dependent on the terms in Eqns. (4a), (4b), and (4c) for each of the three control volumes: hot side, cold side, and return chamber, respectively. For the experimental validation presented, the $\dot{V}_r$ term in equation (4c) is zero. More generally, it is included in the model to account for a power piston that would utilize the pressure in the return chamber. A fourth control volume represents the regenerative channel (to be presented). The dynamics of each control volume describes their interaction with external conditions as well as with the other control volumes. The dynamic dependencies of each control volume are described below.

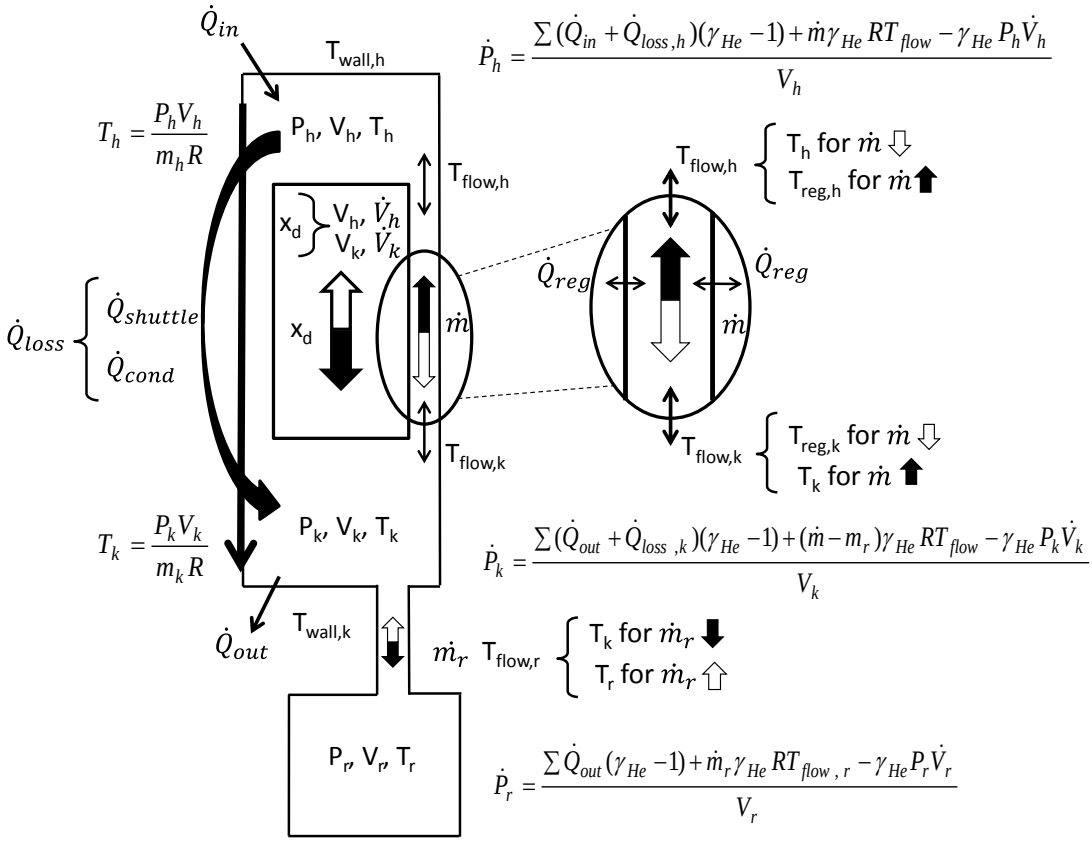

Figure 3-2: A System overview of all the dynamics taking place within the pressurizer. This diagram illustrates dynamic interactions within the system

B. Mass Flow

The mass flow rate $\dot{m}$ is calculated using the Navier-Stokes equation and the volumetric flow rate equation, as is done in [9]. The Navier-Stokes equation for quasi steady, incompressible, fully developed, annular flow given by

$$\frac{1}{\mu}\frac{dP}{dz} = \frac{1}{r}\frac{\partial}{\partial r}\left(r\frac{\partial v_z}{\partial r}\right) \tag{5}$$

where μ and ρ are the dynamic viscosity and the density of the fluid, respectively. Integrating equation (5) and using the following boundary equations 1) $v = v_d$ at $r = r_d$, and 2) $v = 0$ at $r = r_{cyl}$, the velocity profile v_z is given by

$$v_z = \frac{1}{4\mu}\frac{dP}{dz}\left[r^2 - r_{cyl}{}^2 - \frac{\left(r_{cyl}^2 - r_d^2\right)}{\ln\left(\frac{r_{cyl}}{r_d}\right)}\ln\frac{r}{r_{cyl}}\right] + \frac{v_d(t)}{\ln\frac{r_{cyl}}{r_d}}\left(\ln\frac{r_{cyl}}{r}\right) \tag{6}$$

Substituting *dP/dz* with $(P_h\text{-}P_k)/l_{cyl}$ and using the volumetric flow rate equation and the density of the fluid, the mass flow equation yields:

$$\dot{m} = \frac{\rho\pi}{8\mu}\left(-\frac{P_h - P_k}{l_{cyl}}\right)\left[r_{cyl}^4 - r_d^4 - \frac{\left(r_{cyl}^2 - r_d^2\right)^2}{\ln\left(\frac{r_{cyl}}{r_d}\right)}\right] - \frac{2\pi v_d(t)\rho}{\ln\frac{r_{cyl}}{r_d}}\left[\frac{1}{2}\left(r_{cyl}^2 \ln r_{cyl} - r_d^2 \ln r_d\right) - \frac{1}{4}(r_{cyl}^2 - r_d^2)\right] + \frac{2\pi v_d(t)\rho \ln r_{cyl}}{\ln\left(\frac{r_{cyl}}{r_d}\right)}\left[\frac{1}{2}r_{cyl}^2 - \frac{1}{2}r_d^2\right] \tag{7}$$

The sign convention for the mass flow rate is determined positive when the fluid enters the hot control volume and leaves the cold control volume such that $\dot{m}_h = \dot{m}$ and $\dot{m}_k = -\dot{m}$.

The mass flow between the return chamber and the cold side of the engine section is calculated using Bernoulli's equation. Assuming steady-state, incompressible, inviscid, laminar flow, the mass flow rate is given by

$$\dot{m}_{orifice} = \rho c_d A_{orifice}\sqrt{\frac{1}{1-\beta^4}}\sqrt{\frac{2(P_{high} - P_{low})}{\rho}} \tag{8}$$

where c_d is the discharge coefficient, $A_{orifice}$ is the orifice area and β is the ratio of orifice diameter and diameter of the pipe. The driving pressures P_{high} and P_{low} are given by:

$$\begin{aligned} P_{high} &= \max(P_k, P_r) \\ P_{low} &= \min(P_k, P_r) \end{aligned} \tag{9}$$

The mass flow rate into and out of the return section is therefore given as:

$$\dot{m}_r = \text{sign}\,(P_k - P_r)\dot{m}_{orifice} \tag{10}$$

C. Heat transfer

The heat transfer rate due to convection with the engine walls within each control volume is governed by:

$$\dot{Q}_{in/out} = h_{He} A_{h,k,r} \left(T_{wall,h,k,r} - T_{h,k,r} \right) \tag{11}$$

where $A_{h,k,r}$ is the surface area for heat transfer in each control volume and h_{He} is the heat tranfer coefficient for helium. On the hot side and the cold side of the engine the heat transfer rate is limited by the rated output power of the electric heaters and the effectivness and thermal resistance of the cooling fins, respectively. The heat transfer coefficient is estimated by performing a fully developed pipe flow analysis simular to [12]. The Nusselt number given by

$$Nu = \frac{h_{He}\delta}{k_{He}} = a \cdot \mathrm{Re}^m \cdot \mathrm{Pr}^n \tag{12}$$

is used to solve for the heat transfer coefficient h_{He}. *Pr* is the Prandtl number and *a, m, n* are constants from the Dittus-Boelter equation for turbulent flow (Table I). The Prandtl number for helium over a wide range of temperatures is about 0.7. The characteristic length δ is given by

$$\delta = \frac{4A_c}{C} \tag{13}$$

where A_c and *C* are the cross-sectional annular area of the gap in between the displacer piston and the housing cylinder, and the wetted perimeter given by the interior circumference of the housing cylinder, respectively. The Renolds number *Re* depends on the frequency of the displacer piston. It is calculated using

$$\mathrm{Re} = \frac{\dot{x}_m \delta}{\nu} \tag{14}$$

where *v* is the kinematic viscosity of the working fluid and $\dot{x}_m$ is mean velocity of the working fluid which is dependent on the frequency and travel of the displacer piston.

The major heat transfer losses within the engine are the shuttle heat transfer losses and the internal conduction losses along the engine cylinder wall. The heat transfer equation for these losses is given by:

$$\dot{Q}_{loss} = \dot{Q}_{shuttle} + \dot{Q}_{cond} \tag{15}$$

The shuttle heat transfer losses occur due to the reciprocating motion of the displacer piston and the temperature distribution along the walls of the displacer and housing cylinder. When the displacer piston is at top dead center, the temperature profile along the displacer and the wall are similar, but when the displacer piston moves down, the temperature profile of the displacer piston is greater than that of the engine wall. Consequently heat will be transferred to the cold side of the engine section. This thermal effect is generally termed “shuttle losses”. The shuttle heat transfer loss is estimated to be [1]:

$$\dot{Q}_{shuttle} = \frac{0.4 l_{stroke}^2 k_{He} d_{displacer} \left(T_{wall,h} - T_{wall,k} \right)}{S\, l_{displacer}} \tag{16}$$

where *S* is the radial gap given by $r_{cyl} - r_d$. Figure 3-3 illustrates this phenomenon. The temperature profile of the engine housing is a result of the conduction along the cylinder wall between the hot and the cold side. These conduction losses are given by:

$$\dot{Q}_{cond} = \frac{k_{Inconel} \pi d_{cyl} t_{cyl} (T_{wall,h} - T_{wall,k})}{l_{cyl}} \tag{17}$$

where d_{cyl} and t_{cyl} is the diameter and thickness of the housing cylinder respectively. Given that the total heat flux of equation (15) is positive with positive values for both terms given by equations (16) and (17), The sign conventions of the control volumes are given as $\dot{Q}_{loss,h} = -\dot{Q}_{loss}$ and $\dot{Q}_{loss,k} = \dot{Q}_{loss}$.

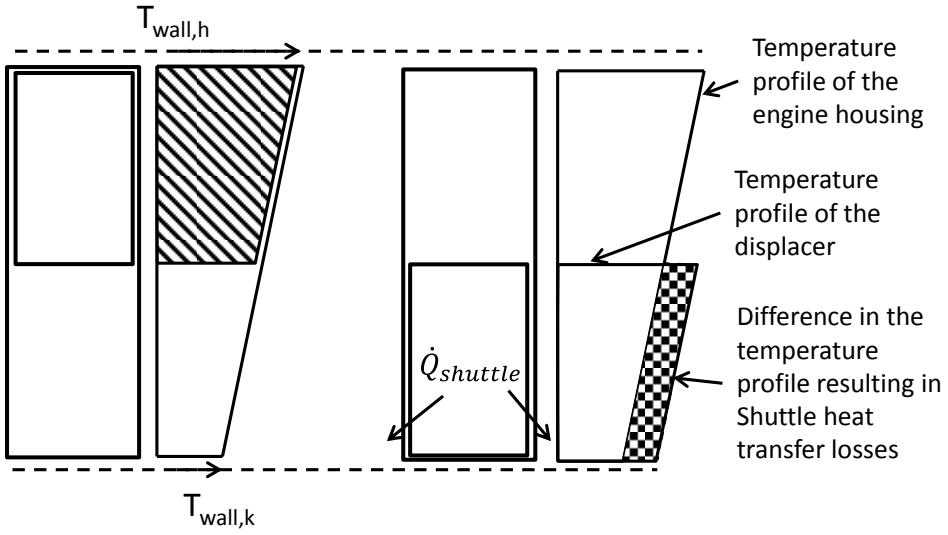

Figure 3-3: Diagram explaining the shuttle heat transfer

D. Regenerative Channel

The regenerative channel uses the first law of thermodynamics in the absence of work and internal energy storage to determine the heat transfer rate between the fluid and the walls of the regenerative channel. The heat transfer rate is given by:

$$\dot{Q}_{reg} = -\dot{m}(h_{in} - h_{out}) \tag{18}$$

where h_{in} and h_{out} are the specific enthalpies at the entry and exit of the regenerative channel, respectively, and $\dot{m}$ is given by Equation (7). The specific enthalpies are calculated using:

$$h = c_p T \tag{19}$$

where c_p is the specific heat at constant pressure and T is the temperature of the working fluid at the associated location. The temperature of the inlet or outlet fluid is dependent on the flow direction. The outlet temperature depends on the effectiveness of the regenerative channel. The effectiveness of the regenerative channel is stated as:

$$\varepsilon = \frac{\text{actual enthalpy change}}{\text{maximum theroretical enthalpy change}} \tag{20}$$

The outlet temperature is calculated using an assumed effectiveness. The outlet temperatures depending on the direction of fluid flow is given by

$$T_{reg,k} = T_h + \varepsilon\left(T_k - T_h\right) \quad for\ \dot{m} < 0 \tag{22a}$$

and

$$T_{reg,h} = T_k + \varepsilon\left(T_h - T_k\right) \quad for\ \dot{m} > 0 \tag{22b}$$

where $T_{reg,k}$ is the outlet temperature of the regenerative channel on the cold side, $T_{reg,h}$ is the outlet temperature of the regenerative channel on the hot side, and $\dot{m}$ is given by Equation (7). These regenerator fluid temperatures then determine the following flow temperatures used for Equations (4a) and (4b) applied to the hot and cold sides as follows:

$$T_{flow,h} = \begin{cases} T_h \text{ for } \dot{m}_h < 0 \\ T_{reg,h} \text{ for } \dot{m}_h > 0 \end{cases} \tag{23a}$$

$$T_{flow,k} = \begin{cases} T_k \text{ for } \dot{m}_k < 0 \\ T_{reg,k} \text{ for } \dot{m}_k > 0 \end{cases} \tag{23b}$$

Experimental Validation of the Model

A. Experimental Setup

The Stirling device was tested in a laboratory fume hood surrounded by half inch thick stainless steel plates. Figure 3-4 shows the Stirling pressurizer instrumented within the fume hood.

For data acquisition, Matlab Simulink was used in conjunction with a Real-Time Windows target machine. The target machine housing one data acquisition board is located outside of the fume hood.

Eight electric Firerod Cartridge Heaters (Watlow part no. G2J110-N24H) and a temperature controller (Watlow part no. PM6C1CH) were used to regulate the temperature on the hot side of the engine. The manufacturers' recommended hole fit for the insertion of the heaters into the heater head for good conduction was followed. To gather temperature and pressure dynamics, a type K thermocouple (Nunmac part no. C2-7) and a pressure sensor (PCB part no. 112A05) were installed on the cold side of

the engine section (see. Fig 3-4). The thermocouple is a right-angle ribbon thermocouple especially suitable to measure temperatures of gasses and liquids at high pressure with a one millisecond response time. To ensure that the working fluid is totally sealed within the engine section and cannot escape through the thermocouple port, the thermocouple was welded to the engine housing. An instrumentation amplifier (AD 595) was used to amplify the signal of the thermocouple. The pressure sensor (PCB 112A05) used on the cold side of the engine section was a high-precision charge mode pressure sensor that uses the piezoelectric properties of quartz to convert an applied pressure into its analog electric output. An IN-Line charge converter (PCB part no. 422E53) and a single-channel, line-operated signal conditioner (PCB part no. 482A21) was used to convert the sensor's high impedance charge signal to a low impedance voltage signal and to decouple the signal from the DC bias voltage, respectively. To minimize sensor noise, the sensor was connected to the charge converter using a coaxial cable (PCB part no. 003A03).

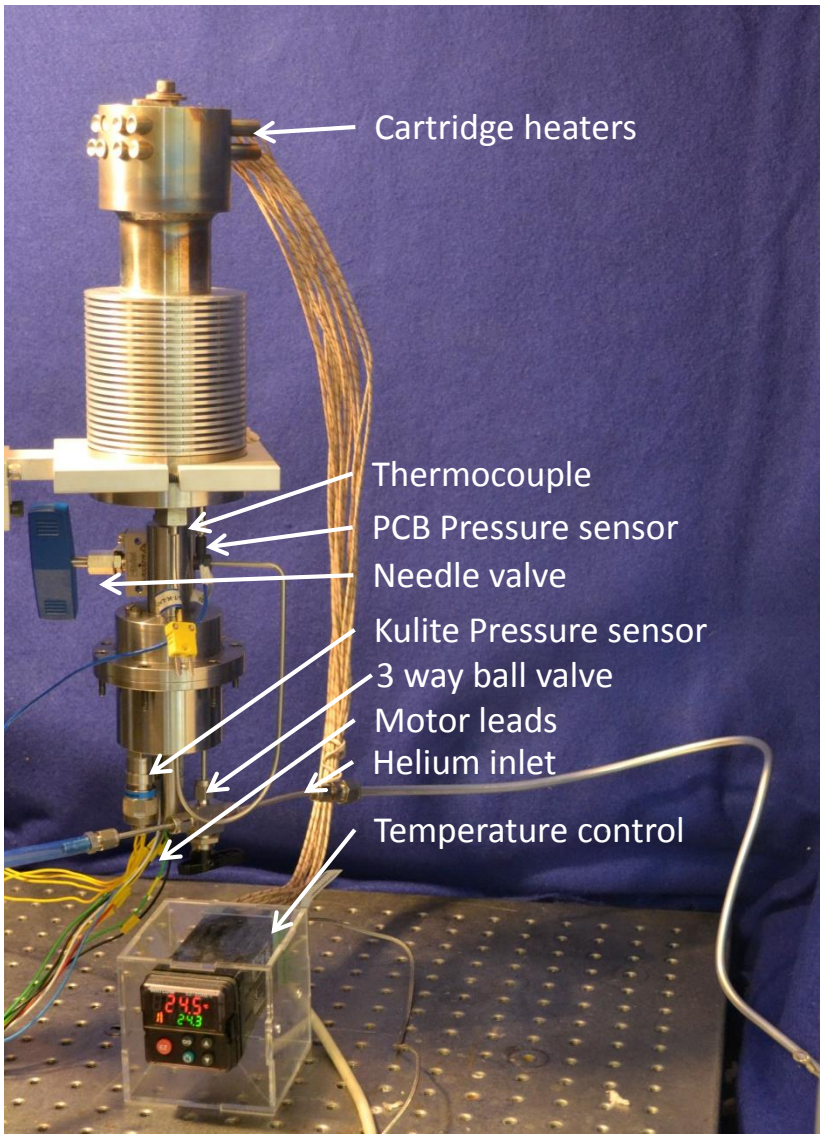

Figure 3-4: Experimental setup

The return chamber is connected to the engine section via a 1/8 inch stainless steel tube and needle valve (Parker part no. 10V2072) (partially obscured in Fig. 3-4). The return chamber houses another pressure sensor, a linear motor and a 3-way ball valve. The pressure sensor (Kulite part no. HEM-59-375-1000A) is used for high temperature, high frequency measurement applications. An instrumentation operational amplifier (AD 624) was selected to precisely amplify the signal with common-mode noise rejection. The 3-way ball valve (Swagelok part no. XX-41GXS1) was used to either purge air out of the engine section, to fill the engine with high purity helium for experimental testing, or to seal the engine closed.

The linear motor (Faulhaber part no. LM 1247) is a DC-Servomotor. To control the output position of the motor, the Faulhaber motion controller (MCLM 3003/06) and its Motion Manager software was used. A Sub-D Type connector (Ceramtec part no. 16800-01-W) hermetically feeds the electric wires of the

motor out of the pressurized return chamber to the surroundings. A command input from Matlab Simulink into the motion controller excites the motor. The actual and the target position of the motor can be extracted from the motion manager software. The actual position of the motor was used as the input to the dynamic model.

An infrared picture was taken with a thermographic camera (Fluke part no. 676-FLK-TI40060Hz) to illustrate the temperature distribution of the engine section (Fig. 3-5). As seen in Fig. 3-5 the temperature gradually decreases when moving toward to the cold side of the engine section. The cartridge heaters heat the heater head up to a desired temperature (up to a maximum temperature of 600°C). The cooling fins and the Inconel cylinder absorb heat from the working fluid and transfer it to the surroundings.

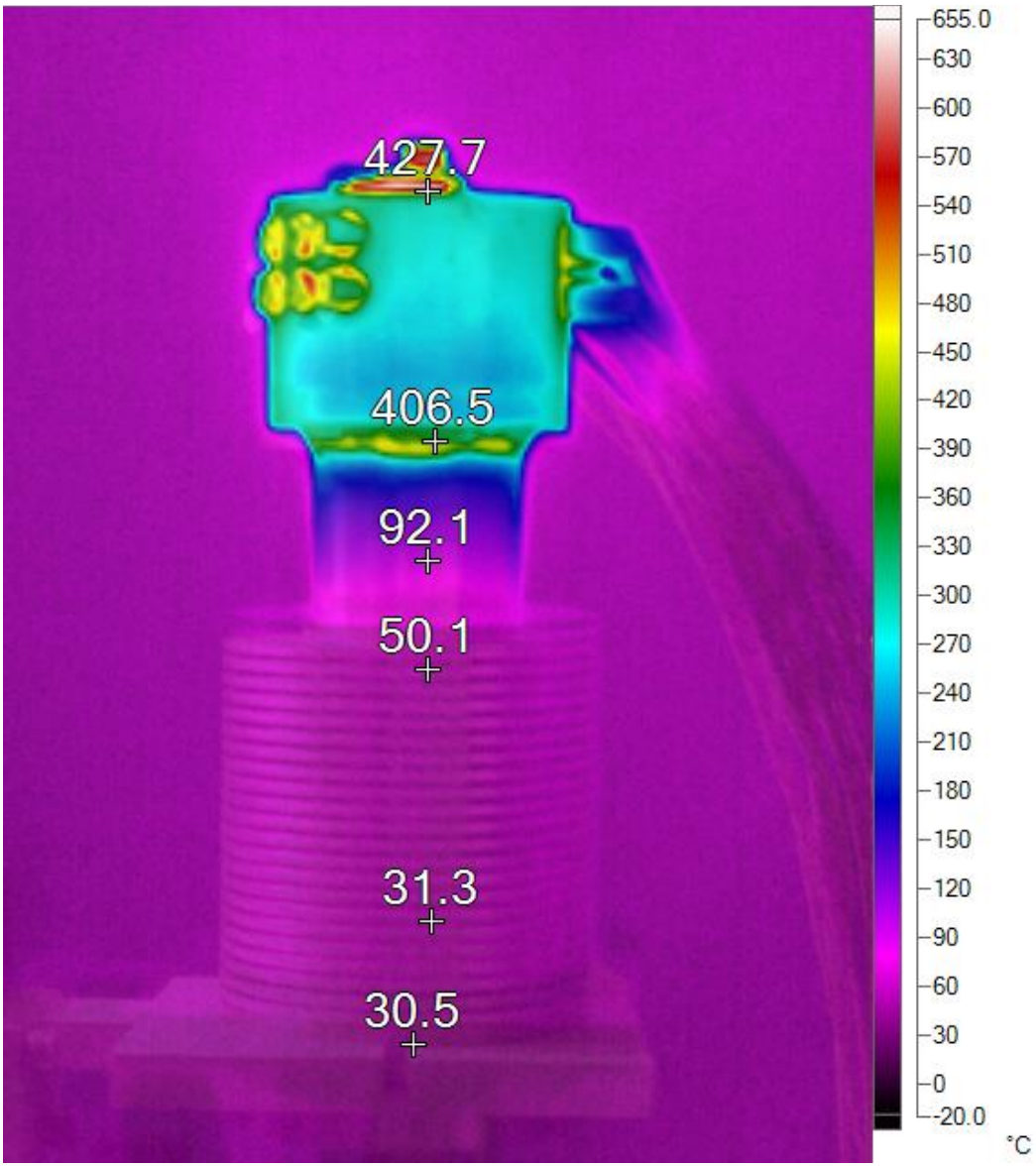

Figure 3-5: Thermographic image of the engine section

B. Engine Parameters

The dynamic model was validated by taking data for different displacer motion profiles and frequencies, different average engine pressures and different heater head temperatures. A sinusoidal motion profile and a step function motion profile were chosen for the displacer. Table 3-1 shows the engine parameters for this prototype.

Table 3-1: Engine Parameters

maximum stroke length	l_{stroke}	23.5 mm
length of displacer	$l_{displacer}$	143.5 mm
length of housing cylinder	l_{cyl}	167 mm
thickness of cylinder	t_{cyl}	1.245 mm
thickness of displacer piston	t_d	0.889mm
diameter of displacer	$d_{displacer}$	47.5 mm
diameter of cylinder	d_{cyl}	48.31 mm
radial gap	S	0.405 mm
gas constant for Helium	R	2070 J/kg/K
thermal conductivity of He	k_{He}	0.2114 W/m/K
thermal conductivity of Inconel	$k_{Inconel}$	10.1 W/m/K
ratio of specific heats for He	γ_{He}	1.664
constant pressure specific heat for Helium	c_p	5196 J/kg/K
Prandtl Number	Pr	0.7
from Dittus-Boelter equation	a	0.023
from Dittus-Boelter equation	m	0.8
from Dittus-Boelter equation	n	0.3
Needle valve discharge coefficient	c_d	0.7

C. Tuned Model Parameters

Given all of the model parameters, the only two that are unknown for the dynamic model are the effectiveness of the regenerator and the orifice area induced by the needle valve. In order to estimate the orifice area of the manually adjustable needle valve (that has no demarcations), the modeled pressure within the return chamber determined by Equation (4c) was adjusted by tuning $A_{orifice}$ in Equation (8) such that it fit the measured pressure in the return chamber. Figure 3-6 compares the modeled and actual measured pressure change inside the return chamber when the heater temperature was set to 500°C and a displacer frequency of 2 Hz. The orifice diameter was found to be about 0.5 mm. Estimating the orifice area from Equation (4c) and Equations (8-10) separates much of the dynamics in the upper portion of the engine from the estimate since P_k is measured and used directly as the driving function. It should also be noted that $A_{orifice}$ is a physically meaningful parameter that can be measured directly.

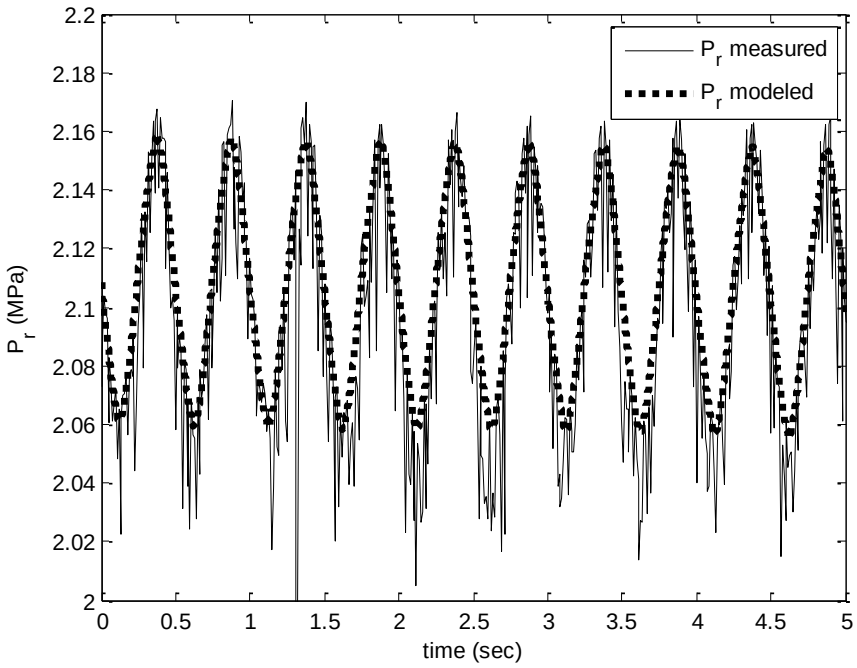

Figure 3-6: Orifice area was adjusted such that modeled and measured pressure inside the return chamber would be the same.

The effectiveness depends on the annular gap between the displacer piston and the housing cylinder and the length of the displacer piston. Based on the long displacer piston and the small gap, the effectiveness of the regenerator was selected similarly to [9] to be 0.8.

D. Sinusoidal Displacer Motion

For a sinusoidal displacer motion profile, data was taken at different heater head temperatures of 250°C, 350°C, 450°C, and 500°C. For each of these temperatures the engine was run at three different average pressures and two different frequencies namely, 10bar, 15bar, and 20bar and, 1Hz and 2Hz. The actual positon of the motor and therefore the displacer's position as measured by the linear motor's position sensor was used as the input to the model. The engine was allowed to run for a duration adequate for it to come to steady-state operating condition before the data were taken. The modeled and measured pressure P_k inside the engine section is compared in Fig. 3-7 and Fig.3-9. Tables 3-2 and Table 3-3 compare measured and modeled pressure ratios of maximum and minimum P_k for other data taken that are not shown graphically. The measured and modeled pressures P_k agree within a few percent over a wide range of different average pressures, heater head temperatures, and displacer frequencies.

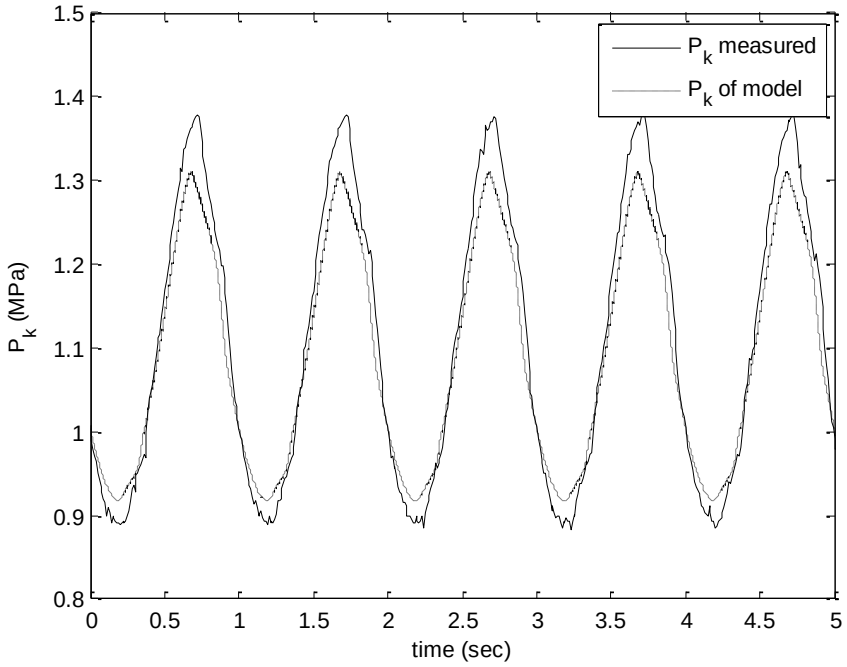

Figure 3-7: Measured and modeled pressure P_k inside the engine section at low heater head temperature (250°C), low pressure (10 bar), and at a frequency of 1 Hz. The modeled pressure ratio is about 7% lower than measured pressure ratio.

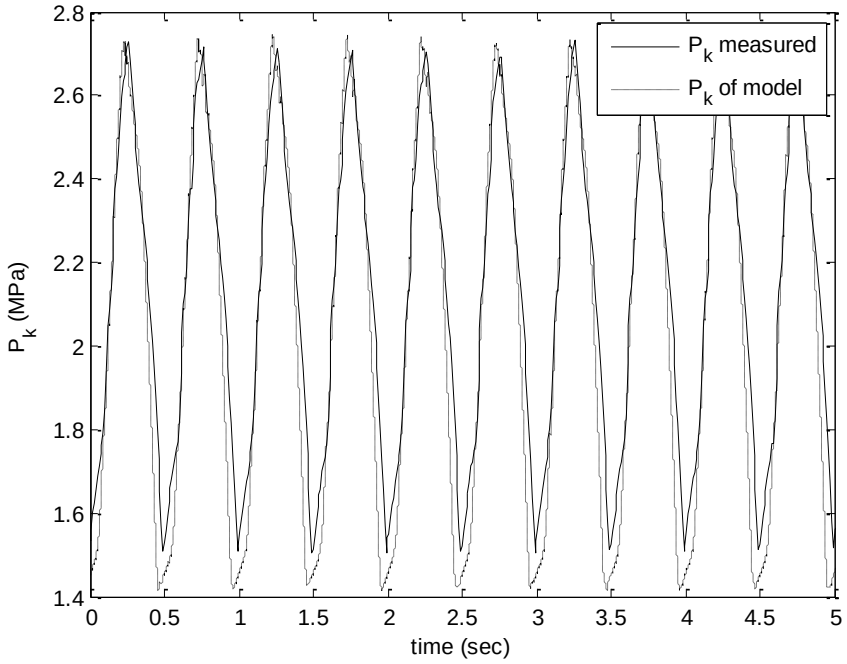

Figure 3-8: Measured and modeled pressure P_k inside the engine section at 450°C heater head temperature, high pressure (20 bar), and at a frequency of 2 Hz. The modeled pressure ratio is about 3% higher than measured pressure ratio.

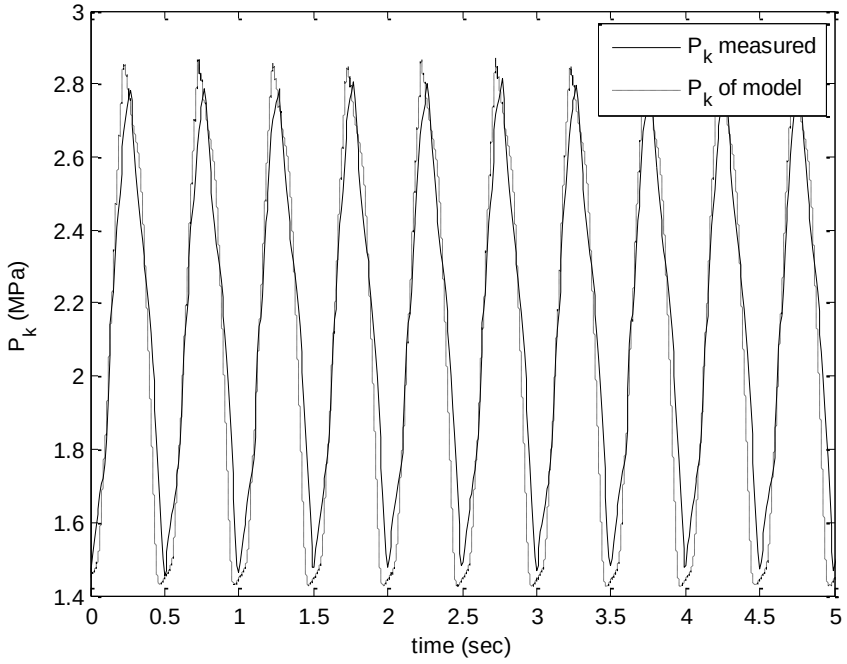

Figure 3-9: Measured and modeled pressure P_k inside the engine section at high heater head temperature (500°C), high pressure (20 bar), and at a frequency of 2 Hz. The modeled pressure ratio is about 4.6% higher than measured pressure ratio.

Table 3-2: Pressure ratio of experimental and modeled data at 1 Hz

1Hz	250°C		350°C		450°C		500°C	
10bar	1.53	-7.14	1.62	-4.48	1.78	3.26	1.79	5.07
	1.42		1.55		1.84		1.88	
15bar	1.52	-6.43	1.63	-2.44	1.76	3.92	1.77	4.62
	1.42		1.59		1.83		1.85	
20bar	1.49	-2.41	1.56	1.93	1.56	6.87	1.76	3.45
	1.45		1.59		1.67		1.82	

Key for Tables 3-2 and Table 3-3:

Experimental $\overline{P}_{k,\max} / \overline{P}_{k,\min}$	% Error
Modeled $\overline{P}_{k,\max} / \overline{P}_{k,\min}$	

Table 3-3: Pressure ratio of experimental and modeled data at 2 Hz

2Hz	250°C		350°C		450°C		500°C	
10bar	1.55	-9.84	1.74	-3.44	1.89	-3.51	1.87	7.71
	1.40		1.68		1.82		2.01	
15bar	1.54	-3.76	1.70	-2.13	1.86	1.82	1.89	6.00
	1.48		1.66		1.89		2.00	
20bar	1.48	0.82	1.66	2.71	1.86	2.82	1.89	4.61
	1.49		1.70		1.92		1.98	

E. Non-sinusoidal Displacer Motion

Part of the motivation for casting a dynamic model of the Stirling pressurizer was to be able to study various displacer motion profiles. A model that adequately captures differences with regard to different displacer motion profiles would allow a model-based optimization of the displacer motion for maximum efficiency, power, or other metrics discernable from the model. This section presents a model validation for a non-sinusoidal displacer motion. The displacer piston's linear motor was given a filtered square wave reference input command to track. Figure 3-10 shows the resulting motion profile. Data were gathered for a heater head temperature of 450°C and at pressures and frequencies of 15 bar and 20 bar and 1Hz and 2Hz, respectively; all other conditions were the same as those for the sinusoidal motion tests. The actual and modeled cold-side pressure was compared. Figure 3-11 can be compared to Fig. 3-8 and shows that the model captures differences between the two motion profiles.

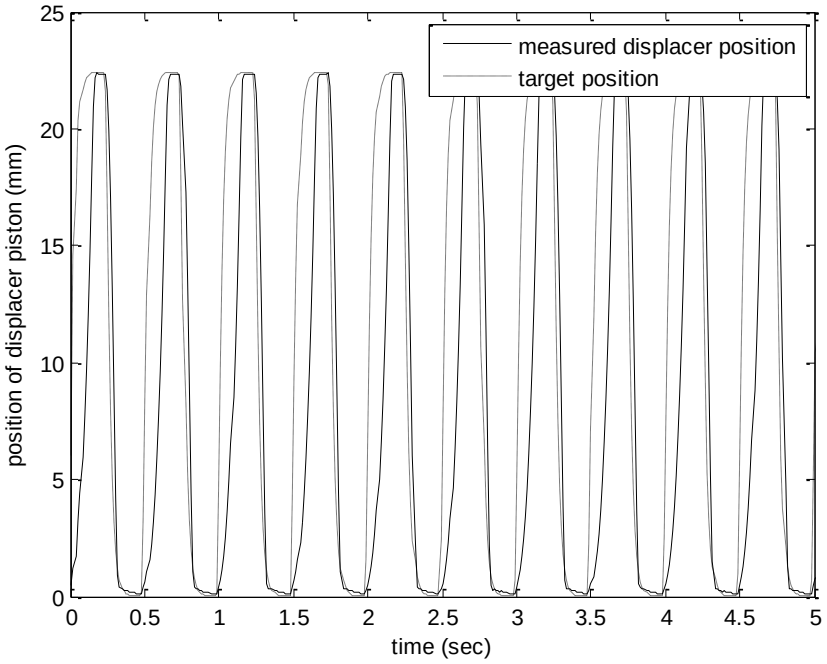

Figure 3-10: Filtered square wave motion profile of the displacer piston at 450°C, 20bar and 2Hz

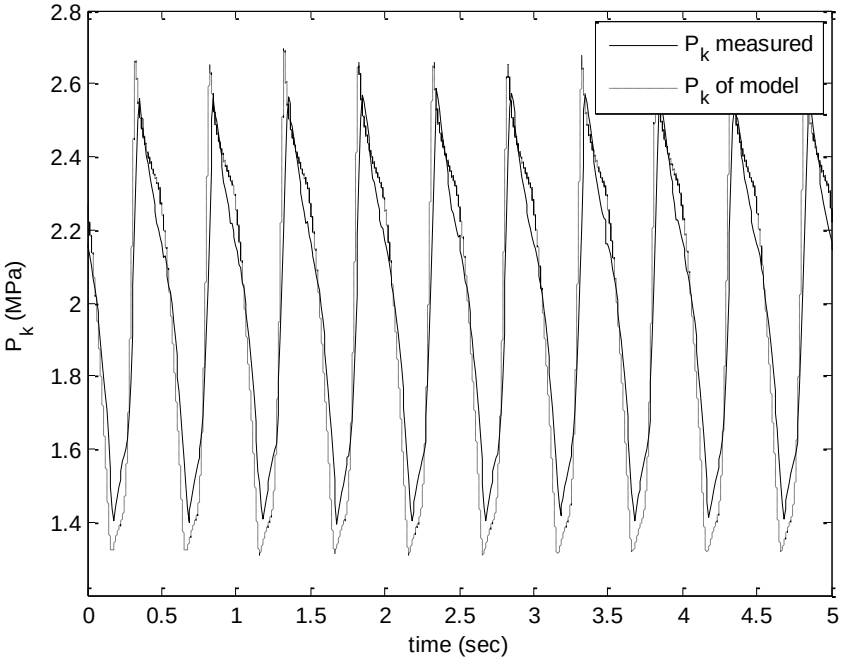

Figure 3-11: Measured and modeled pressure P_k inside the engine section at 450°C heater head temperature, high pressure (20 bar), and at a frequency of 2 Hz. The modeled pressure ratio is 8% higher than measured pressure ratio.

Conclusion

The design, first-principles dynamic model and the experimental setup of a Stirling pressurizer has been described. The dynamic model has been validated with experimental data.

The model matches experimental data for different displacer motion profiles and frequencies, different average engine pressures, and different heater head temperatures. Experimental and modeled pressure ratios do not differ by more than 10% (in most cases less than 5%). Furthermore, since the dynamic model incorporates an arbitrarily specifiable displacer motion, it could be used to optimize such motion with respect to the pressurizer's power, efficiency, or other performance metrics. Additionally, the lumped parameter model could be used in deriving control strategies.

The dynamic model validation presented here does not show the effects of a power piston extracting energy from the system because the experimental setup has no power-piston attached at the power connection ports (shown in Fig. 3-1). However, these effects are included in the model as volumes, and rates of change of volumes, in both the return chamber and the cold-side chamber (V_r, $\dot{V}_r$, V_k, $\dot{V}_k$) that would be influenced by a power piston driven by the pressure difference between the return chamber and the dynamic engine pressure. It can be stated with high confidence that such terms in the model would model the effects well given that such terms are already present for control volume changes in the hot and cold sides due to the displacer motion (V_h, $\dot{V}_h$, V_k, $\dot{V}_k$).

Finally, it should be emphasized that the model required no tuning of parameters with the exception of the regenerator effectiveness which was set according to the range in [9]. In conclusion, the model presented could be used to inform the design and control of not only this engine arrangement, but for others more generically since the dynamic model is built from first-principles with known or measureable parameters.

Acknowledgment

This work was supported by the Center for Compact and Efficient Fluid Power, an NSF Engineering Research Center, grant EEC-0540834.

References

[1] G. Walker, Stirling Engines, Oxford University Press, 1980.

[2] G. Walker and J. R. Senft, Lecture Notes in Engineering: Free Piston Stirling Engines, Springer-Verlag, New York, 1985.

[3] E. H. Cooke-Yarborough, E. Franklin, T. Gesow, R. Howlett, C. D. West, "Thermomechanical generator: an efficient means of converting heat to electricity at low power levels," Proceedings IEE, no. 121, p. 749-751, 1974.

[4] C. D. West, Principles and Applications of Stirling Engines, Van Nostrand Reinhold Company, New York, 1986.

[5] C. D. West, Liquid Piston Stirling Engines, Van Nostrand Reinhold Company, New York, 1983.

[6] F. T. Reader and M. A. Clarke, “Liquid Piston Stirling Air Engines,” 2nd International Conference of on Stirling Engines, 14 p, 1984

[7] Gopal, V. K., Duke, R., and Clucas, D., 2009. “Active Stirling Engine”. In TENCON 2009-2009 IEEE Region 10 Conference, IEEE, pp. 1–6.

[8] M. Craun, B. Bamieh, “Optimal Periodic Control of an Ideal Stirling Engine Model,” ASME Journal of Dynamic Systems, Measurement and Control, Jan 2nd 2015. doi:10.1115/1.4029682

[9] Chin-Hsiang Cheng, and Ying-Ju Yu, “Numerical model for predicting thermodynamic cycle and thermal efficiency of a beta-type Stirling engine with rhombic-drive mechanism”, Renewable Energy, vol. 35, pp. 2590-2601, 2010. doi:10.1016/j.renene.2010.04.002

[10] F. Formosa and G. DEspesse, “Analytical model for Stirling cycle machine design”, Energy Conversion and Management, vol. 51, pp. 1855-1863, 2010. doi:10.1016/j.enconman.2010.02.010

[11] H. Karabulut, “Dynamic analysis of a free piston Stirling engine working with closed and open thermodynamic cycles”, Renewable Energy, vol. 36, pp. 1704-1709, 2011. doi:10.1016/j.renene.2010.12.006

[12] Van de Ven, J., Gaffuri, P., Mies, B., and Cole, G., 2008, "Developments Towards a Liquid Piston Stirling Engine," International Energy Conversion Engineering Conference, Cleveland, Ohio

CHAPTER IV.
FUTURE DIRECTIONS AND DISCUSSION

The contribution of this work, as presented in Chapter II and Chapter III, is a first principles model of the Stirling pressurizer that is validated with experimental data for two different displacer motion profiles, a variety of heater head temperatures and a variety of different average engine pressures. Results show that the first-principles model can be used to optimize efficiency and/ or power output of the Stirling device, can also be used to inform the design of control strategies and the design of the Stirling pressurizer.

The first-principles model can also be used for the design and sizing of an attached power unit. A power unit that can be driven by the pressure swing of the Stirling pressurizer would be a hydraulic pump, a compressor, or an electric generator, making the Stirling pressurizer an ideal power source for a variety of applications.

Oak Ridge National Laboratory for example is interested in building a Stirling device using their Manufacturing Demonstration Facility (MDF) to enable additive manufactured metal components. Additive manufacturing enables unprecedented leap-ahead capabilities in Stirling engines due to the ability to integrate geometries not previously possible with traditional machining. Increasing the surface area for heat transfer along with a controlled displacer could possibly achieve near-ideal Stirling cycle efficiencies. Figure 4-1 illustrates how additive manufacturing allows integrating complex geometries to increase the surface area for heat transfer. A collaboration with Oak Ridge National Laboratory would seek to build a Stirling device to drive an electric generator which in turn could either power a car or deliver electricity to the grid when the car is parked.

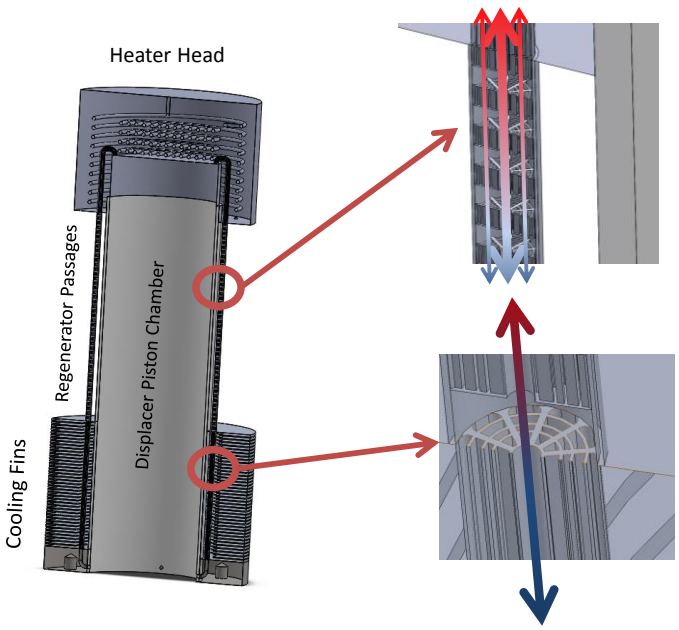

Figure 4- 1: Stirling device using additive manufacturing capabilities

The Stirling pressurizer can also be driven by any excess heat. For example, one by-product of compressing gasses from very low pressures to very high pressures is an elevated gas temperature at the exit of the compressor. Parker Hannifin is interested in running a Stirling pressurizer as a “turbocharger” from the elevated gas temperature exiting a natural gas compressor. This elevated gas temperature would represent the heat source for the Stirling pressurizer. In return, the Stirling pressurizer could boost the pressure of the natural gas before entering the compressor. As a result, the efficiency of the compressor would be increased greatly.

APPENDIX

A. SIMULINK DIAGRAMS

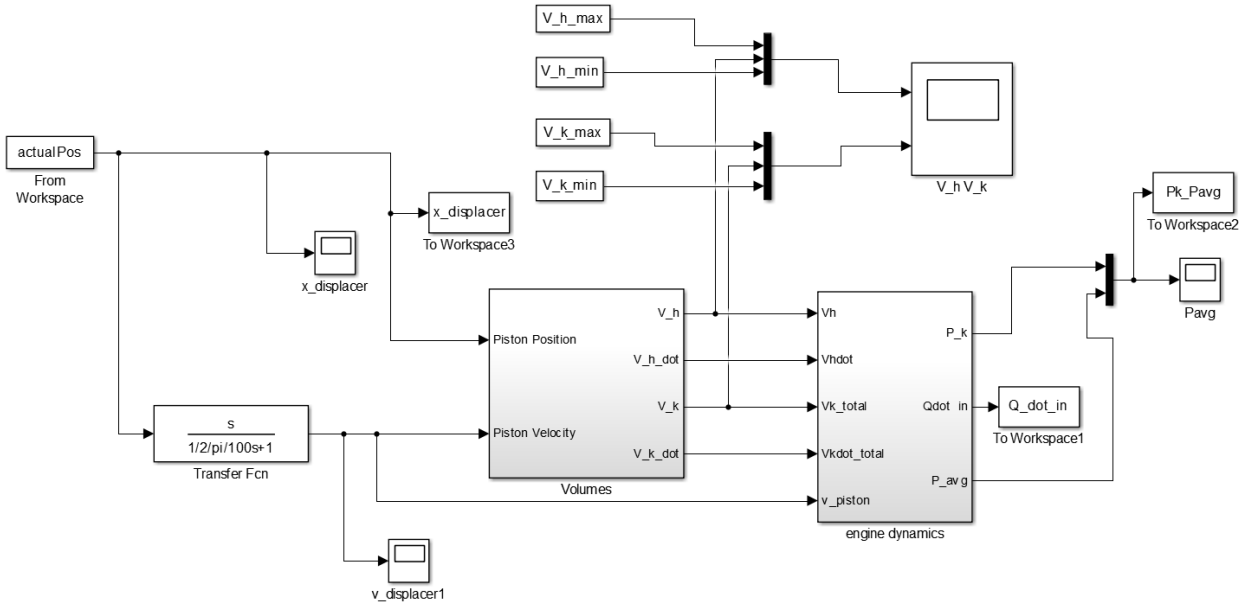

Figure A-1: Overall system

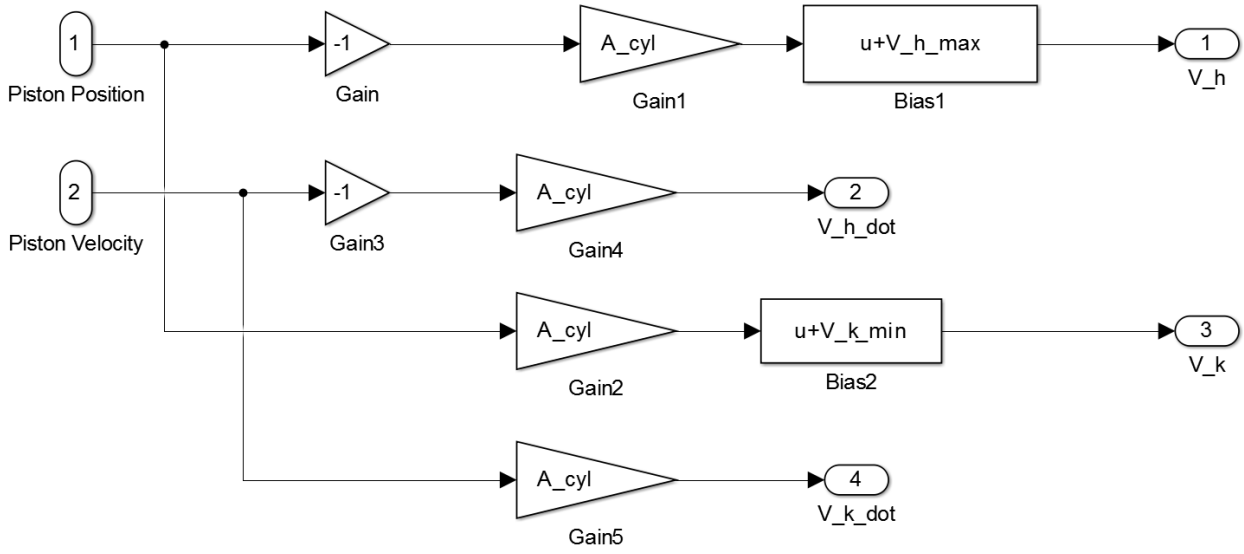

Figure A-2: Volumes

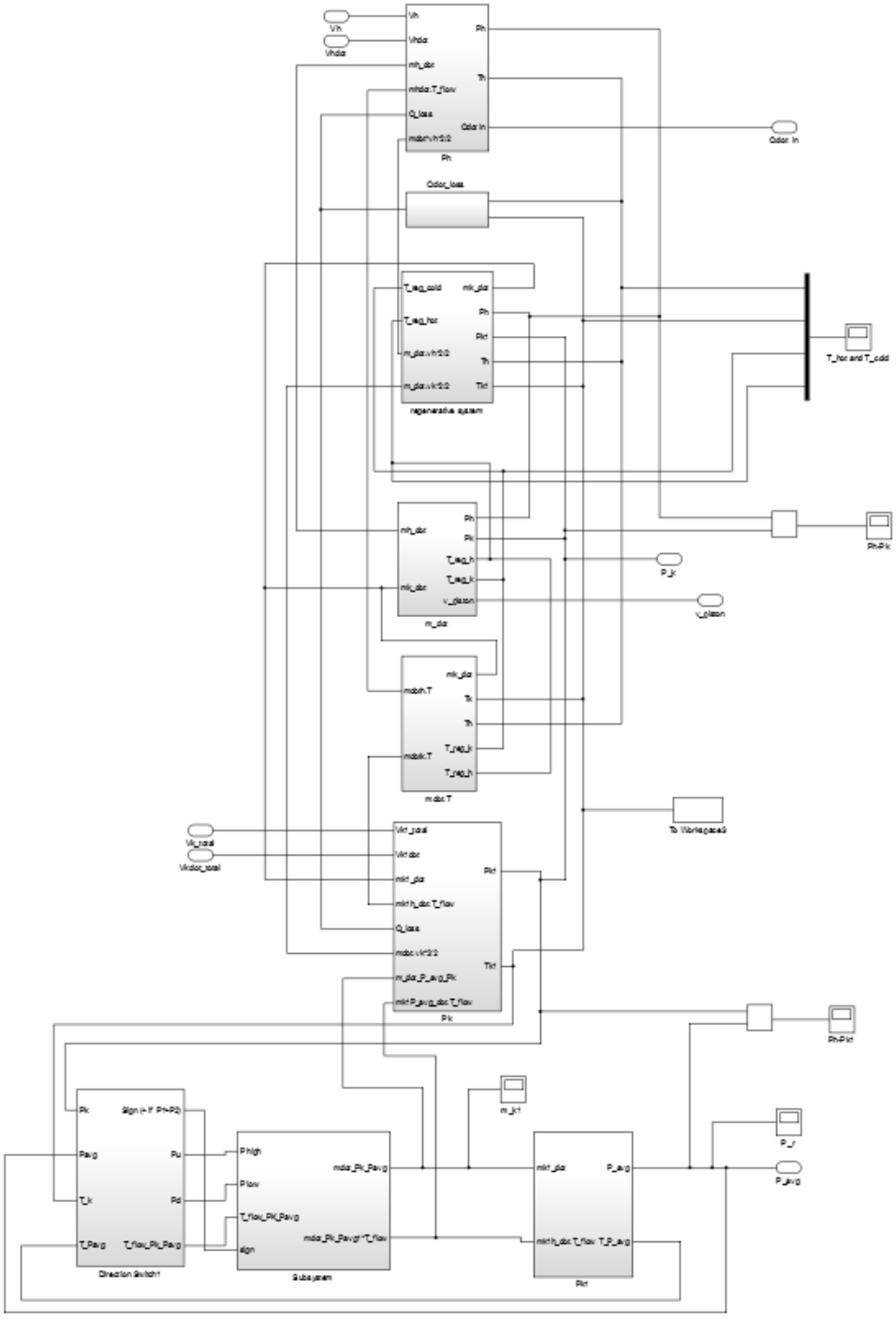

Figure A-3: Engine dynamics

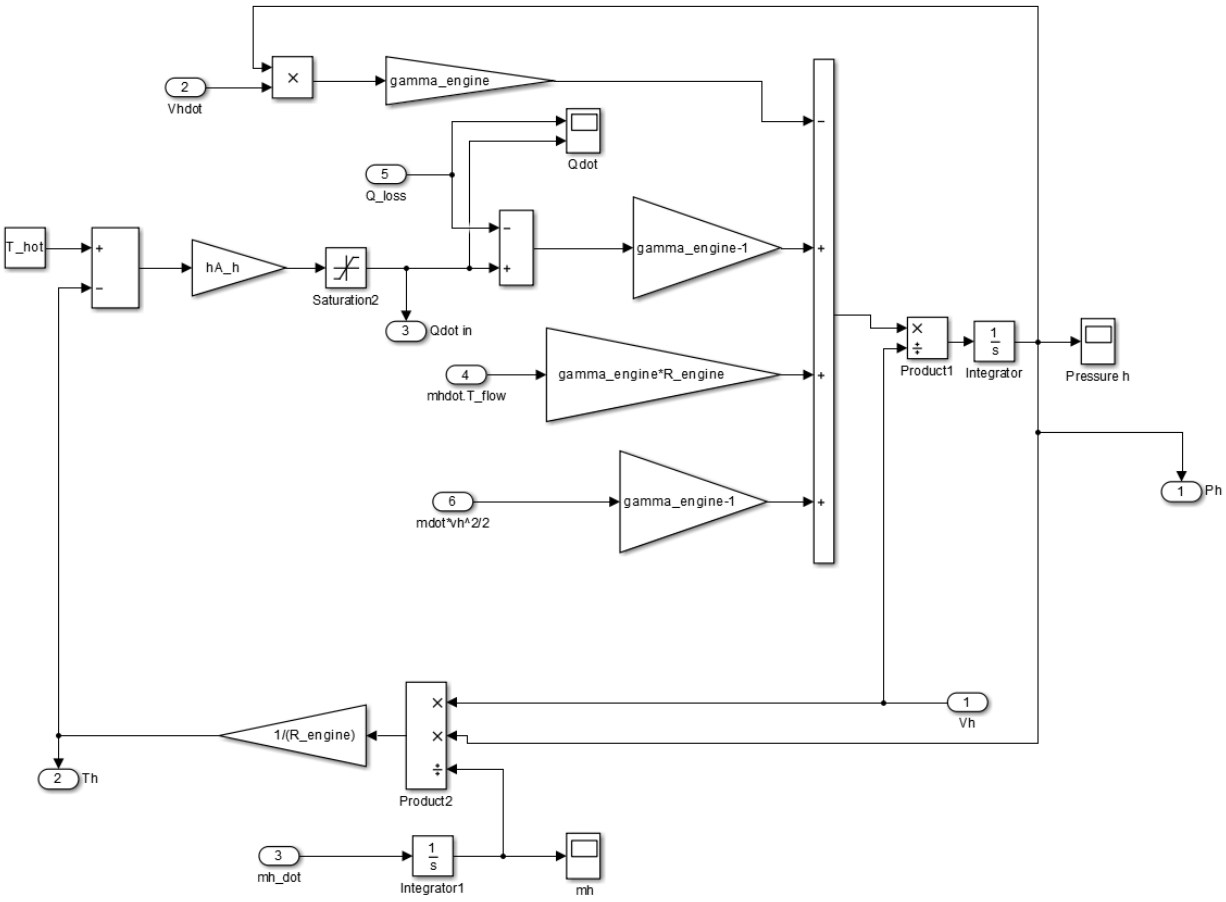

Figure A-4: Pressure dynamics on hot side

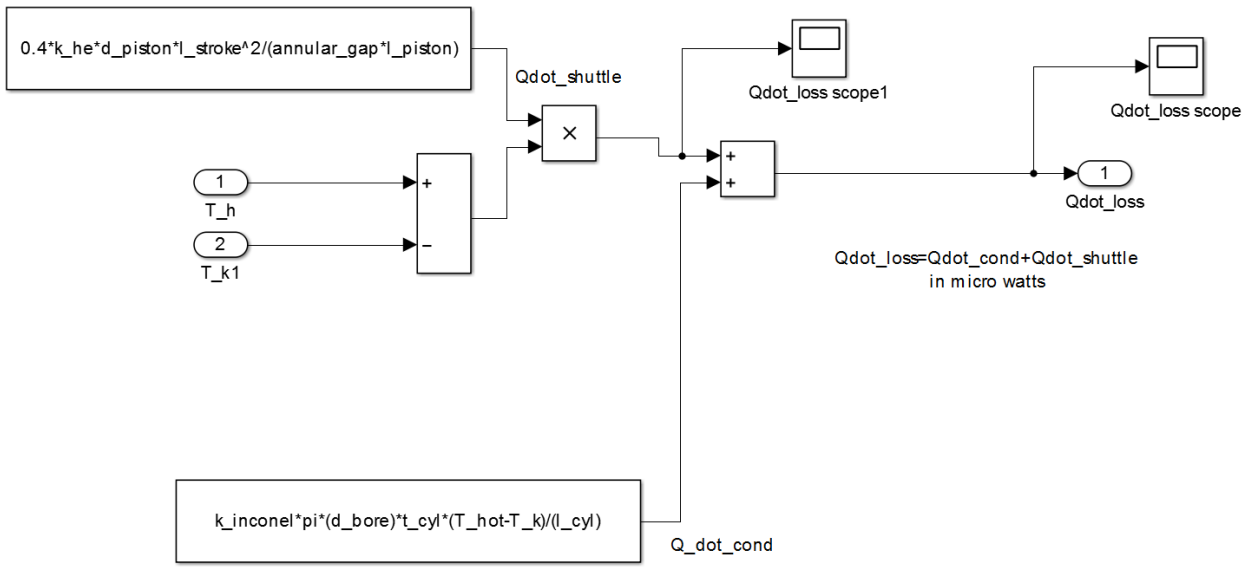

Figure A-5: Heat transfer losses

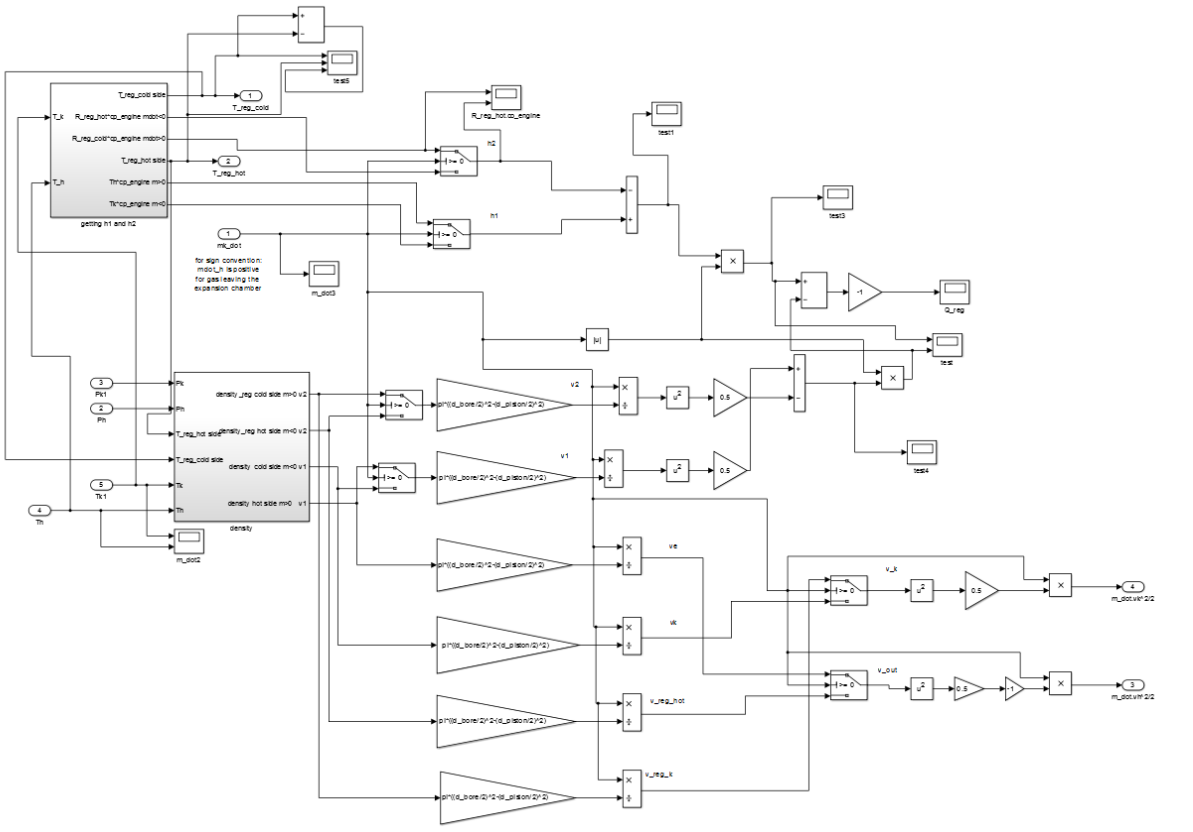

Figure A-6: Regenerative system

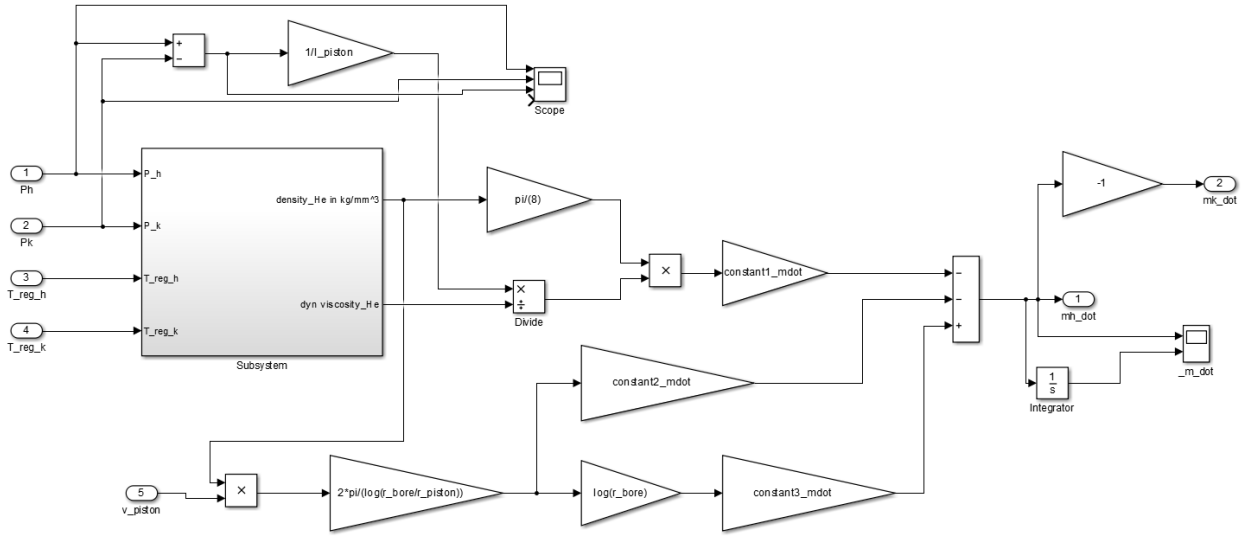

Figure A-7: Mass flow ate in engine section

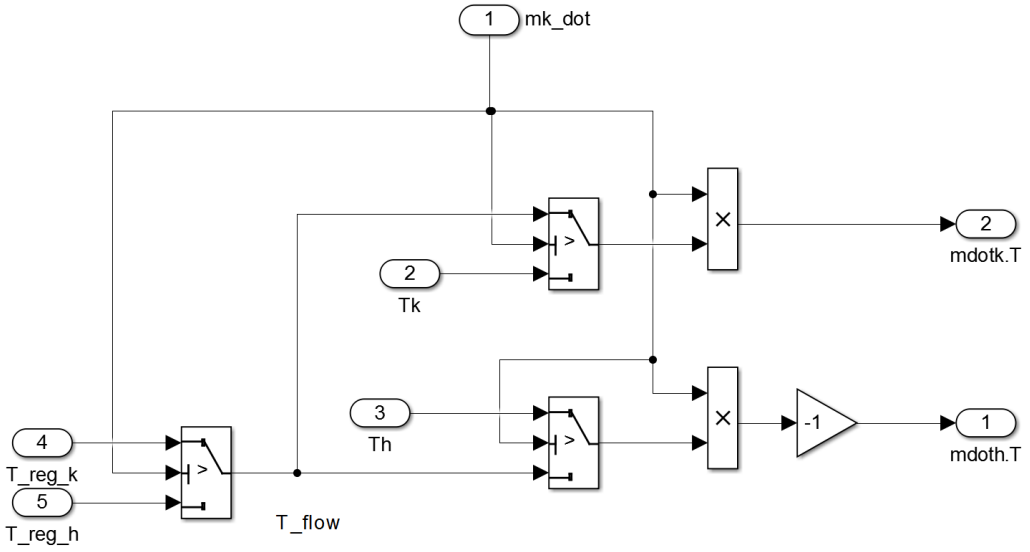

Figure A-8: Mass flow rate in engine section times T_{flow}

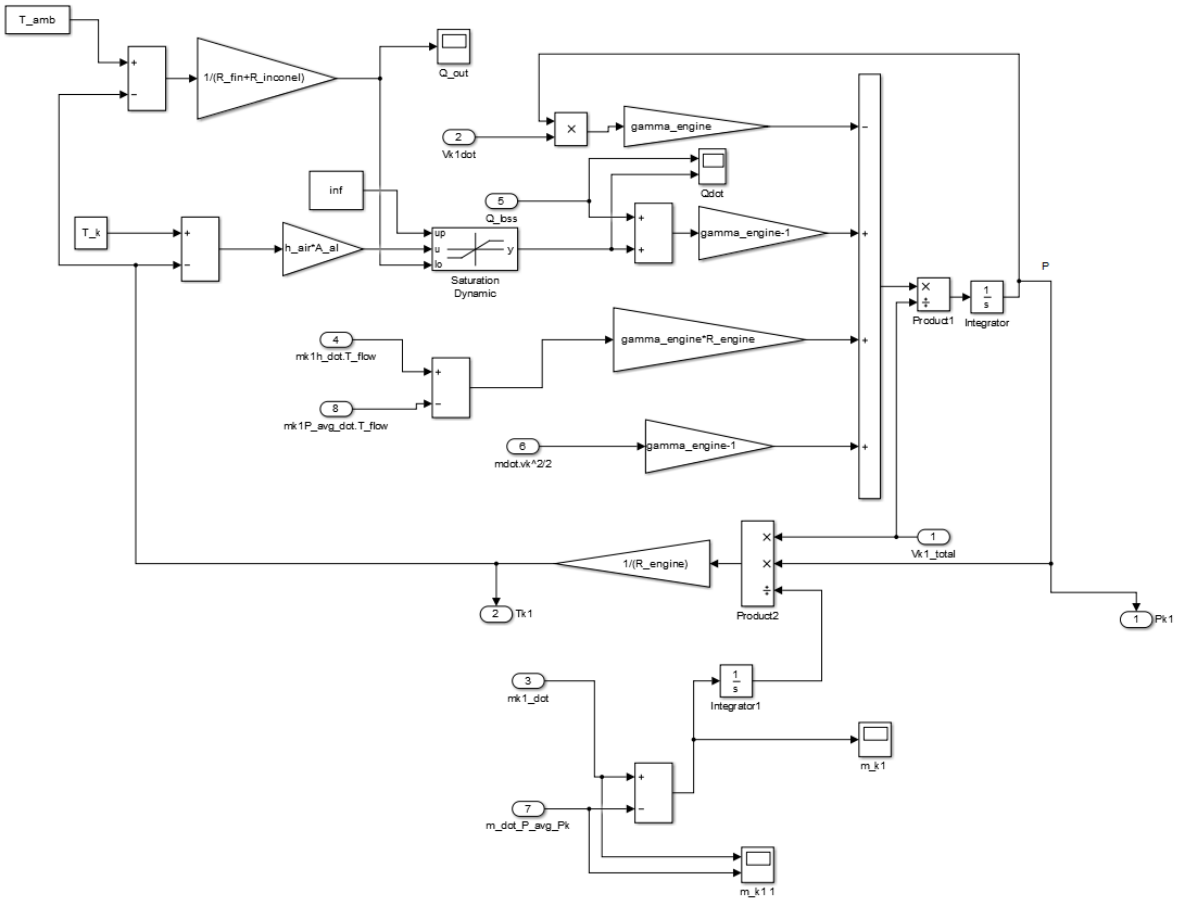

Figure A-9: Pressure dynamics on cold side

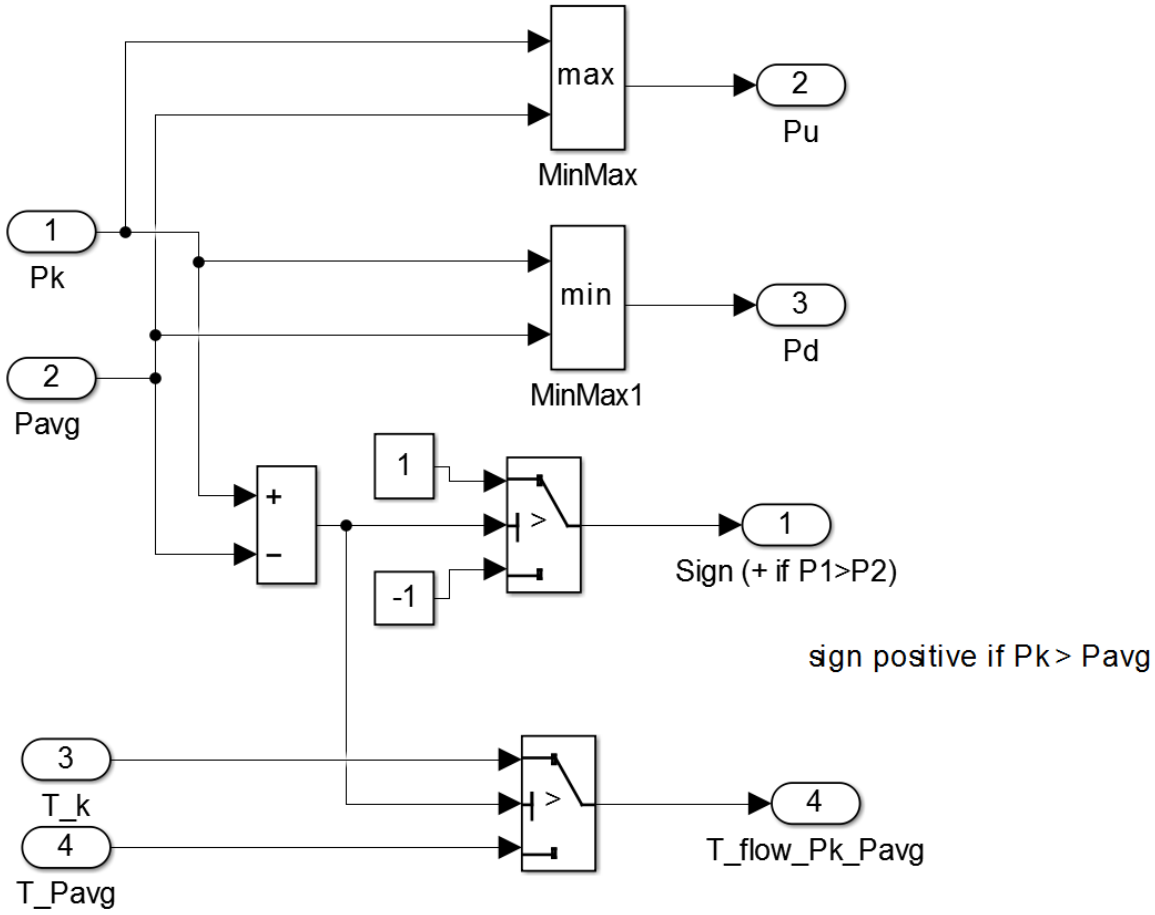

Figure A-10: Direction switch

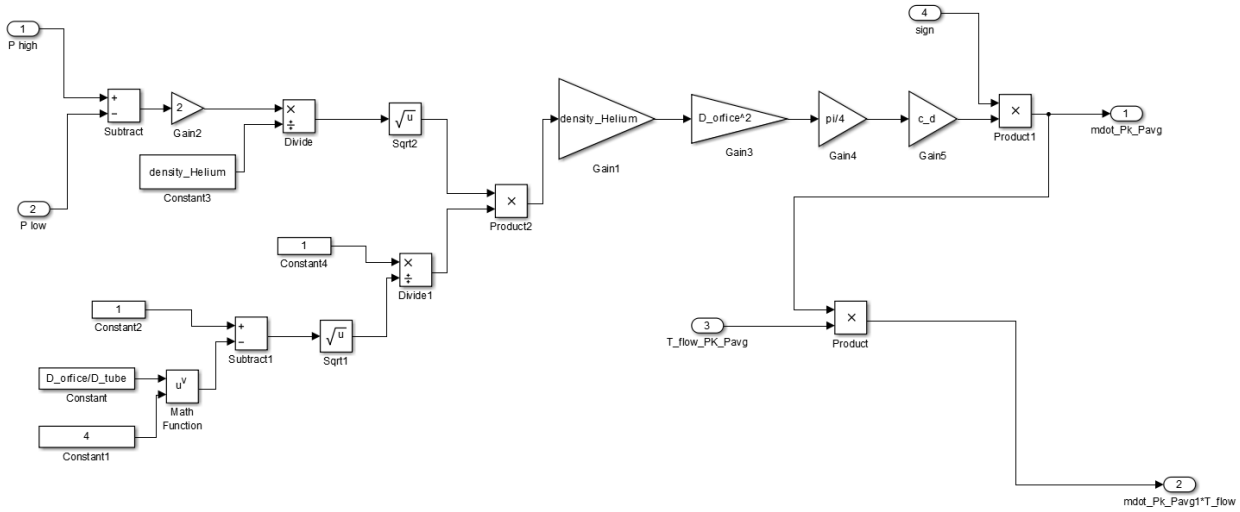

Figure A-11: Mass flow rate between cold side and return chamber

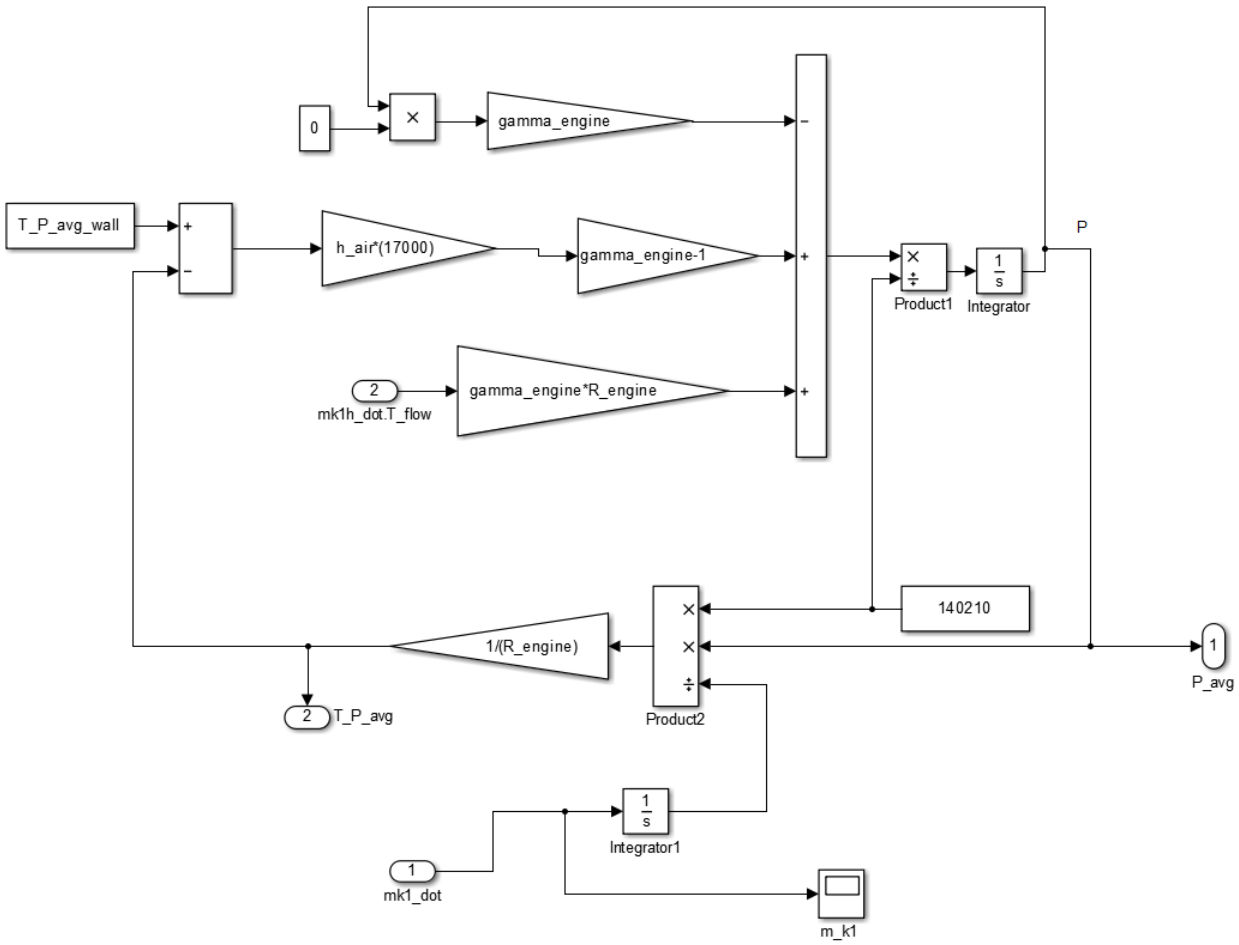

Figure A-12: Mass flow rate between cold side and return chamber

B. MATLAB CODE

```
% Stirling Pressurizer

% Base Units:
%mm, kg, s, mN, kPa, microJ (uJ), microW (uW), K


%%
% Atmospheric Temperature and Pressure

T_amb=25+273;       % Ambient air temperature (K)
P_atm=14.65*6.89;   % Atmoshperic Pressure (kPa)

%%  variables

l_stroke=23.6;      %(mm) stroke length

%% working gas constants (helium) in engine section

% data:
% cv_helium=12.5 % J/mol/K
% cp_helium=20.8 % J/mol/K
% molecular weight = 4.002602 g/mol
% cp_gas=5193.2*1e6; %constant pressure specific heat (in uJ/kg/K)
% cv_gas=3123*1e6; %constant volume specific heat (in uJ/kg/K)
% R_univ=8.3145*1e6; %Average gas constant (in uJ/mol/K)

cp_helium=20.8/4.002602*1000*1e6; %constant pressure specific heat (in
uJ/kg/K)
cv_helium=12.5/4.002602*1000*1e6; %constant volume specific heat (in uJ/kg/K)
R_helium=cp_helium-cv_helium; %gas constant (in uJ/kg/K)
gamma_helium=cp_helium/cv_helium; %ratio of specific heats (no dim)

%% working gas constants (krypton)
% data:
% cp=0.248 J/g/K
% cv=12.5 J/mol/K
% molecular weight = 83.798 g/mol
% cv=0.1492 J/g/K
R_univ=8.3145*1e6;                  %Average gas constant (in uJ/mol/K)
cp_krypton=248*1e6;                 %constant pressure specific heat (in
uJ/kg/K)
cv_krypton=149.2*1e6;               %constant volume specific heat (in
uJ/kg/K)
R_krypton=cp_krypton-cv_krypton;    %gas constant (in uJ/kg/K)
gamma_krypton=cp_krypton/cv_krypton; %ratio of specific heats (no dim)


%%

cp_engine=cp_helium;  % constant pressure specific heat (in uJ/kg/K)
cv_engine=cv_helium; % constant volume specific heat (in uJ/kg/K)
```

```
R_engine=R_helium; %gas constant (in uJ/kg/K)
gamma_engine=gamma_helium; %ratio of specific heats (no dim)


%% Engine Constants

d_rod_LM= 6.31;                              % diameter of rod (LM) in mm
m_rod=0.0430;                                % mass of rod in kg
m_displacer=0.06;                            % mass of displacer in kg
m_rod_displacer=m_rod+m_displacer; % mass of rod and displacer in kg

t_cyl=1.2446;                  % thickness of Inconel cylinder (mm)
d_bore=50.8-2*t_cyl; %(mm)
d_piston=d_bore-0.8; %(mm)

l_stroke=l_stroke; %(mm)
l_bottom_stroke=0.5;% % remaining cylinder at cold side (mm)
l_top_stroke=0.5; % remaining cylinder at hot side (mm)
l_piston=2.97*d_bore; % mm
l_cyl=l_piston+l_stroke+l_bottom_stroke+l_top_stroke; %Length of quartz
cylinder with gasket (mm)
l_return=100; % (mm) length of return chamber

%%  Area Calculations

A_cyl=pi*(d_bore/2)^2;
A_piston=pi*(d_piston/2)^2;
A_rod=pi*(d_rod_LM/2)^2;

 %% calculates the surface area for heat transfer on heater head

N_h=7;                           % number of inside fins on heater head
H_fin_h=16.5;                    % height of fins on hot side (mm)
r_h_1=d_bore/2;                  % inside radius of inside fins on heater head
(mm)
r_h_2=r_h_1+3;                   % outside radius of inside fins on heater head
(mm)
t_h=1.5;                         % thickness of each fin on inside fins of
heater head (mm)
h_h_below=8.5;                   % hight below last fin to end of heater head
(mm)
A_h=pi*(d_bore/2)^2+pi*d_bore*h_h_below+(2*pi*r_h_1)*(H_fin_h-
N_h*t_h)+(2*pi*r_h_2)*N_h*t_h...
    +2*N_h*pi*(r_h_2^2-r_h_1^2);                      % Area available for
heat transfer on cold side  (mm^2)
V_dead_fin_h=N_h*pi*(r_h_2^2-r_h_1^2)*t_h;            % dead volume caused
by inside fins on heater head

%% calculates the surface area for heat transfer on outside fins for cooler
head

N_k_out=22;                            % number of inside fins on cooler head
H_fin_k=l_cyl/2;                       % height of fins on cold side (mm)
r_k_out_0=d_bore/2+t_cyl;              % inside diameter of base of fin (mm)
```

```
r_k_out_1=d_bore/2+7;                   % inside radius of inside fins on
cooler head (mm)
r_k_out_2=45;                           % outside radius of inside fins on
cooler head (mm)
t_k_out=2;                              % thickness of each fin on inside fins
of cooler head (mm)
A_al=(2*pi*r_k_out_1)*(H_fin_k-N_k_out*t_k_out)+(pi/4)*(d_bore^2-
d_rod_LM^2)...
           +(2*pi*r_k_out_2)*N_k_out*t_k_out+2*N_k_out*pi*(r_k_out_2^2-
r_k_out_1^2); % Area available for heat transfer on cold side (housing, lead
screw, etc.) (mm^2)

%% fin efficiency

T_amb=T_amb;
T_b=333;       % Temperature on base of fins (between fins and Inconel
cylinder)
k_Al=215000;                            % thermal conductivity of Aluminium
(uW/mm/K)
k_inconel=10.1e3;                       % thermal conductivity of Inconel
(uW/mm/K)
h_air=50;                               % W/m^2/K or uW/mm^2/K
r_k_out_2c=r_k_out_2+(t_k_out/2);       % corrected outside fin radius (mm)
L=r_k_out_2-r_k_out_1;
L_c=L+(t_k_out/2);                      % corrected length
A_f=2*pi*(r_k_out_2c^2-r_k_out_1^2); % from heat transfer book p.171
A_t=N_k_out*A_f+2*pi*r_k_out_1*(H_fin_k-N_k_out*t_k_out);  % from heat
transfer book p.171
A_p=L_c*t_k_out;
(L_c)^1.5*sqrt(h_air/(k_Al*A_p));       % look up efficiency of annular fin of
rectancular profile
n_f=0.95;

run('Z:\Anna\Research\MATLAB\other MATLAB files\calculation_h')

R_He_cyl=(1/(h*2*pi*(d_bore/2)*(H_fin_k)));
R_inconel=(log(r_k_out_0/(d_bore/2))/(2*pi*k_inconel*H_fin_k));
R_fin_base=(log(r_k_out_1/r_k_out_0))/(2*pi*k_Al*H_fin_k);
R_fin=1/(h_air*A_t*(1-((N_k_out*A_f)/A_t)*(1-n_f)));

q_t=(1/(R_He_cyl+R_inconel+R_fin_base+R_fin))*(T_amb-T_b);

%% Heat transfer

hA_h= h*A_h;

%% Calculate Volumes
V_cyl=A_cyl*l_cyl;

V_piston=l_piston*A_piston; % Volume taken up by piston

V_dead_piston=l_piston*(A_cyl-A_piston); %Dead volume surrounding piston
V_h_dead=V_dead_piston/2+l_top_stroke*A_cyl+V_dead_fin_h;
V_h_max=V_h_dead+l_stroke*A_cyl; % Max volume of air on hot side (m^3)
V_h_min=V_h_dead; % Min volume of air on hot side (m^3)
```

```
V_k_dead=l_bottom_stroke*A_cyl+V_dead_piston/2;
V_k_max=V_k_dead+l_stroke*A_cyl; % Max volume of air on cold side (m^3)
V_k_min=V_k_dead; % Min volume of gas on cold side (m^3)

%% initial conditions engine hot side

T_h_0=T_hot;
P_h_0=P_k_min;
V_h_0=V_h_dead;
m_h_0=P_h_0*V_h_0/(R_engine*T_h_0);

%% initial conditions engine cold side
T_k_0=T_k;
P_k_0=P_k_min;
V_k_0=V_k_dead + l_stroke*A_cyl;
m_k_0=P_k_0*V_k_0/(R_engine*T_k_0);

%% regneration effect

k_he=211.4;   % thermal conductivity of helium (uW/mm/K) at 500K
k_ss=17e3;    % thermal conductivity of stainless steel (uW/mm/K)
alpha_ss=4.2; % thermal diffusivity of stainless steel (mm^2/s)
k_inconel=k_inconel;
%thermal conductivity of Inconel (uW/mm/K)
annular_gap=(d_bore/2)-(d_piston/2); % annular gap (mm)
omega=2*pi*f_Hz;
C=(k_ss/k_he)*annular_gap*sqrt(omega/(2*alpha_ss));
BET=(2*C^2-C)/(2*C^2-1);
Q_shuttle=(pi/8)*k_he*l_stroke*(T_hot-
T_k)*(d_bore/annular_gap)*(l_stroke/l_piston)*BET;

%%  constants needed to calculate m_dot

r_bore=d_bore/2;
r_piston=d_piston/2;

constant1_mdot=((r_bore)^4-(r_piston)^4-(((r_bore)^2-
(r_piston)^2)^2/log(r_bore/r_piston)));
constant2_mdot=0.5*(r_bore^2*log(r_bore)-r_piston^2*log(r_piston))-
0.25*(r_bore^2-r_piston^2);
constant3_mdot=0.5*r_bore^2-0.5*r_piston^2;

A_hole_displacer=(pi/4)*0.1^2;
```

Code to calculate the heat transfer coefficient h

```
% calculation of convection coefficient h

A_gap=(pi/4)*(d_bore^2-d_piston^2);
V_cyl=A_cyl*l_cyl;                      % Volume of cylinder
V_piston=A_piston*l_piston;             % Volume of piston

V_dead_piston=l_piston*(A_gap);         %Dead volume surrounding piston
V_h_dead=V_dead_piston/2+l_top_stroke*A_cyl;
V_k_dead=l_bottom_stroke*A_cyl+V_dead_piston/2;
V_dead=V_k_dead+V_h_dead;

V_max=V_cyl-V_piston-V_dead;         % max. Volume thats moved by displacer
per stroke

t=1/(f_Hz*2);                           % time displacer moves V_max (sec)


V_dot=V_max/t;                          % in mm^3/sec
velocity=V_dot/A_gap/1000;              % in m/sec

C=d_bore-d_piston;                       % characteristic length of a duct in mm
charac_length=(C)/1000;                  % characteristic length of a duct in m
R_He=2.077;                              % kJ/kg/K
% T_avg=600;                             % avg. Temperature in K
% P_avg=2000;                            % avg. Pressure in kPa
density_He=P_avg/(R_He*T_avg);           % from ideal gas law in kg/m^3
viscosity_He=19e-6*((273+79.4)/(T_avg+79.4))*(T_avg/273)^1.5;      % in Pa*s
kinem_viscosity_He=viscosity_He/density_He ;                       % in m^2/s


density_air=0.588;                  % from ideal gas law in kg/m^3
viscosity_air=3.017e-5;             % in Pa*s
kinem_viscosity_air=viscosity_air/density_air ;     % in m^2/s
k_air=0.0485;
Re_He=velocity*charac_length/kinem_viscosity_He;
Re_air=velocity*charac_length/kinem_viscosity_air;
a=0.023;
Pr=0.7;
m=0.8;
n=0.3;
k=0.14789*(T_avg/273)^0.6958;

h=a*Re_He^m*Pr^n*k/charac_length
h_air=a*Re_air^m*Pr^n*k_air/charac_length
```

C. TECHNICAL DRAWINGS FOR PROTOTYPE

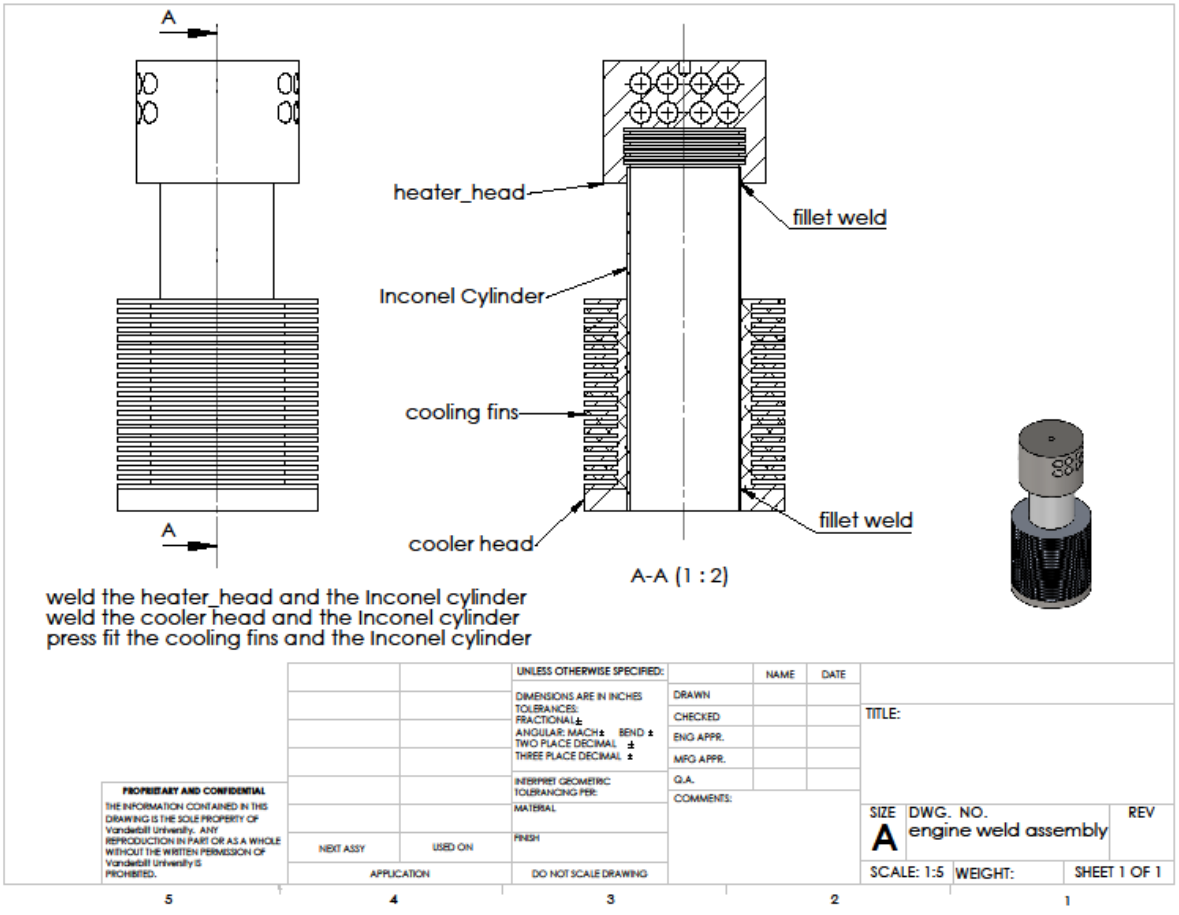

Figure C-1: Engine weld assembly

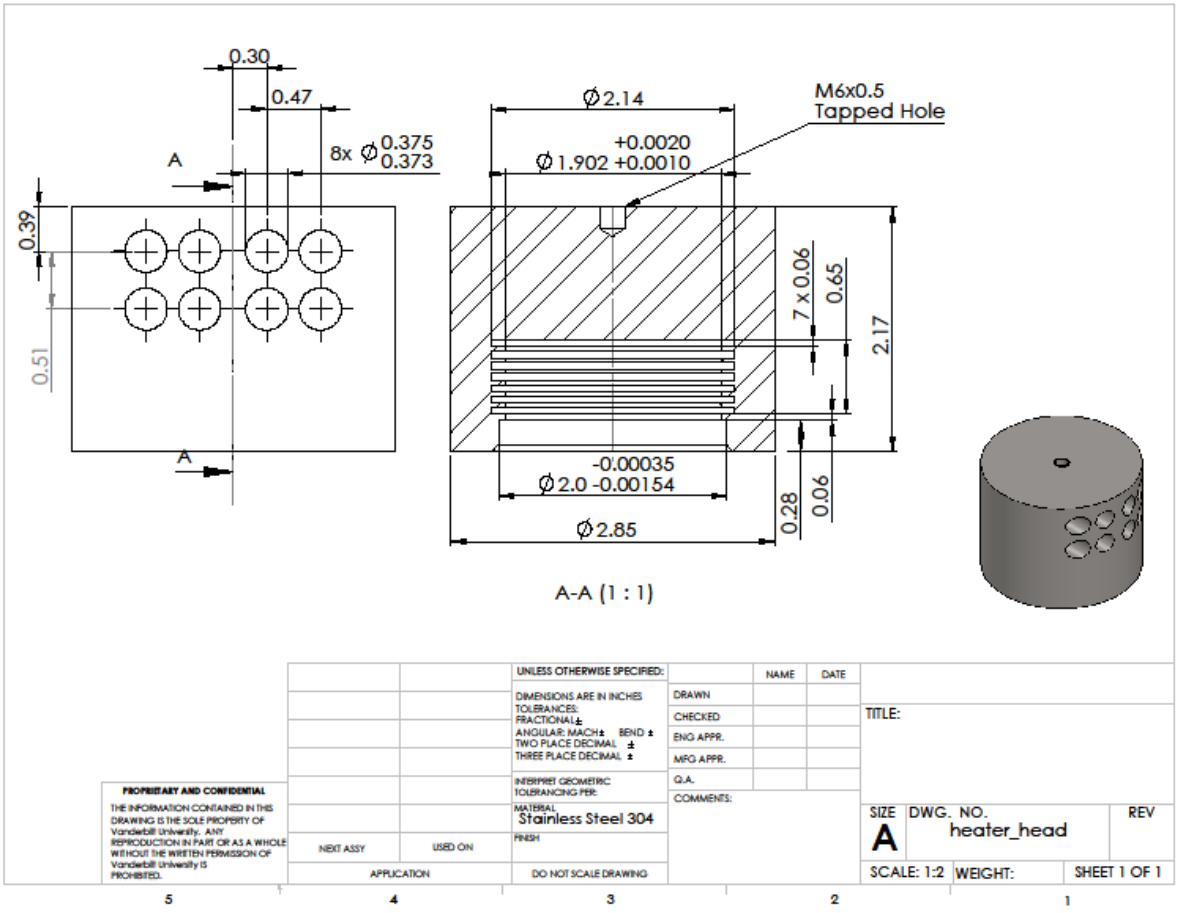

Figure C-2: Heater head

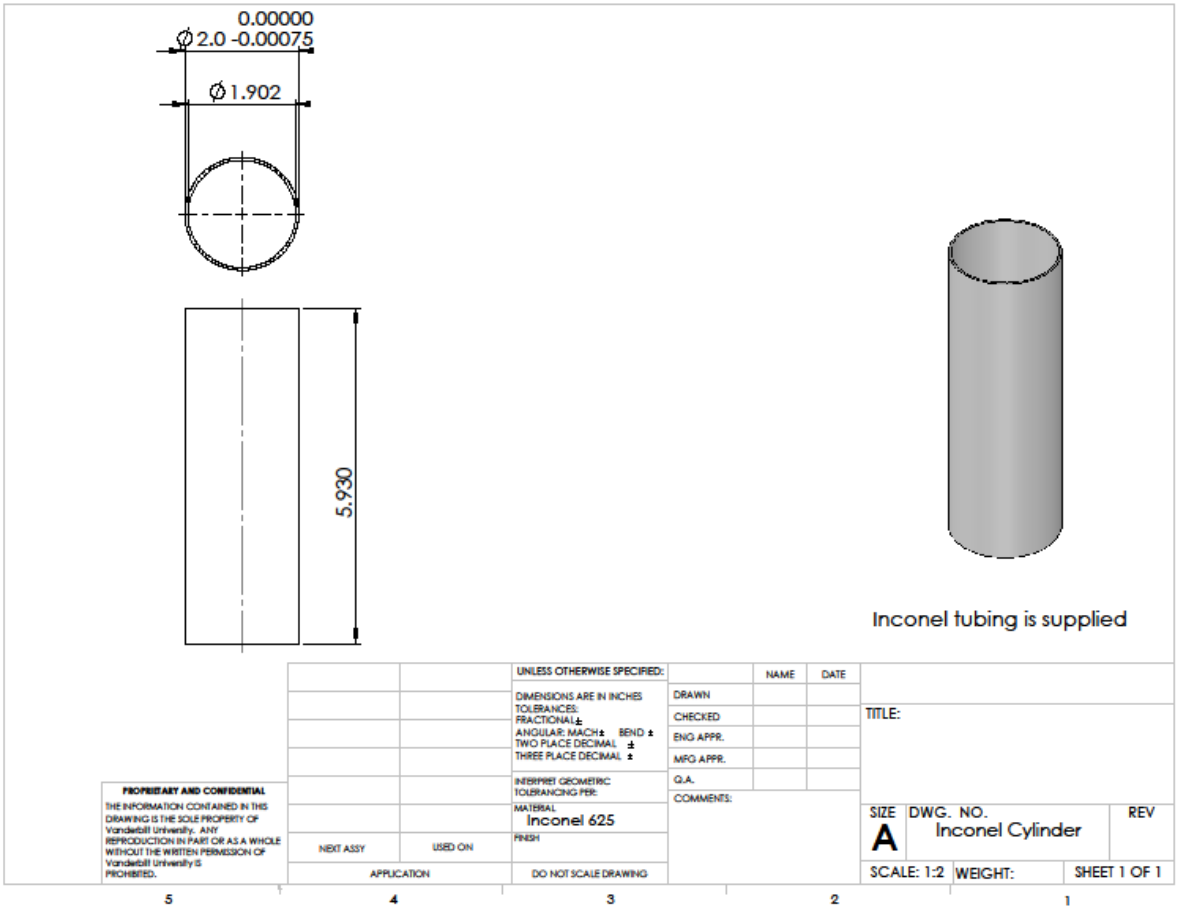

Figure C-3: Inconel cylinder

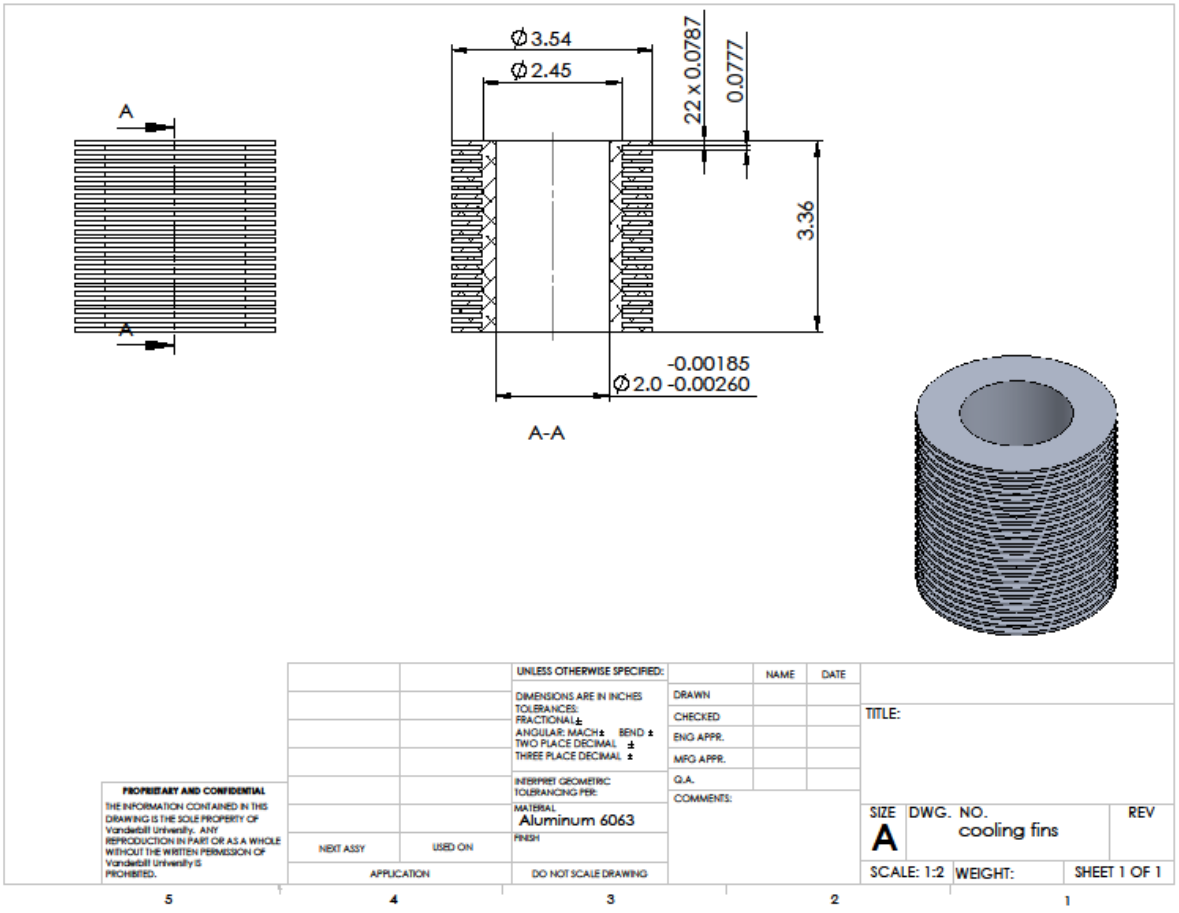

Figure C-4: Cooling fins

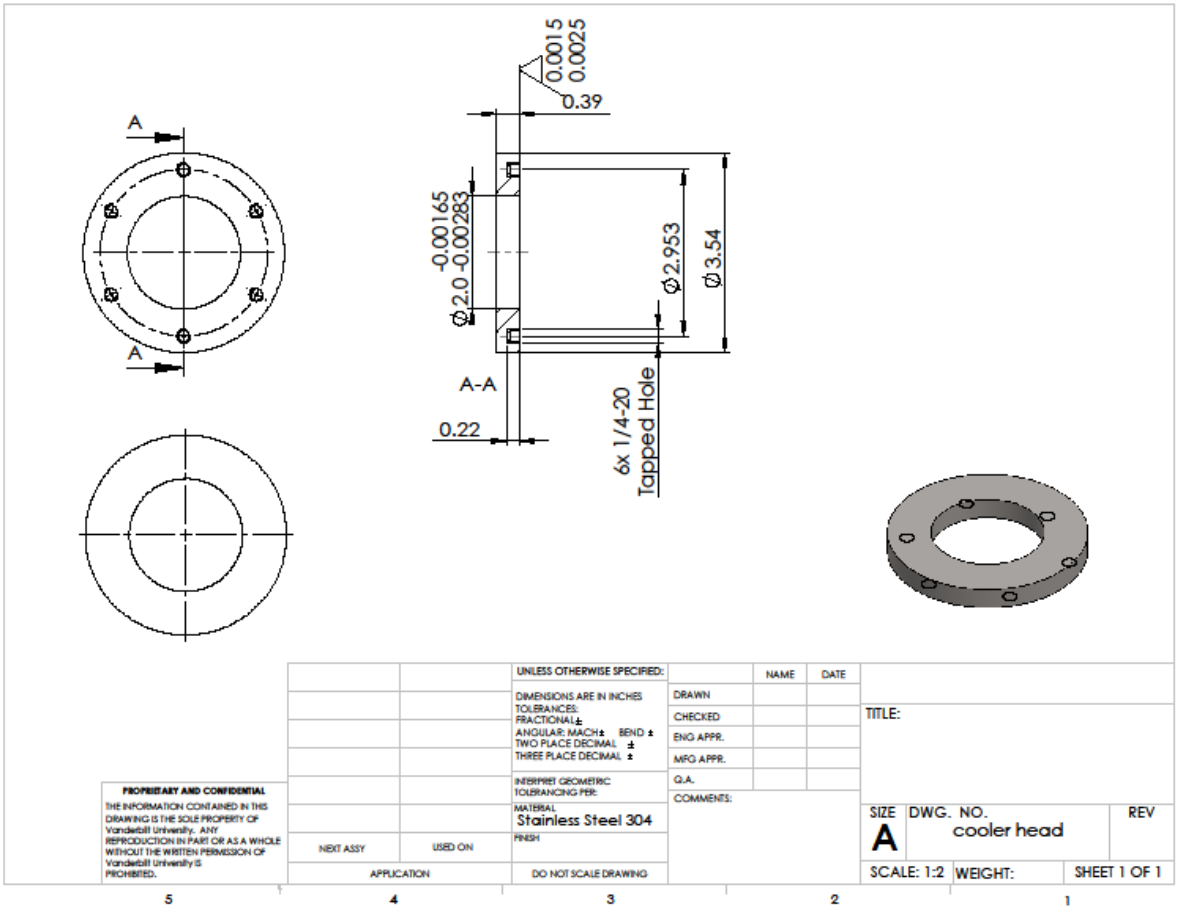

Figure C-5: Cooler head

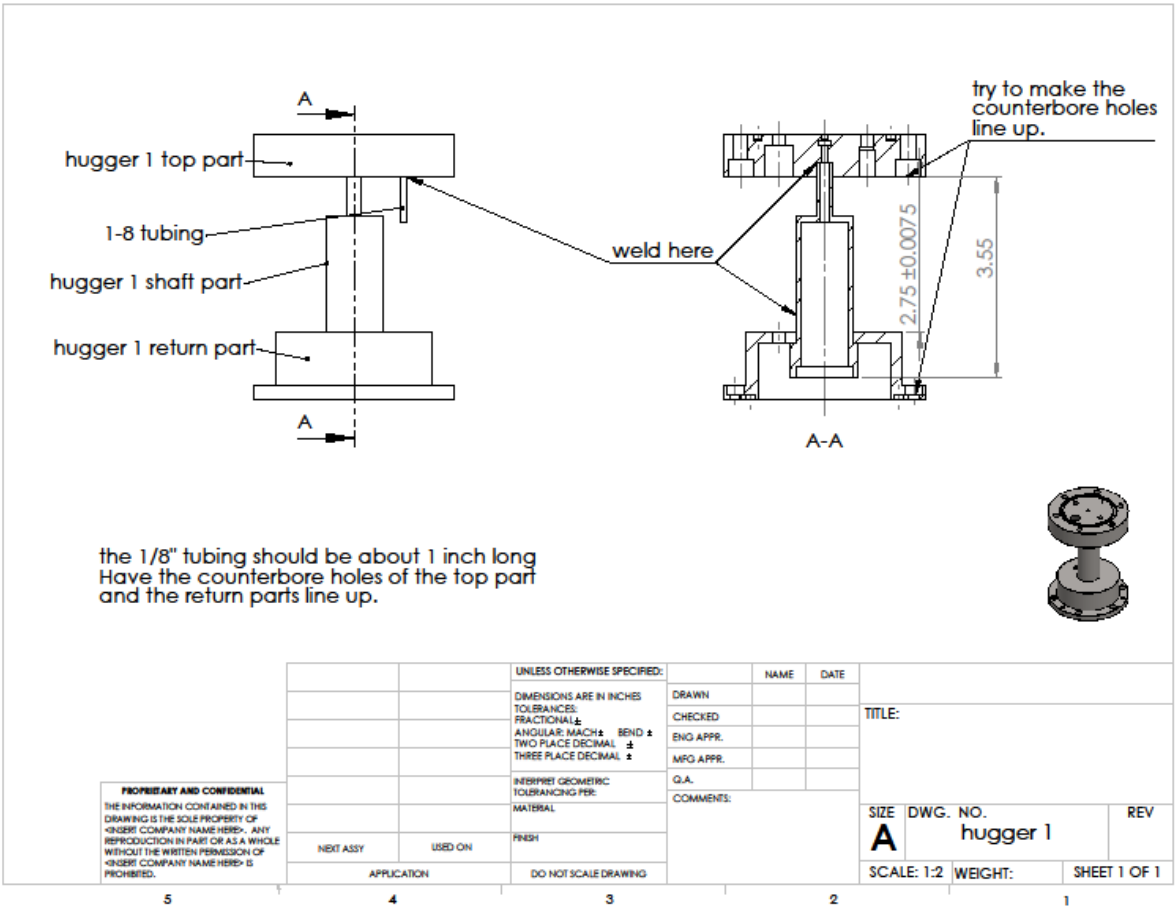

Figure C-6: Hugger1 of return chamber

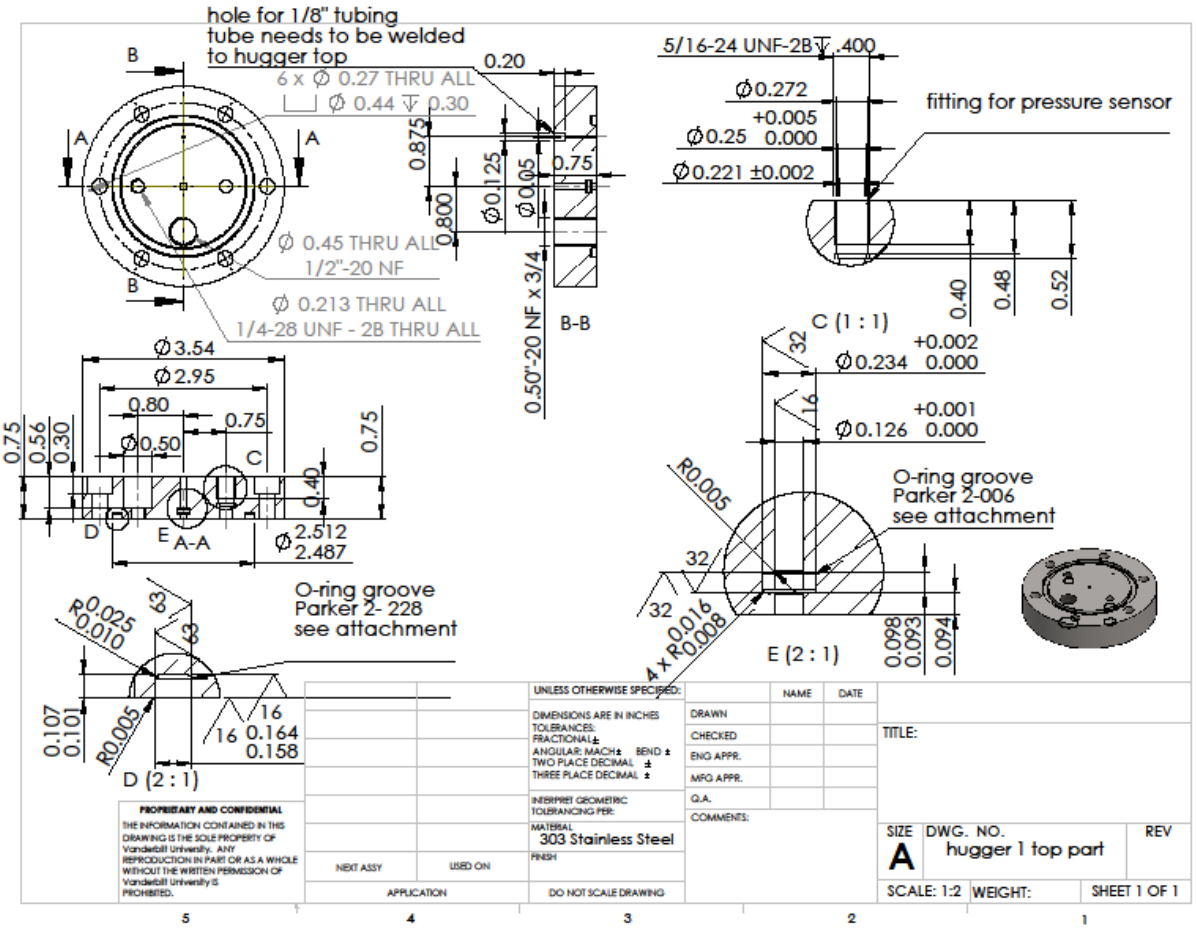

Figure C-7: Top part of hugger1

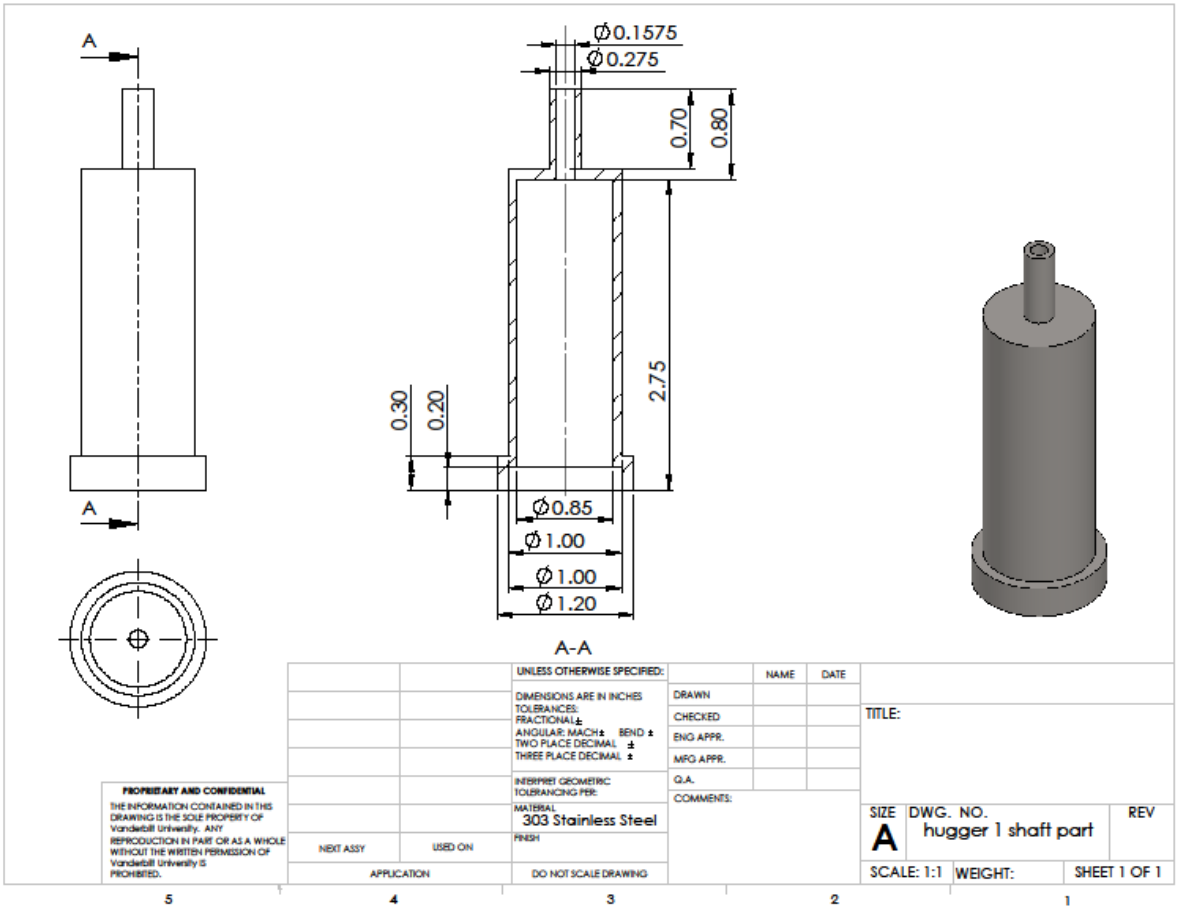

Figure C-8: Shaft part of hugger1

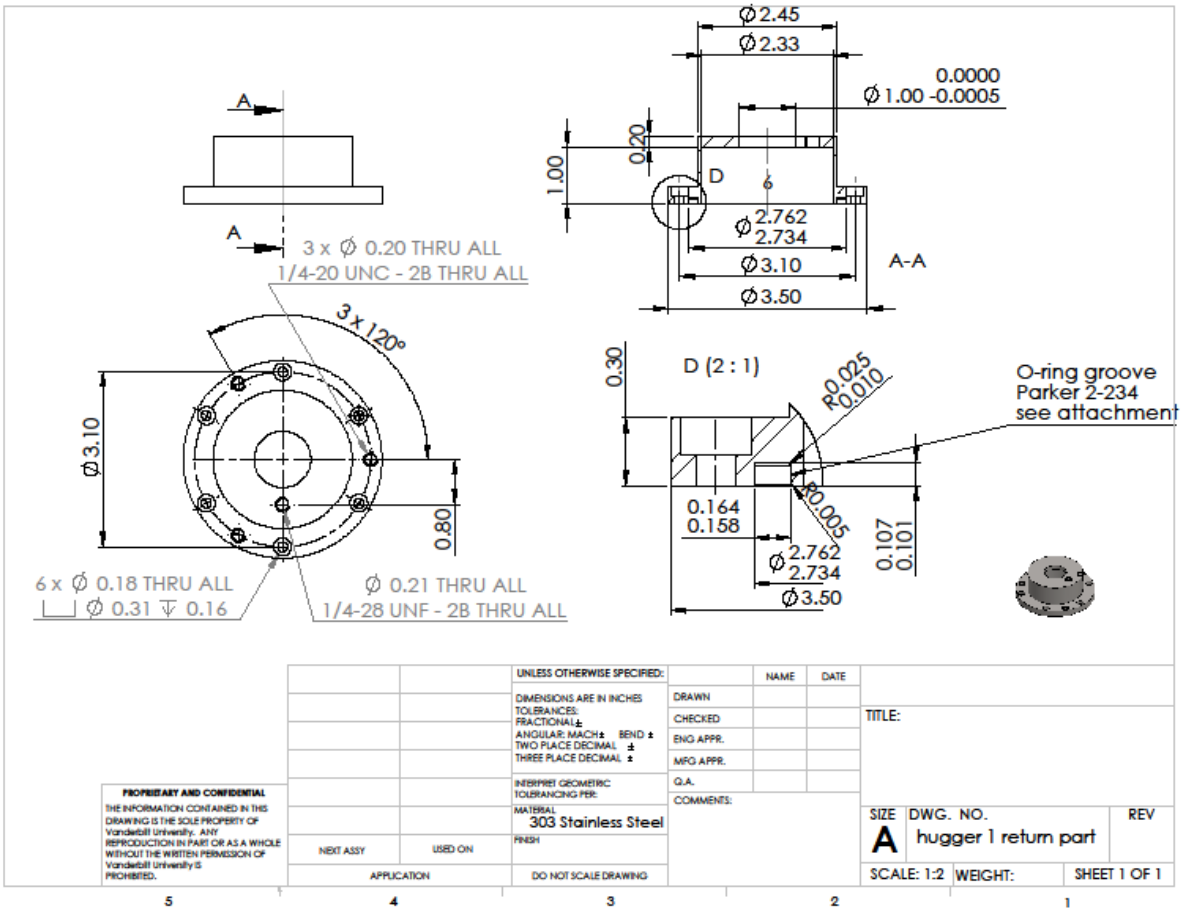

Figure C-9: Return part of hugger1

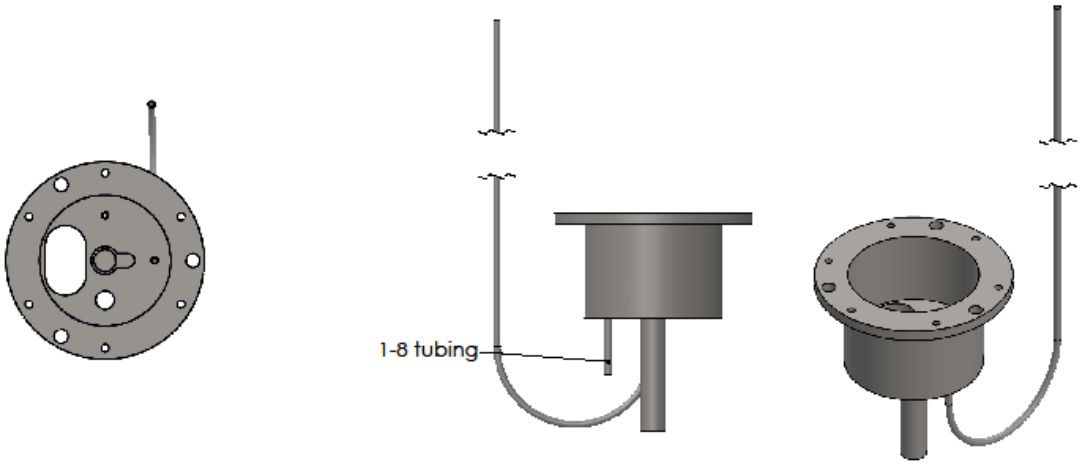

the multipin feedthrough needs to be
welded to the hugger2 top.
mulitpin feedthrough will be supplied.
Also, a 1/8" tubing needs to be welded to the hugger2 top.
The short tubing about 1.5" is connected to a ball valve.
The long tubing about 18 inches is connected to a needle valve

		UNLESS OTHERWISE SPECIFIED:		NAME	DATE
		DIMENSIONS ARE IN INCHES TOLERANCES: FRACTIONAL ± ANGULAR: MACH ± BEND ± TWO PLACE DECIMAL ± THREE PLACE DECIMAL ±	DRAWN		
			CHECKED		
			ENG APPR.		
			MFG APPR.		
		INTERPRET GEOMETRIC TOLERANCING PER:	Q.A.		
		MATERIAL	COMMENTS:		
NEXT ASSY	USED ON	FINISH			
APPLICATION		DO NOT SCALE DRAWING			

PROPRIETARY AND CONFIDENTIAL
THE INFORMATION CONTAINED IN THIS DRAWING IS THE SOLE PROPERTY OF <INSERT COMPANY NAME HERE>. ANY REPRODUCTION IN PART OR AS A WHOLE WITHOUT THE WRITTEN PERMISSION OF <INSERT COMPANY NAME HERE> IS PROHIBITED.

TITLE:

SIZE	DWG. NO.	REV
A	hugger2	
SCALE: 1:2	WEIGHT:	SHEET 1 OF 1

5 4 3 2 1

Figure C-10: Hugger2 of return chamber

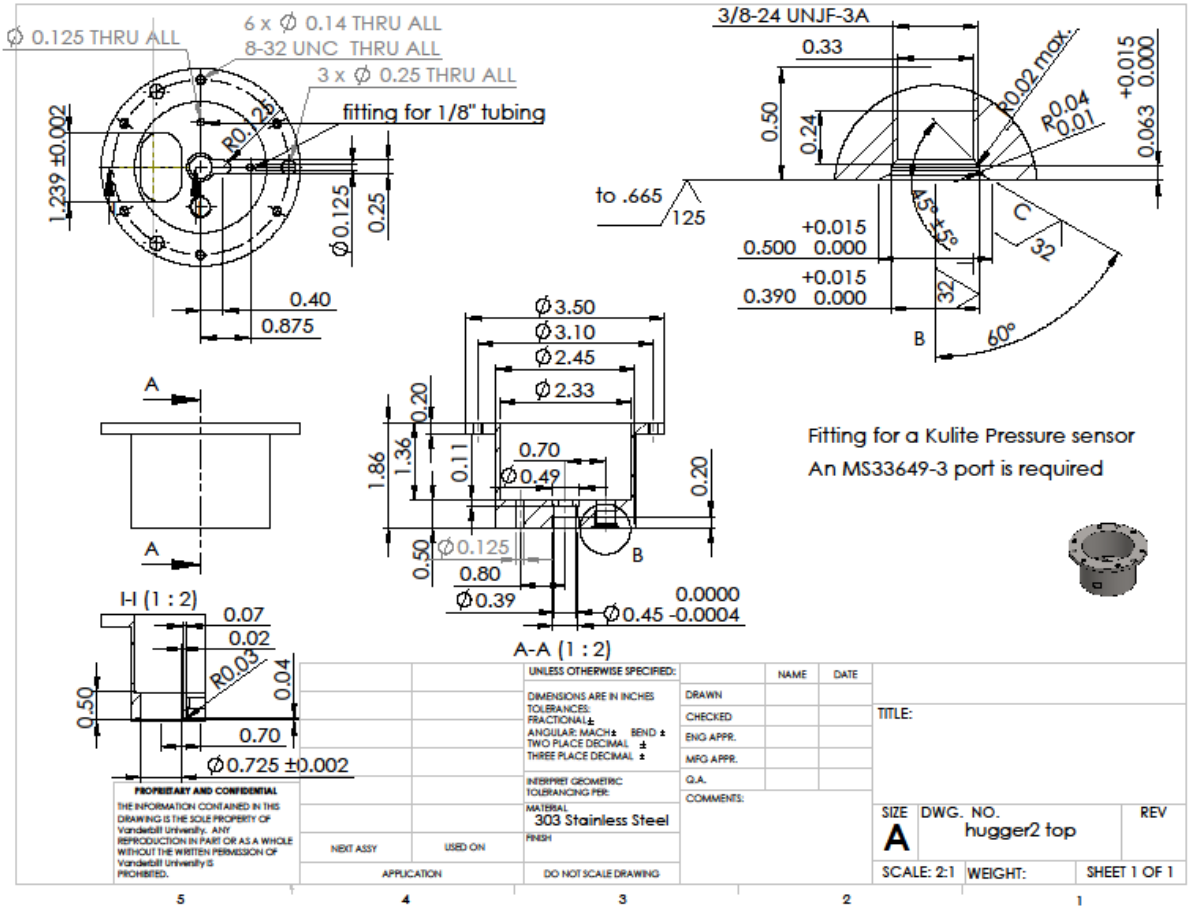

Figure C-11: Top part of hugger2

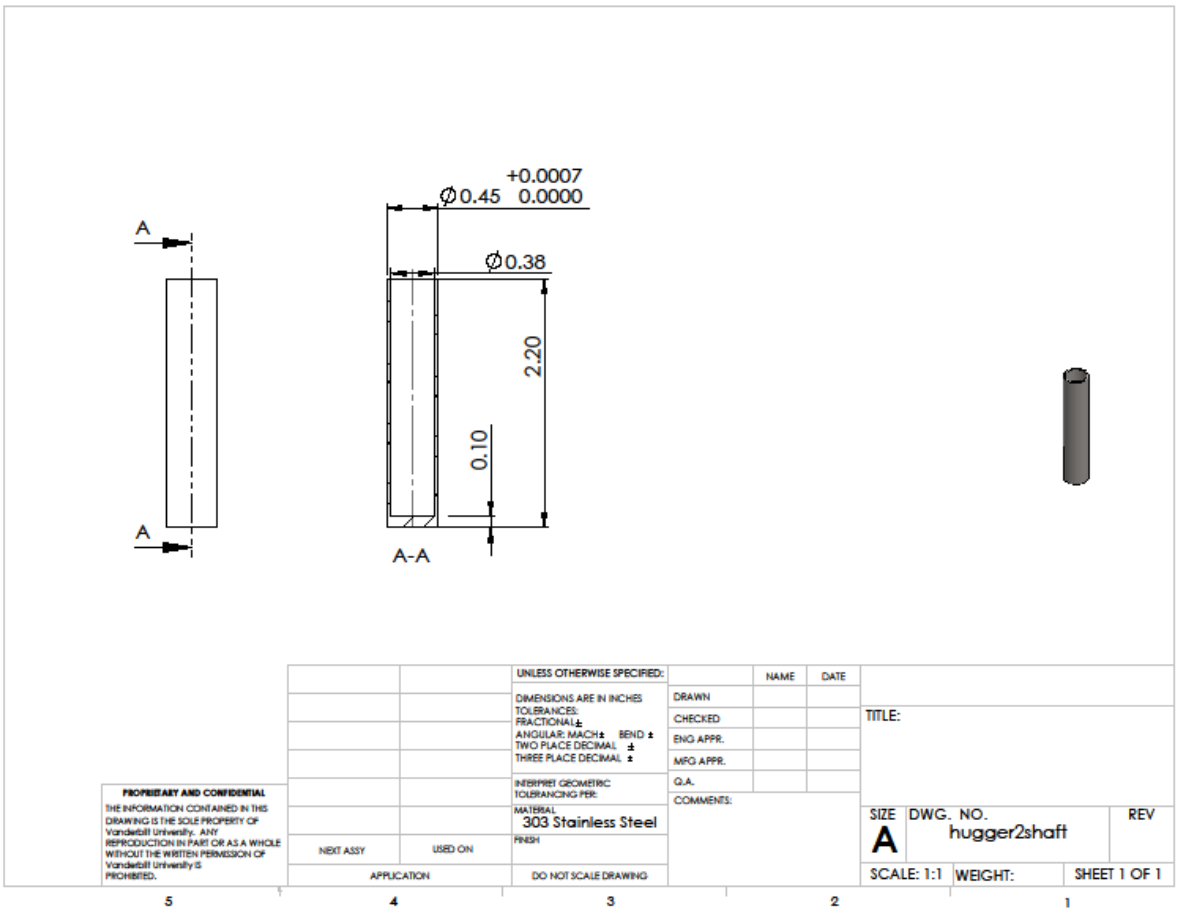

Figure C-12: Shaft part of hugger2

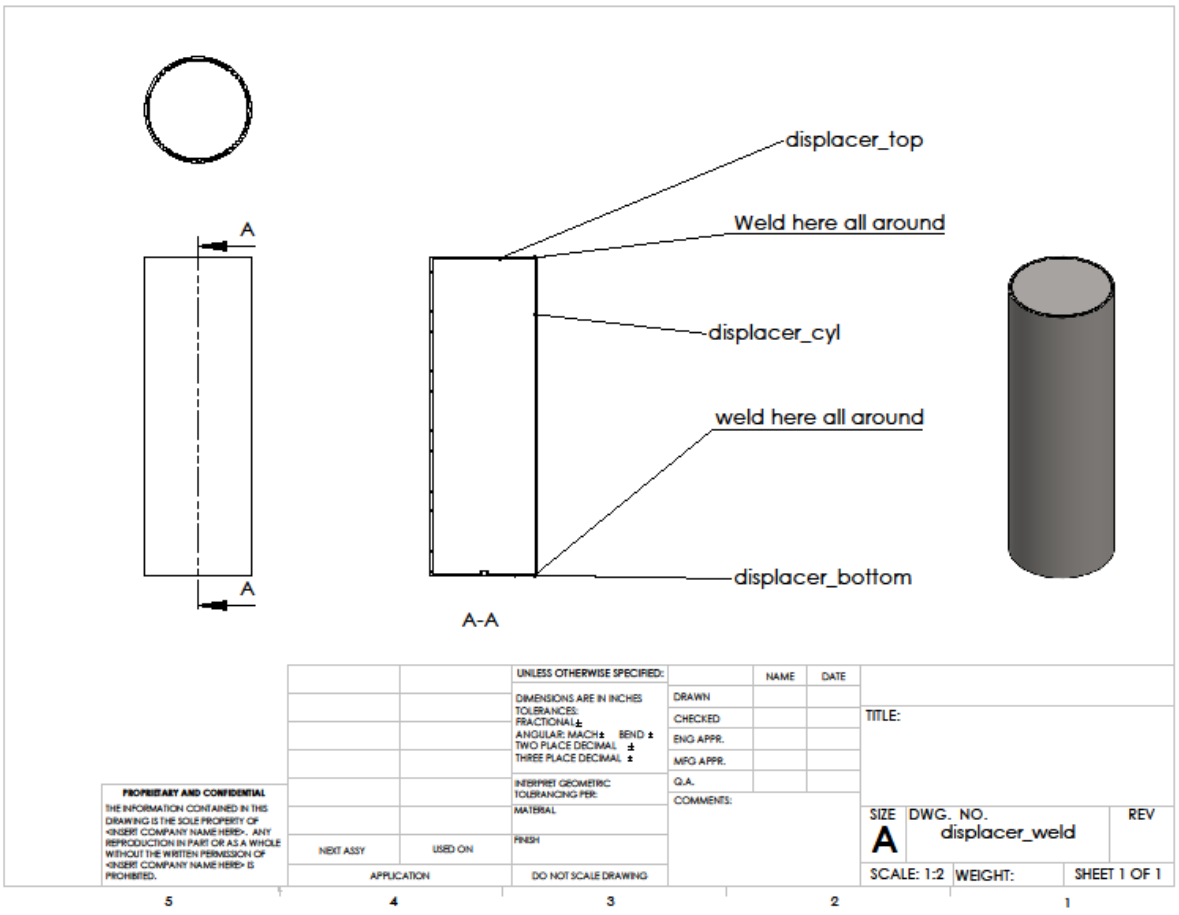

Figure C-13: Displacer weld assembly

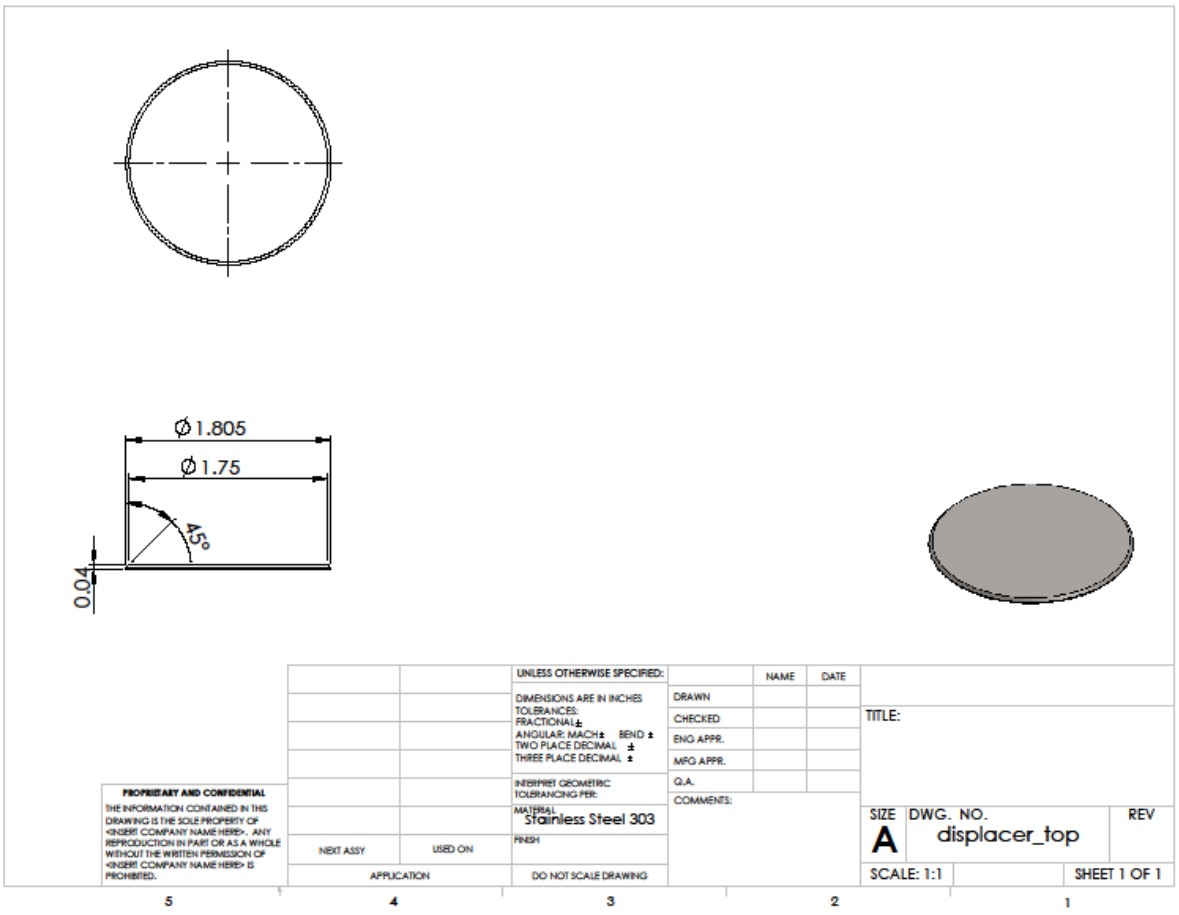

Figure C-14: Top part of displacer piston

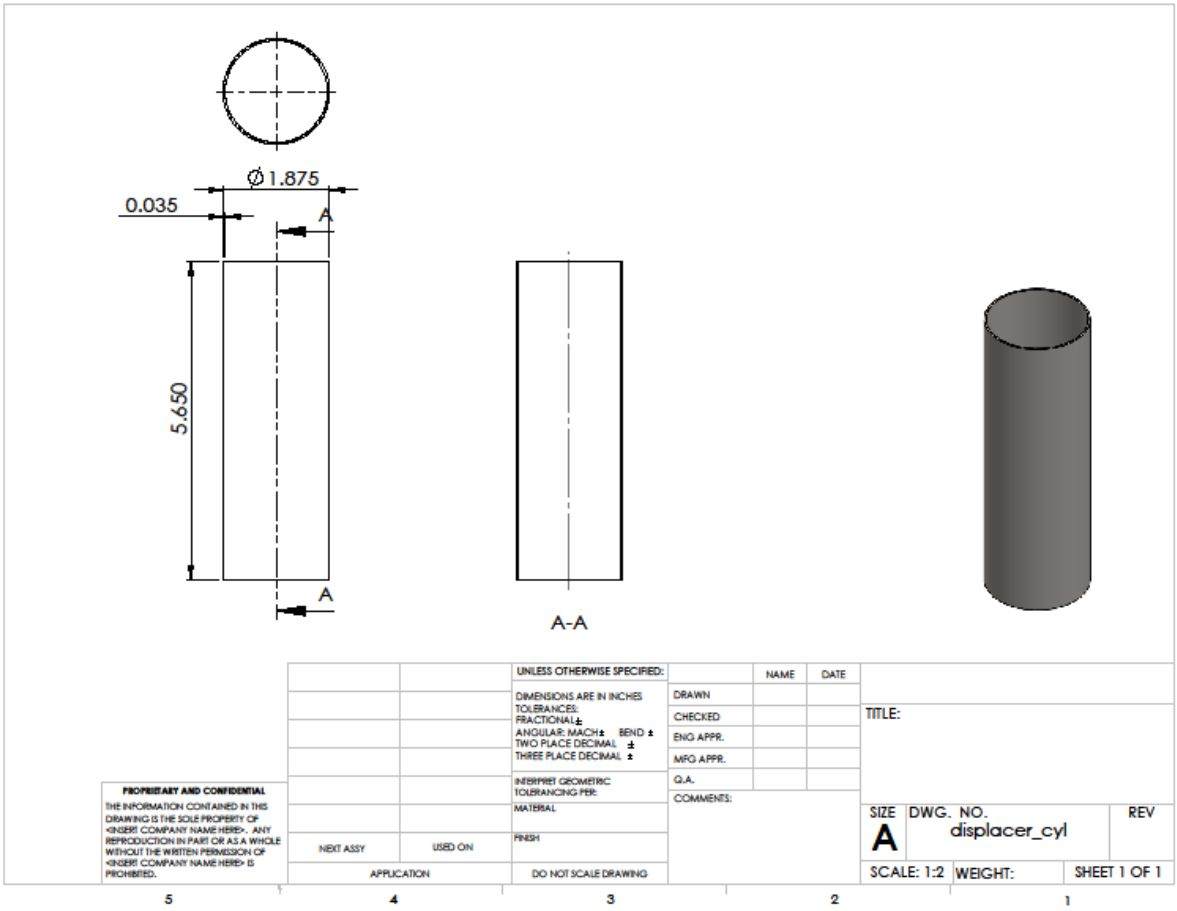

Figure C-15: Displacer cylinder

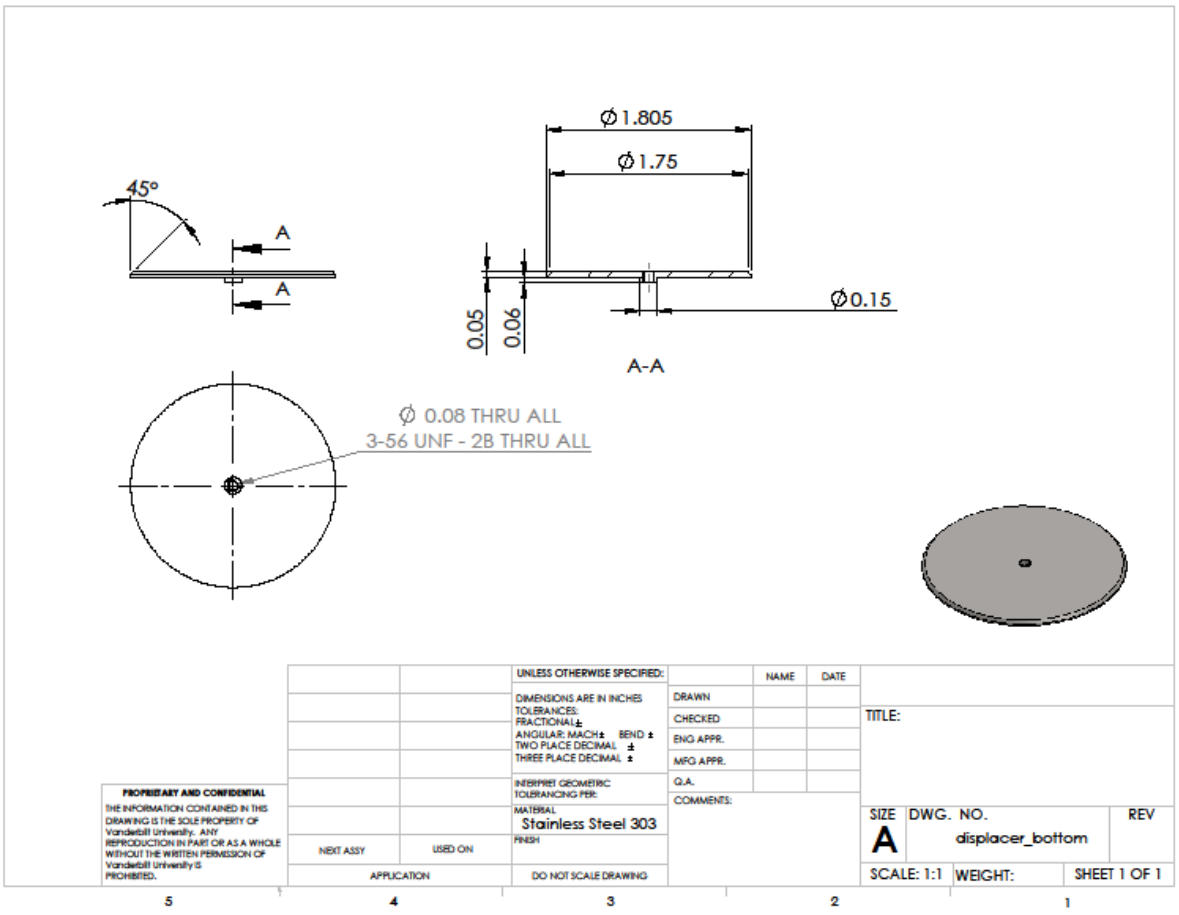

Figure C-16: Bottom of displacer

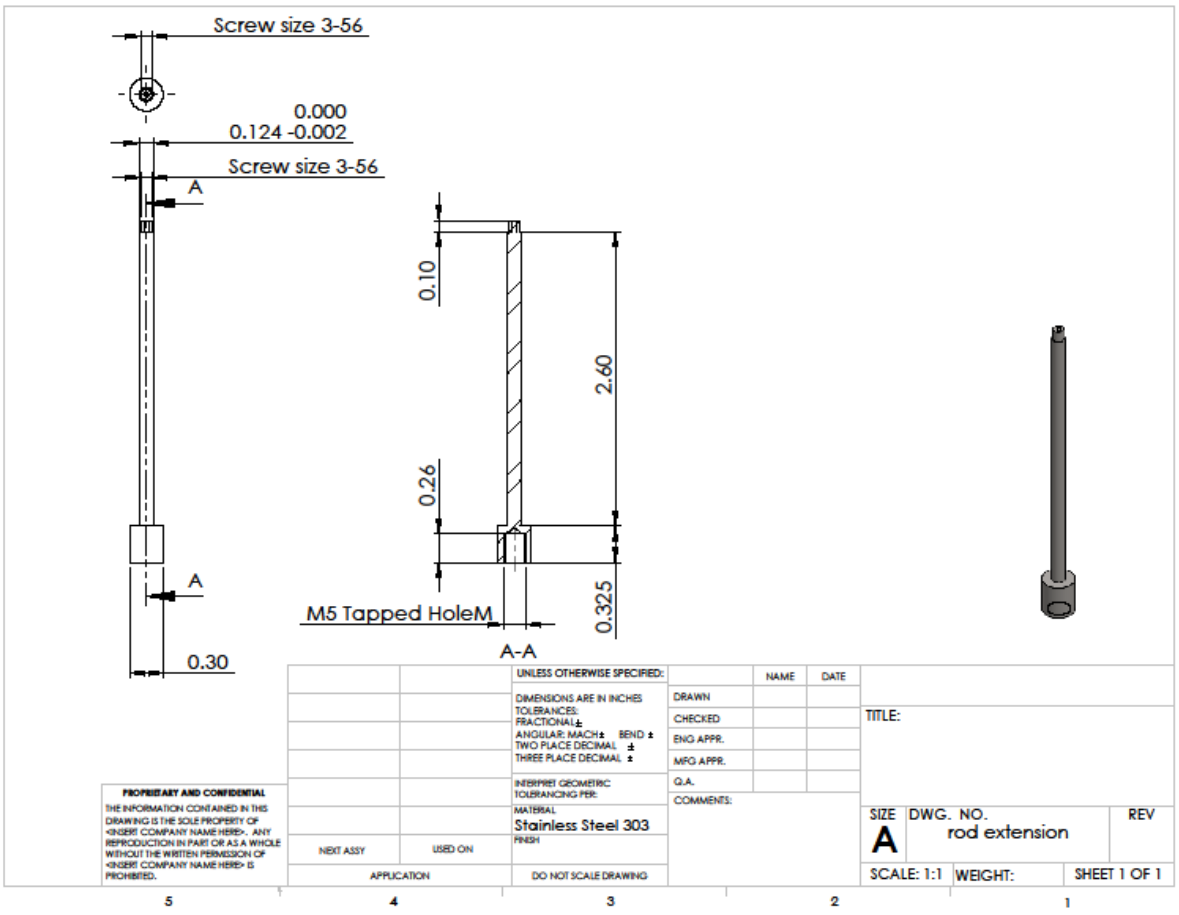

Figure C-17: Extension rod

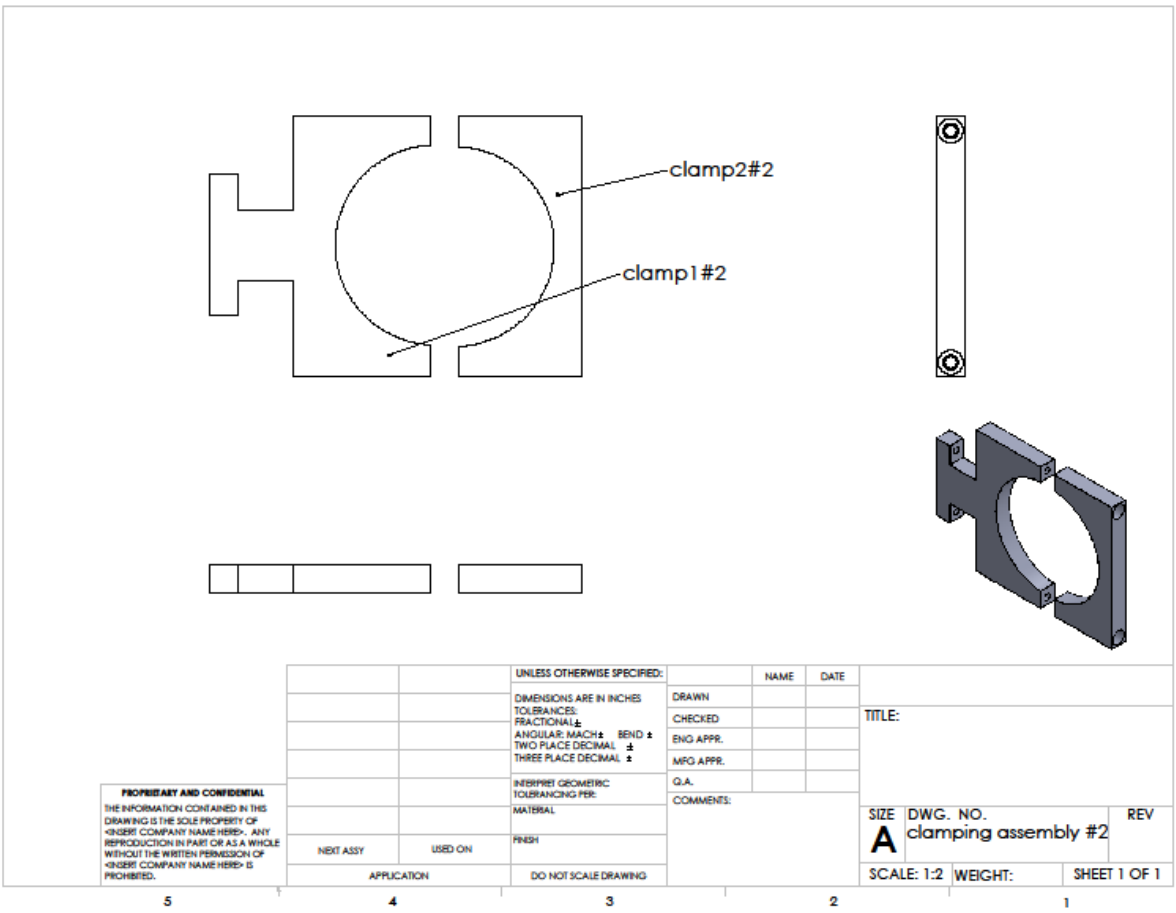

Figure C-18: Clamp assembly

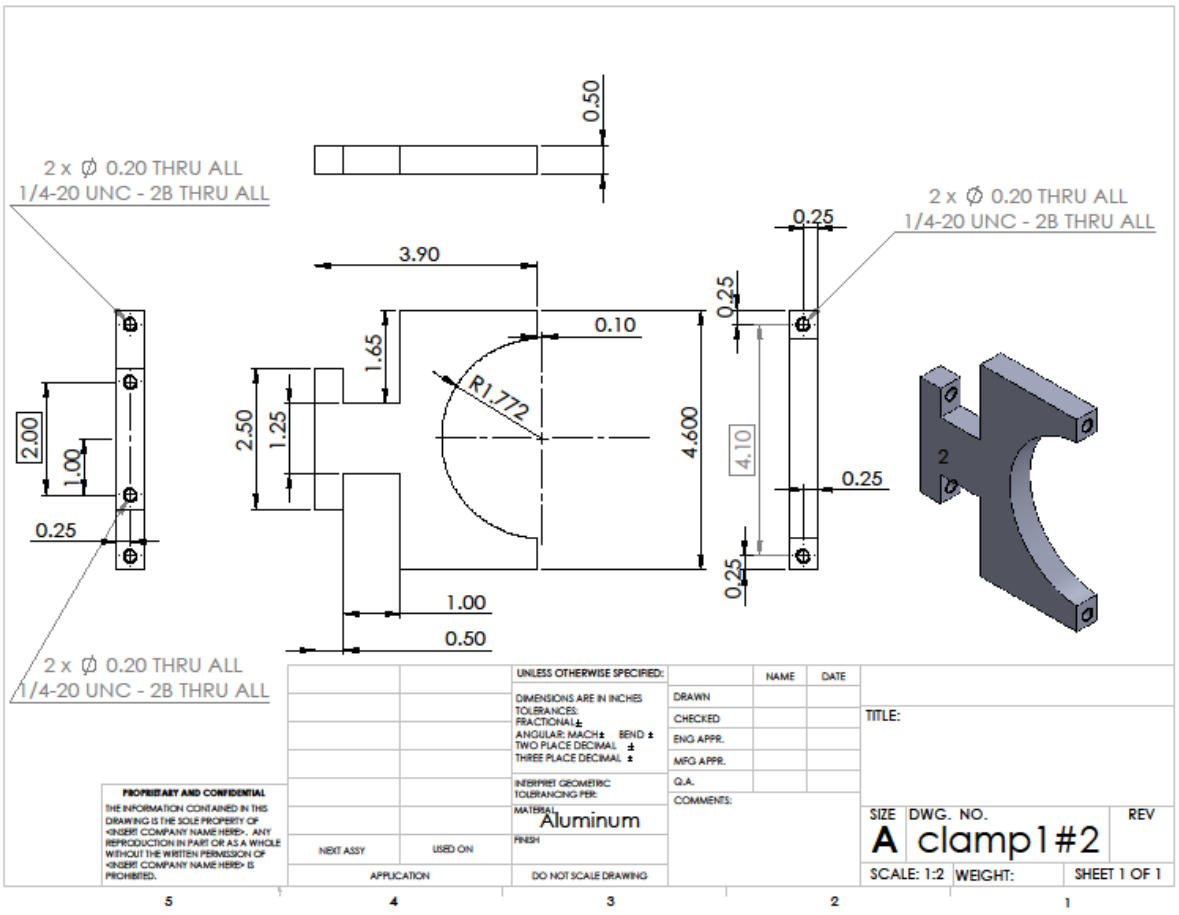

Figure C-19: Part 1 of clamp assembly

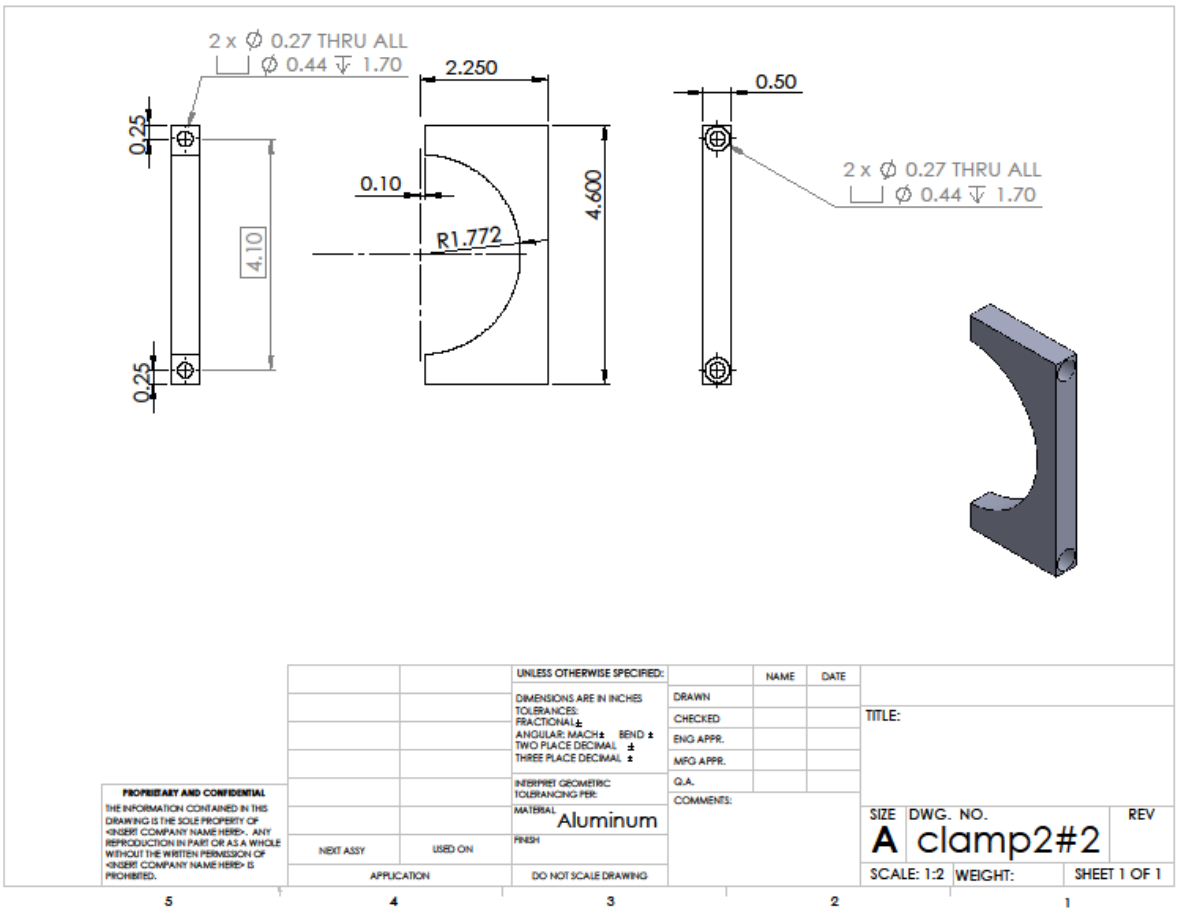

Figure C-20: Part 2 of clamp assembly

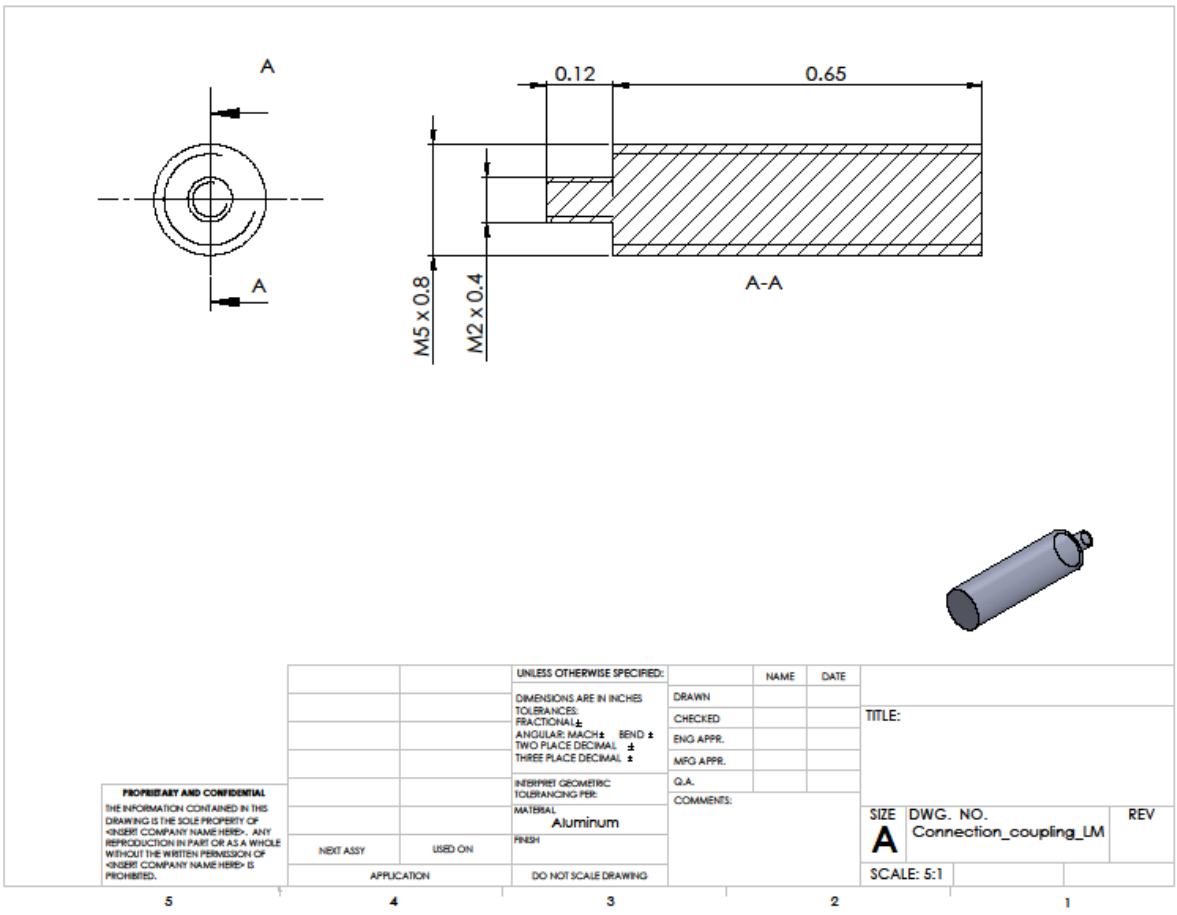

Figure C-21: Connection between coupling and linear motor